NASA Contractor Report 198536

Effects of Shrouded Stator Cavity Flows on Multistage Axial Compressor Aerodynamic Performance

Steven R. Wellborn and Theodore H. Okiishi
Iowa State University
Ames, Iowa

October 1996

Prepared for
Lewis Research Center
Under Grant NAG3–1427

National Aeronautics and
Space Administration

EFFECTS OF SHROUDED STATOR CAVITY FLOWS ON MULTISTAGE AXIAL COMPRESSOR AERODYNAMIC PERFORMANCE

Steven R. Wellborn and Theodore H. Okiishi
Iowa State University
Ames, Iowa 50011

ABSTRACT

Experiments were performed on a low-speed multistage axial-flow compressor to assess the effects of shrouded stator cavity flows on aerodynamic performance. Five configurations, which involved changes in seal-tooth leakage rates and/or elimination of the shrouded stator cavities, were tested. Data collected enabled differences in overall, individual stage and the third stage blade element performance parameters to be compared. The results show conclusively that seal-tooth leakage can have a large impact on compressor aerodynamic performance while the presence of the shrouded stator cavities alone seemed to have little influence. Overall performance data revealed that for every 1% increase in the seal-tooth clearance to blade-height ratio the pressure rise dropped up to 3% while efficiency was reduced by 1 to 1.5 points. These observed efficiency penalty slopes are comparable to those commonly reported for rotor and cantilevered stator tip clearance variations. Therefore, it appears that in order to correctly predict overall performance it is equally important to account for the effects of seal-tooth leakage as it is to include the influence of tip clearance flows. Third stage blade element performance data suggested that the performance degradation observed when leakage was increased was brought about in two distinct ways. First, increasing seal-tooth leakage directly spoiled the near hub performance of the stator row in which leakage occurred. Second, the altered stator exit flow conditions caused by increased leakage impaired the performance of the next downstream stage by decreasing the work input of the downstream rotor and increasing total pressure loss of the downstream stator. These trends caused downstream stages to progressively perform worse.

Other measurements were acquired to determine spatial and temporal flow field variations within the up-and-downstream shrouded stator cavities. Flow within the cavities involved low momentum fluid traveling primarily in the circumferential direction at about 40% of the hub wheel speed. Measurements indicated that the flow within both cavities was much more complex than first envisioned. A vortical flow structure in the meridional plane, similar to a driven cavity, existed within the upstream cavity. Furthermore, other spatial and temporal variations in flow properties existed, the most prominent being caused by the upstream potential influence of the downstream blade.

This influence caused the fluid within cavities near the leading edges of either stator blades in space or rotor blades in time to be driven radially inward relative to fluid near blade mid-pitch. This influence also produced large unsteady velocity fluctuations in the downstream cavity because of the passing of the downstream rotor blade.

TABLE OF CONTENTS

LIST OF FIGURES

LIST OF TABLES

NOMENCLATURE

ENGLISH

a	=	Calibration coefficients
A	=	Annulus cross-sectional area
AR	=	Aspect ratio
b	=	seal-tooth knife thickness
Cd	=	Discharge coefficient
Cp_c	=	Static pressure correction coefficient
Cp_i	=	Probe pressure coefficients
Cp_q	=	Dynamic head pressure coefficient
Cp_s	=	Static pressure coefficient
Cp_t	=	Total pressure coefficient
Cp_α	=	Pitch angle pressure coefficient
Cp_β	=	Yaw angle pressure coefficient
DF	=	Diffusion factor
g_c	=	Standard acceleration of gravity
h	=	Blade span
H^o	=	Total enthalpy
i	=	Incidence angle
$\dot{m}$	=	Primary path massflow
$\dot{m}_l$	=	Leakage path massflow
M	=	Mach number
P	=	Static pressure
P_i	=	Probe pressures
P^o	=	Total pressure
r	=	Radius

Re = Reynolds number

T_{dp} = Dew point temperature

T^o = Total temperature

Tq = Measured torque

Tq_{tare} = Tare torque

U = Blade speed

Un = Unsteadiness intensity correlated with rotor passing frequency

V = Absolute velocity magnitude

V_r = Absolute velocity in the radial direction

V_θ = Absolute velocity in the tangential direction

V_z = Absolute velocity in the axial direction

W_θ = Relative velocity in the tangential direction

GREEK

α = Pitch angle

β = Yaw angle

β^* = Blade angles

δ = Deviation angle

δ^* = Displacement thickness

δf = *N*th-Order uncertainty variable

δf_b = Bias uncertainty variable

δf_p = Precision uncertainty variable

δx = Independent uncertainty variable

γ = Blade setting angle

γ = Specific heat ratio

ϵ = Seal-tooth clearance

η = Efficiency

ρ	=	Density
σ	=	Solidity
ϕ	=	Flow coefficient
ψ	=	Work coefficient
$\psi/$	=	Pressure rise coefficient
ω	=	Shaft rotational speed
ω	=	Total pressure loss coefficient
ω_p	=	Loss parameter

SUBSCRIPTS

b	=	Best configuration
c	=	Known calibration angles
cl	=	Centerline condition
in	=	Inlet station
$isen$	=	Isentropic condition
max	=	Maximum
out	=	Outlet station
ref	=	Reference condition
tip	=	Blade tip
w	=	Worst configuration
$1, 2, 3, 4$	=	Stage number
$1d$	=	One-dimensional
0.1	=	Station 0.1
1.0	=	Station 1.0
5.0	=	Station 5.0

SUPERSCRIPTS

$\overline{f}$	=	Area averaged quantity
$\overline{f}^m$	=	Mass averaged quantity
$\widetilde{f}$	=	Time averaged quantity over one rotor pitch
f'	=	Unsteady perturbation quantity $(f(t) - \widetilde{f})$

ACKNOWLEDGMENTS

The research reported in this dissertation owes its existence to the efforts of many. We express my appreciation to the NASA Lewis Research Center, Cleveland, Ohio, sponsor of this work under Grant No. NAG 3–1427. In addition, we acknowledge the test cell personnel without whose support this research endeavor would not have been possible. In particular I would like to thank Bill Darby, Don Costello, Bob Ehrbar, Tom Jet, Mary Ann Lupica, Rick Senyitko, Charles Wasserbauer and Hal Weaver for their advice, support, assistance and skilled workmanship. Many long hours were logged by these personnel preparing the rig for a run day or operating the facility. Their hard work, in the end, produced high quality data for a meaningful study.

CHAPTER I

INTRODUCTION AND LITERATURE REVIEW

Leakage flows exist in turbomachines. They are normally created by pressure differences across open clearances or channels in which fluid is driven from high to low pressure regions. Leakage flows may be extracted from or injected into the power stream from secondary flow paths. They also arise at the interface of rotating and stationary members within or near individual blade rows. In general, when not accounted for in the design process, leakage flows alter the blockage and loss distributions in the primary flow path which in turn may lower the effectiveness and efficiency of a turbomachine.

Axial-flow compressors have leakage in a number of places. Figure I.1 shows a few of these locations within a modern high pressure core compressor. In the past, rotor blade tip clearance leakage has been most commonly studied and the large number of recent reports on this topic indicate the subject is still important. Studies which detail the impact of other kinds of leakage flows on compressor performance have been reported to a much lesser extent. These flows include shrouded blade seal-tooth leakage, rotor dovetail leakage, variable stator pivot / clearance leakage and customer bleed. All of these and other types of leakages which are present in gas turbine engines have been thoroughly documented by Ludwig [1] and Wisler [2].

The negative impacts of some of the above mentioned leakage flows on compressor performance have been well documented over the years. For example, the increase of rotor tip clearance leakage leads to a reduction in stage pressure rise, efficiency and flow range. For rotor blades with normal operating clearances a general rule is to expect a 1.5 point reduction in efficiency for every 1% increase in the clearance to blade-height ratio [1,3]. The reduction in stall margin can be as great as 6% for every 1% increase in clearance to chord ratio [2]. These are substantial penalties for engine manufacturers and users to endure. For multistage compressors, the cumulative impact of leakage on performance can be even more significant, since not only is performance degraded, but stage matching becomes altered from the design intent.

Problems associated with leakage flows become even more critical for at least two reasons. First, clearances increase because of wear. Airline reports indicate that engine specific fuel consumption increases over time. Periodic overhauls of these engines do not fully recover the reduction in performance. This deterioration has been blamed on wear of blades and seals which open clearances and in turn allow more leakage. Second, trends in aircraft engines toward highly loaded stages [4] and low aspect ratio blading [5] result in leakage flows becoming increasingly influential on compressor performance. Highly loaded stages imply more leakage for the same geometric clearances and lower aspect

ratio blades can create stronger secondary flows which in turn force a larger percentage of the blade to be affected by leakage. Furthermore, higher pressure differences promote faster erosion of the blades and seals.

In axial-flow compressors, designers commonly consider two options for the construction of stator blades: cantilevered airfoils or hub shrouded airfoils. Illustrations of each of these configurations are shown in Figure I.2. Both options produce leakage flows; however, the types of leakage generated are different in nature.

Cantilevered airfoils (Figure I.2a) are connected at the case while at the hub they remain free. Since stators are stationary and the hub endwall rotates, a running clearance is present at the hub interface. This clearance allows flow leakage across the end of the

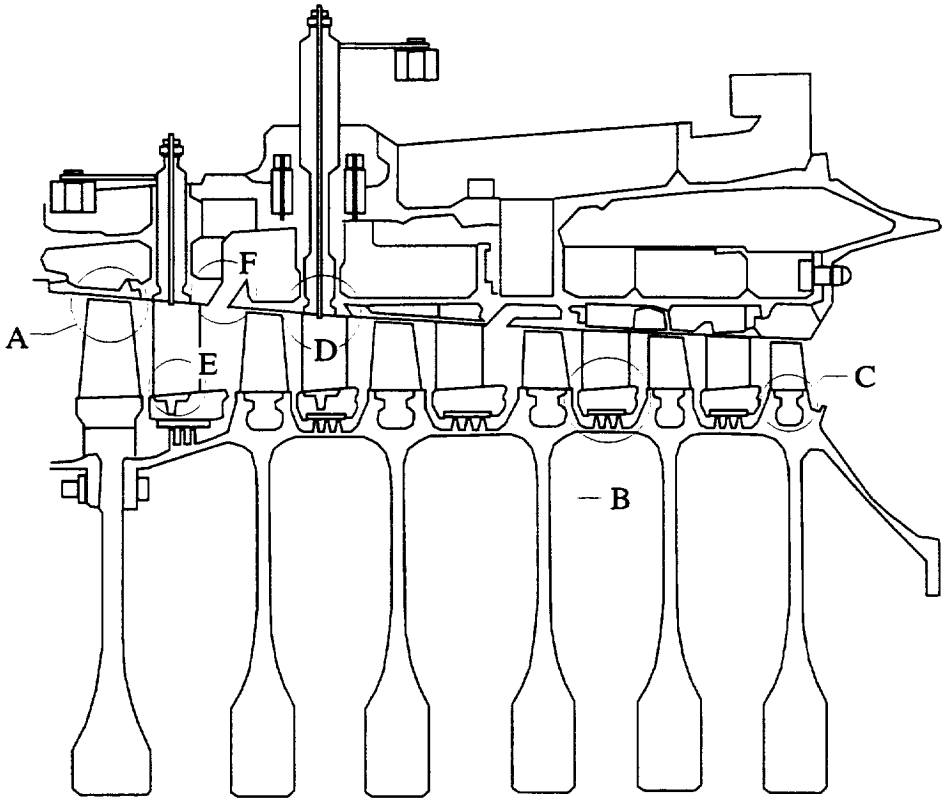

A. Rotor tip clearance leakage

B. Shrouded stator leakage

C. Dovetail leakage

D. Variable stator pivot leakage

E. Variable stator clearance leakage

F. Customer bleed

Figure I.1 Leakage paths within an axial-flow core compressor.

airfoil. The leakage is driven by the pressure differential across the blade. Unfortunately, cantilevered blades require relatively large hub-to-endwall clearances in order to avoid rubs and possible catastrophic damage. Large clearances can cause large amounts of leakage. Furthermore, since the stator hub end is free, cantilevered blades may be susceptible to vibration problems.

Shrouded stators (Figure I.2b) are connected at both the case and hub. To fix the hub end, the blades are normally pinned to an annular foot-ring which is concentric to the rotor. The pinned hub reduces the risk of vibrations which thereby also allows the airfoils to be thinner than their cantilevered counterparts, both considered as attributes to designers. To accommodate the foot-ring, a cavity exists in the rotor drum. The foot-ring is immersed in the cavity and therefore transparent to the primary flow path. Since the stator row produces a static pressure rise and the cavity allows a leakage path, fluid is

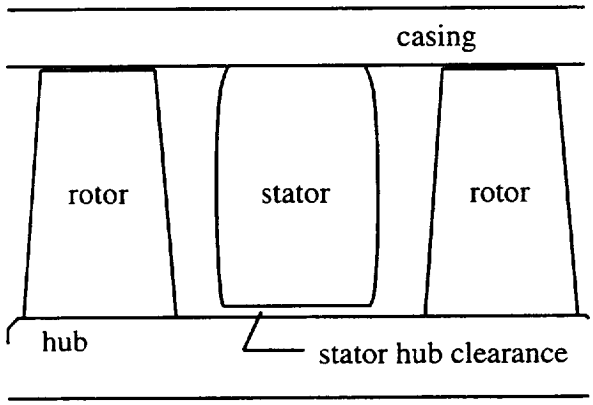

a) cantilevered stator blades

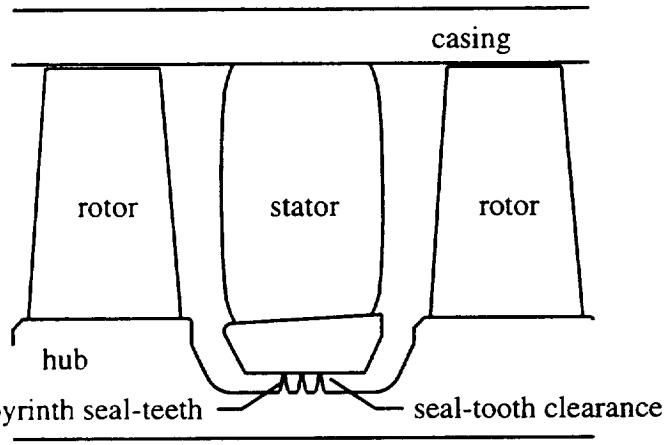

b) hub shrouded stator blades

Figure I.2 Options for the construction of stator blades.

normally driven through the foot-ring cavity from the trailing edge opening to the leading edge opening. This is in the reverse direction of the primary flow. Multiple labyrinth seal-teeth and special design of the cavities are required to minimize gas recirculation through the cavity.

The decision to cantilever or shroud stators is generally a mechanical choice. Structural integrity objectives such as keeping the first flex, first torsion and two-strip frequencies out of the operating range [2] usually outweigh any aerodynamic considerations. Shrouding usually provides the mechanical stability desired and therefore modern gas turbine engines typically employ shrouded stator blades. The choice to shroud of course eliminates the troubles associated with hub clearance leakage flows found with cantilevered stator blades, but replaces them with the difficulties of shrouded stator leakage flows.

Researchers have briefly commented on the influence of shrouded stator seal tooth leakage on compressor performance. Some published examples are given by Jefferson and Turner [6], Mahler [7], Freeman [3] and Wisler [2]. Jefferson and Turner provided an excellent review which detailed the effects of shrouding stator blades, which were originally cantilevered, on the performance of an industrial multistage compressor. Unfortunately, the blading and type of shroud used in their study were not typical of what is currently used in engines today. Mahler reviewed tests conducted on a multistage research compressor with two-lipped interstage labyrinth seals in which the seal clearance was varied. A relation was developed from the measured data which correlated efficiency to the seal-tooth clearance. Estimates of this correlation for current fighter and transport engines were also provided. All data showed a reduction in efficiency as seal-tooth clearance was increased. These trends are reproduced in Figure I.3. Note that the correlations are all dissimilar because of the different leakage characteristics of the seals employed for each implementation. Freeman presented data taken from a two-stage low reaction compressor in which clearance amounts were changed for shrouded blades having either deep or shallow cavities. Those measurements also suggested a loss in efficiency, shown in Figure I.4, with an increase in seal-tooth clearance. The depth of the cavity did not greatly impact the results. Wisler also hinted at the importance of seal-leakage flows when he reported a 2.3 point reduction in efficiency and a 10.3% decrease in the average pressure rise of a four-stage multistage compressor when both rotor tip and labyrinth seal-tooth clearances were increased. Although both of these clearances usually deteriorate together in an engine (as noted by Wisler), by changing both clearances simultaneously it is difficult to determine the influence of seal-tooth leakage alone on overall performance. Finally, no known literature addresses how the presence of the up-and-downstream shrouded stator cavities alone impact multistage compressor performance.

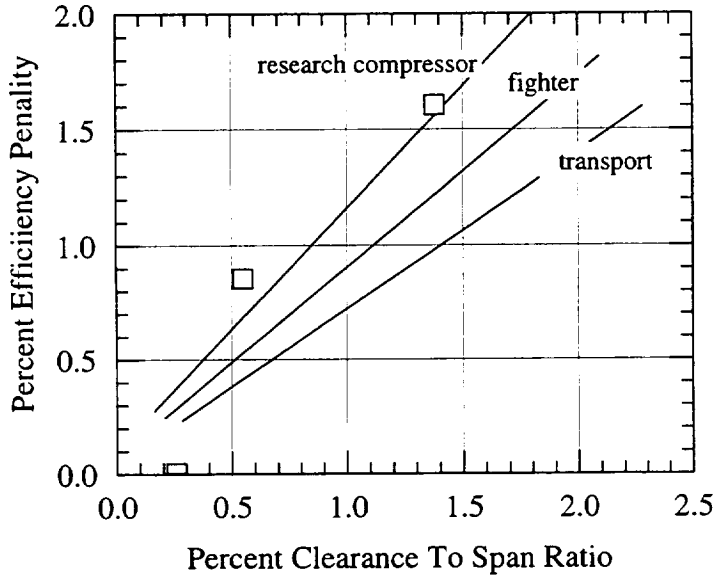

Figure I.3 Penalty in efficiency with increased seal-tooth clearance (from Mahler [7]).

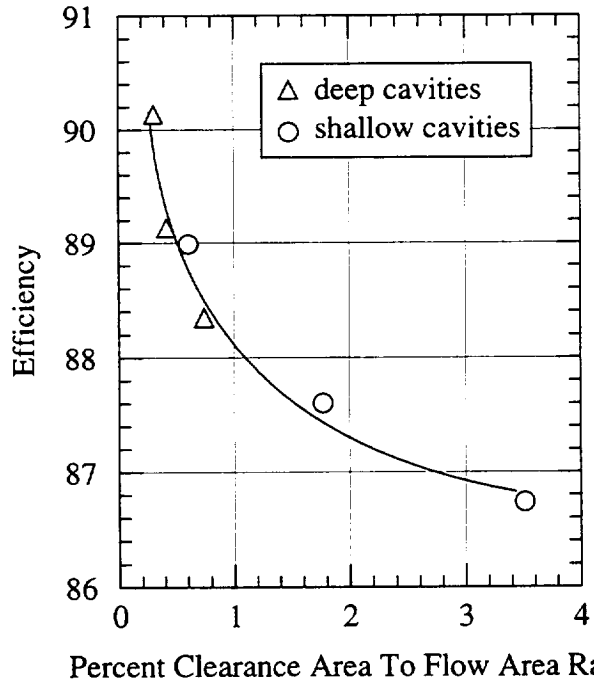

Figure I.4 Reduction in efficiency with increased seal-tooth clearance area (from Freeman [3]).

Although past experience has revealed that seal-tooth leakage affects the efficiency of a compressor, few details have been published regarding the changes in the power stream flow field which occur when seal-tooth leakage is present. Furthermore, even fewer details are given about the character of the flow within shrouded stator cavities. Adkins and Smith [8] suggested that shrouded blade endwall leakage enters the power stream with little meridional velocity and becomes entrained by the main flow. Limited data presented in the same article indicated that leakage caused a reduction in the circumferentially averaged stator turning of the flow. It was postulated that this was due to a weakened suction surface boundary layer, possibly caused by the leakage flow. In a separate article concerned with secondary flows in turbomachinery, Wisler *et al.* [9] demonstrated that increasing seal-tooth leakage enhanced flow overturning very near the hub. They also hinted that at high loading levels, increasing leakage relieved the suction side vane boundary layer. This appears to be contrary to the hypotheses advanced by Adkins and Smith. More recently, LeJambre *et al.* [10] have shown in a multistage compressor calculation that extra hub blockage develops in the power stream because of the entrained leakage flow. Even with these examples, it remains unclear how the presence of shrouded stator flows influence the power stream flow property distributions. This lack of understanding is obviously a barrier for compressor designers.

It is not surprising to find that a review of open literature suggests designers may not always model shrouded stator flows or specifically account for the effects of these flows in design throughflow calculations. Adkins and Smith [8] have discussed the possibility of modeling the entrained leakage flow as an upstream vorticity source entering the stator blade row and therefore subject to the development of secondary flow which augments the spanwise and pitchwise movement and mixing of fluid particles. Assuming the shrouded stator leakage flow enters the primary flow as a boundary layer collateral to the freestream flow, secondary flow velocities are calculated from the secondary vorticity in a fashion similar to those for typical endwall boundary layer flows (details can be found in [8] and [11]). To include the result of reduction in flow turning with increased seal-tooth leakage, a relation is used which correlates the change in stator turning to the change in circulation. Circulation is in turn empirically correlated to the amount of known leakage flow through the seal-tooth. The implementation of this model into a design calculation showed fair agreement between predicted and test data. The trend of increased flow deviation with increased leakage was established and in general the departure of the measured flow angles from the calculated flow angles showed the model worked reasonably well; however, the calculated stator total pressure loss near the hub was not in good agreement with test data. The model employed considerably overestimated the magnitude of total pressure loss from 5–20% stator span and underestimated it from 0–5% span. In a separate study, Denton [12] also concluded that a lack of experimental data has hindered the modeling of loss mechanisms associated with seal-tooth leakage.

The only fair agreement between the Adkins-Smith model and measured data combined with the lack of any other published data indicate that a systematic study detailing the influence of shrouded flows could be beneficial to engineers who want to better account for these flows in the compressor throughflow design process.

Computational fluid dynamics is being increasingly used for turbomachinery design. Advancements in computer speeds, storage capacities and computational methods have allowed engineers to move away from simple single blade row calculations to include the effects of multiple stages, three dimensional blade geometries, off-design operation and various leakage flows. The importance of including the effects of shrouded stator leakage flows in the design of a multistage compressor was given by LeJambre *et al.* [10] For these calculations the cavity flow was modeled as a simple flow extraction at the stator trailing edge and injection at the leading edge (few details of the simple model were given). Changes to the original axisymmetric axial velocity distribution occurred when the cavity model was employed. Furthermore, the work input of the downstream rotor better matched experimental data when the cavity model was applied. A separate computational effort performed concurrently with this investigation (Heidegger *et al.* [13]) has started to systematically investigate the influence of a variety of shrouded stator geometric parameters on stator blade performance. This parametric study has been beneficial to the work reported herein and upon completion may prove to be valuable for designers. Unfortunately, as with all new design tools, the accuracy of the computed results remain in question until thoroughly validated. A consistent set of experimental data detailing the effect of shrouded stator flows on multistage compressor flow fields would therefore be beneficial to designers in order to assess the accuracy of computational fluid dynamic results.

In summary, the mechanical based decision to shroud stator blades in axial-flow compressors produces shrouded stator cavity flows. A primary component of these cavity flows results from leakage through labyrinth seal-teeth. Although seal-tooth leakage has been shown to reduce compressor efficiency, only limited data are available which detail changes in the primary flow field when this leakage is present. Furthermore, no known study addresses how or if the shrouded stator cavities alone impact compressor performance. This general lack of knowledge concerning shrouded stator cavity flows can severely limit engineers who use throughflow or computational fluid dynamics methods in their design of axial-flow compressors.

CHAPTER II

OBJECTIVES AND APPROACH

The objectives of this study stemmed from the general lack of present knowledge concerning the effects of shrouded stator cavity flows on multistage axial-flow compressor aerodynamics as reviewed in Chapter I. The overall objectives of this study are 1) to quantify the importance of shrouded stator cavity flows on the performance of a multistage compressor, 2) to specifically describe how shrouded stator cavity flows effect the performance of an embedded stage and 3) to provide information about the flow field within shrouded stator cavities.

The intent of the objectives is to answer a broad range of questions concerning how compressor performance values are altered when either shrouded stator cavities or seal-tooth leakage rates are modified in the stages of a multistage compressor. The first objective was set to demonstrate that shrouded stator flows really do affect compressor aerodynamic performance. Completion of this objective gave a reasonable guess at the performance penalties which could be expected in a core compressor when shrouded stator flows change. The second objective was established to better understand what influence shrouded stator flows have on the power stream flow. Completion of this objective helped to explain how the observed changes in overall performance value occurred, provided detailed information on important changes in the power stream flow field and also gave insight into how shrouded stator cavity flows may effect stage matching. The third objective was chosen since little is known about the details of shrouded stator cavity flow fields. Completion of the third objective could help engineers better model shrouded stator cavity flows in designing of axial-flow compressors.

Achievement of the objectives was completed by performing tests on a four-stage low-speed axial-flow compressor. For the first two objectives, two separate experiments were completed. In the first one, labeled Part 1, modifications to the shrouded stator cavity flows were incorporated on all four stages of the compressor. In the second, Part 2, alterations were made only to the third stage cavity flows while the other stages were kept at the baseline condition. In both experiments, measurements were taken which allowed overall, individual stage and blade element performance parameters to be calculated. Comparison of these data answered questions relating to the first two objectives. To achieve the third objective, detailed pressure and velocity distributions within the shrouded stator cavities were acquired with pneumatic and hotfilm probes.

CHAPTER III

EXPERIMENTAL FACILITY

The NASA Lewis Research Center Low-Speed Axial Compressor (LSAC) facilitY is described in this chapter. Stage blade geometry parameters are also specified. Further details of the LSAC facility may be found in Wasserbauer *et al.* [14] Information concerning the probe calibration facility maybe found in Appendix B.

Large Low-Speed Axial-Flow Compressor Test Facility

An illustration of the NASA Lewis Research Center Large Low-Speed Axial-Flow Compressor (LSAC) is shown in Figure III.2. A detailed meridional view of the third stage is shown in Figure III.1. Relevant design parameters are listed in Table III.1. The LSAC was modeled after the GE Low-Speed Research Compressor, which has been used for improving multistage compressor design and technology for the past forty years. The blading, presented in the next section, was modeled after a design used to develop the Energy Efficient Engine. Some important blading parameters are also given in Table III.1.

In line with GE's philosophy, the LSAC incorporated many common features in an attempt to achieve an accurate low-speed simulation of a high speed multistage compressor. A long entrance length was used to develop thick endwall boundary layers typical of an embedded stage. An inlet-guide vane row was used to generate exit flow angles similar to what the embedded stators would produce. Four repeating stages (stages with identical blade geometry) were used. The first two stages were assumed to set up a repeating stage environment. The third stage was considered the test stage. The fourth stage continued the repeating stage environment and buffered the third stage from the compressor exit conditions. For each of the stages, the stators were shrouded with one labyrinth seal-tooth in the shrouded stator cavity and were sealed at both the hub and case blade tip interfaces.

Stage Blade Geometry

The blading used for all tests were based on the Rotor B / Stator B geometry designed by General Electric, under Contract NAS3–20070, and tested in their Low-Speed Research Compressor. The GE blades were designed to reduce loss in the endwalls of a representative core compressor. Complete details of the original designs were given by Wisler [15]. Some simple modifications to original geometry were incorporated into the NASA blades because of the differences in the hub-to-tip ratios of the two facilities. A description of the blades, the changes that were made to the original GE geometry

and the spanwise variations, presented as percent span from the hub, of both NASA's and GE's blading parameters are presented.

Rotor Blades

A photograph of the rotor blade is given in Figure III.3. Blade profiles at 10, 50 and 90% span are shown in Figure III.4. The rotor consisted of airfoil sections having modified circular-arc meanlines with 2° and 6° overcambering at the leading and trailing edges. The stacking axis was at 50% chord. Modified circular-arc thickness distributions were used. At the tip maximum thickness was at 60% chord. This blended to 50% chord at the pitchline. These deviations from standard circular arc distributions helped to increase the loading level at the tip and trailing edge of the rotor blade.

Radial distributions of rotor solidity and aspect ratio are illustrated in Figure III.5. The aspect ratios for each blade were kept constant along the span ($AR \approx 1.2$). However, since the hub-to-tip ratios of the two facilities were different, radial distributions of solidity could not be identically matched. No modifications were incorporated into NASA's geometry to account for differences in deviation and/or secondary flow which could arise due to the differences in solidity. The radial distributions of rotor leading edge, trailing edge and setting angles are depicted in Figure III.6. NASA's angles match

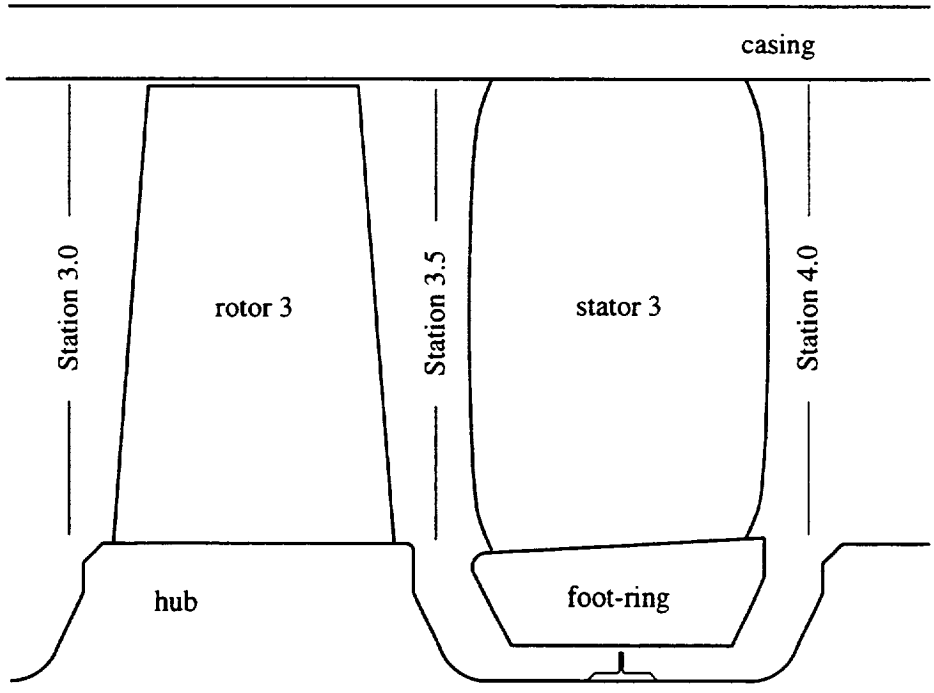

Figure III.1 Meridional view of the third stage of the LSAC.

Table III.1 Baseline parameters for the Low-Speed Axial-Flow Compressor.

Casing radius	60.96 cm
Hub radius	48.8 cm
Hub-to-tip ratio	0.80
Blade span	12.19 cm
Rotational speed	958 rpm
Rotor tip speed (based on casing radius)	61.15 m / s
Mass flow	12.3 kg / s
Axial velocity	24.4 m /s
Pressure ratio	1.042
Temperature ratio	1.013
Flow coefficient, ϕ	0.400
Average pressure rise coefficient, $\psi'/4$	0.500
Average work coefficient, $\psi/4$	0.550
Nominal axial gap	2.54 cm
Number of blades	
Rotor	39
Stator and IGV	52
Midspan aerodynamic chord	
Rotor	10.2 cm
Stator	9.4 cm
Midspan blade setting angle	
Rotor	43°
Stator	42°
Clearances	
Rotor tip	1.7 mm (1.4% span)
Stator shroud labyrinth seal	0.85 mm (0.70% span)

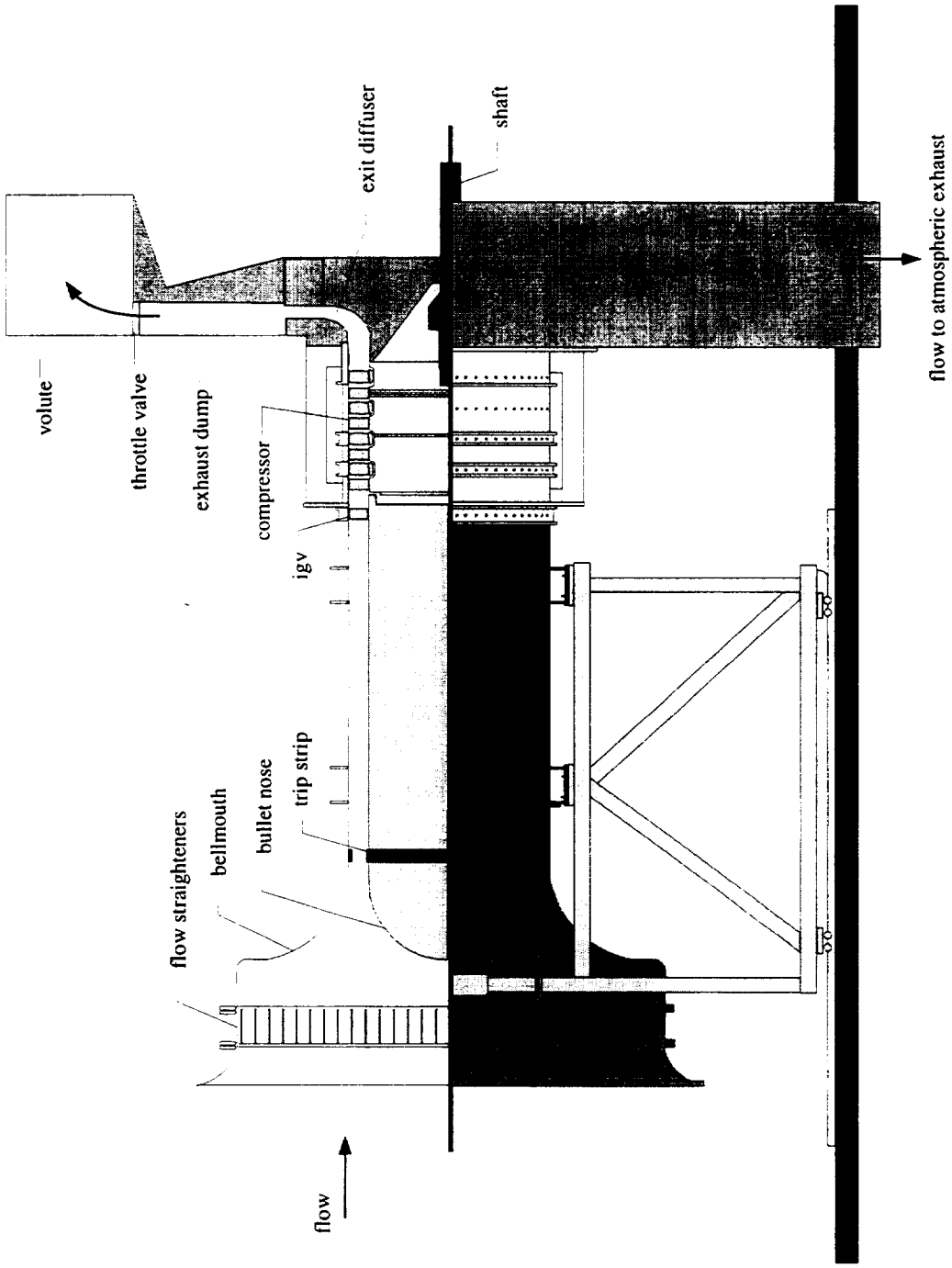

Figure III.2 NASA Lewis Low-Speed Axial-Flow Compressor.

GE's angles at the hub, but not at the tip. This departure from the original design was incorporated in order to account for the different hub-to-tip ratios and attempted to keep velocity triangles the same across the span between the two geometries.

Stator Blades

A stator blade is shown in Figure III.7. As seen, the stators employ end-bends at both the hub and case. Blade profiles for 10, 50 and 90 % span are illustrated in Figure III.8. The stator consisted of airfoil sections having 65–series thickness distributions on a modified circular-arc meanline. Leading edge overcambering (3.5°) was needed in order to achieve representative suction surface velocity distributions. No trailing edge overcambering was incorporated. As explained by Wisler [15], the type of twist used in the stator could lead to large acute angles at the leading edge where the suction surface meets the endwalls. Conversely, large obtuse angles could occur near the trailing edge. In order to prevent this, the airfoil sections were stacked at the 30% chord location, instead of the usual 50%.

Radial distributions of stator solidity and aspect ratio are illustrated in Figure III.9. Aspect ratio distributions were matched while solidity distributions were allowed to vary. Again, no modifications were incorporated to NASA's stator geometry for differences in deviation and/or secondary flow which could arise because of the differences in solidity. The radial distributions of stator leading edge, trailing edge and setting angles are depicted in Figure III.10. As with the rotor, to keep the velocity triangle distributions the same across the span, NASA's geometry employed a linear twist from hub to tip which increased the tip angles by about 1.2°.

Figure III.3 Low-speed axial-flow compressor rotor.

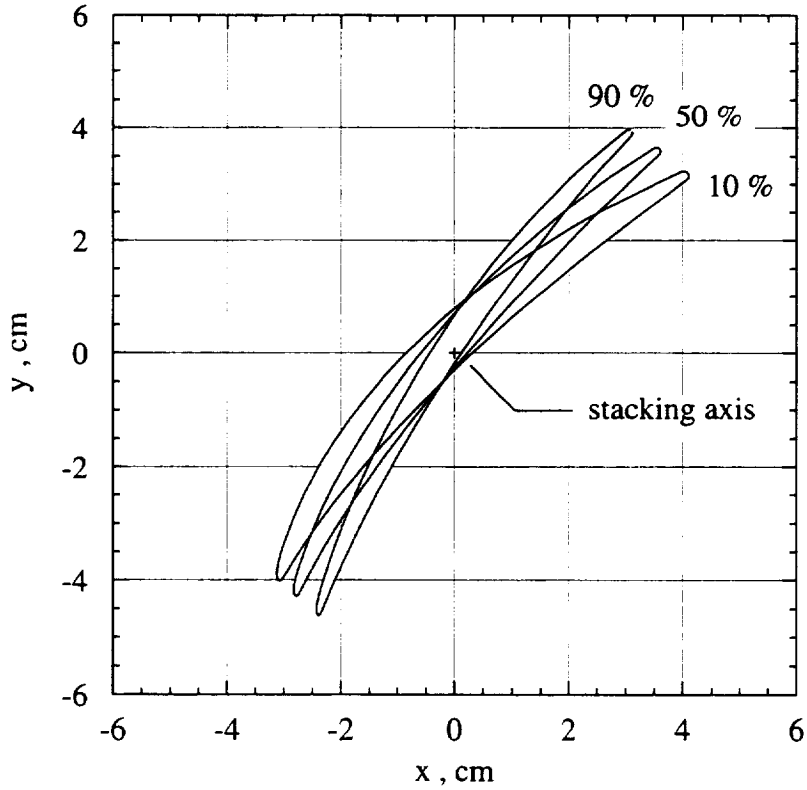

Figure III.4 Rotor airfoil sections at 10, 50 and 90% span.

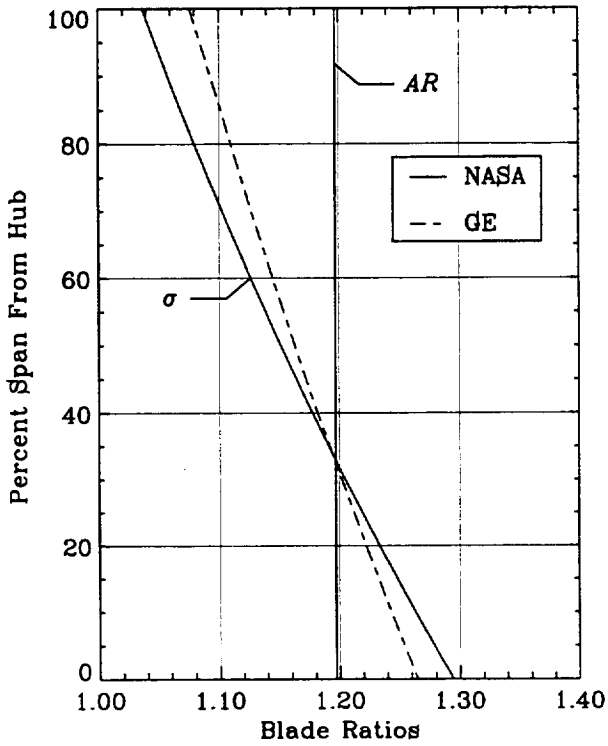

Figure III.5 Radial distributions of rotor solidity and aspect ratio.

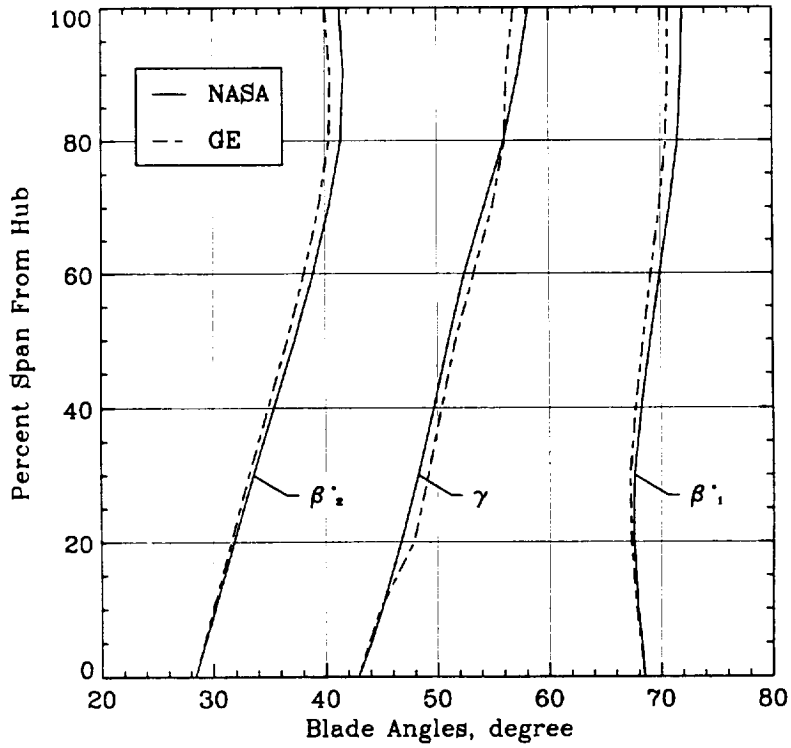

Figure III.6 Radial distributions of rotor leading edge, trailing edge and setting angles.

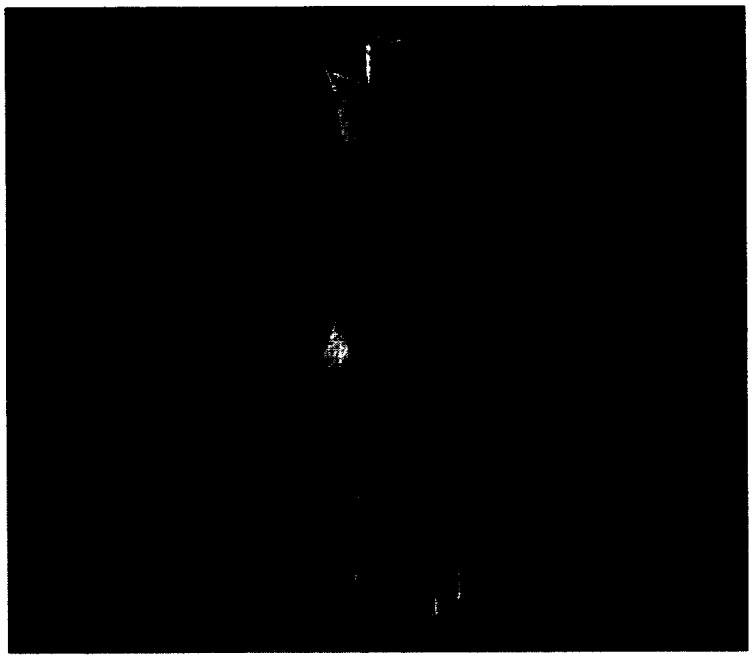

Figure III.7 Low-speed axial-flow compressor stator.

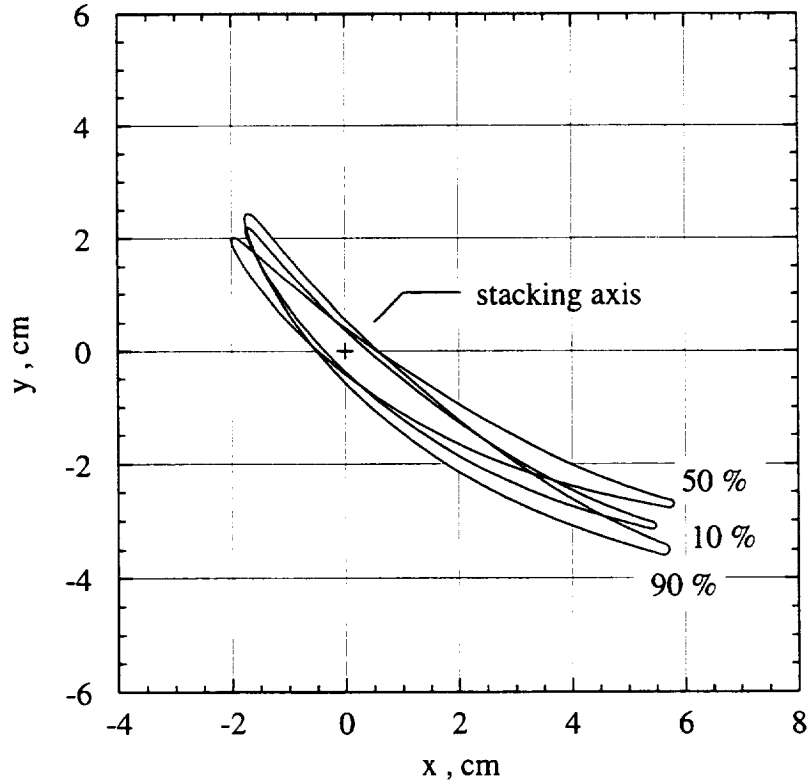

Figure III.8 Stator airfoil sections at 10, 50 and 90% span.

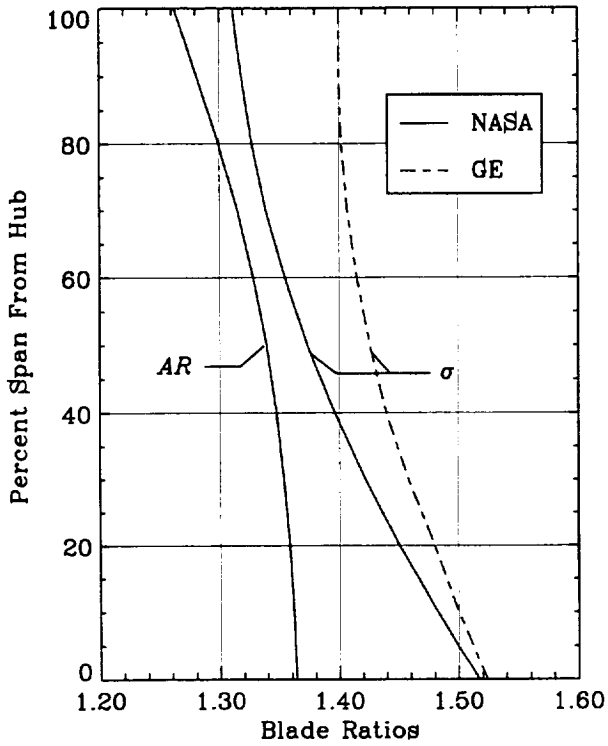

Figure III.9 Radial distributions of stator solidity and aspect ratio.

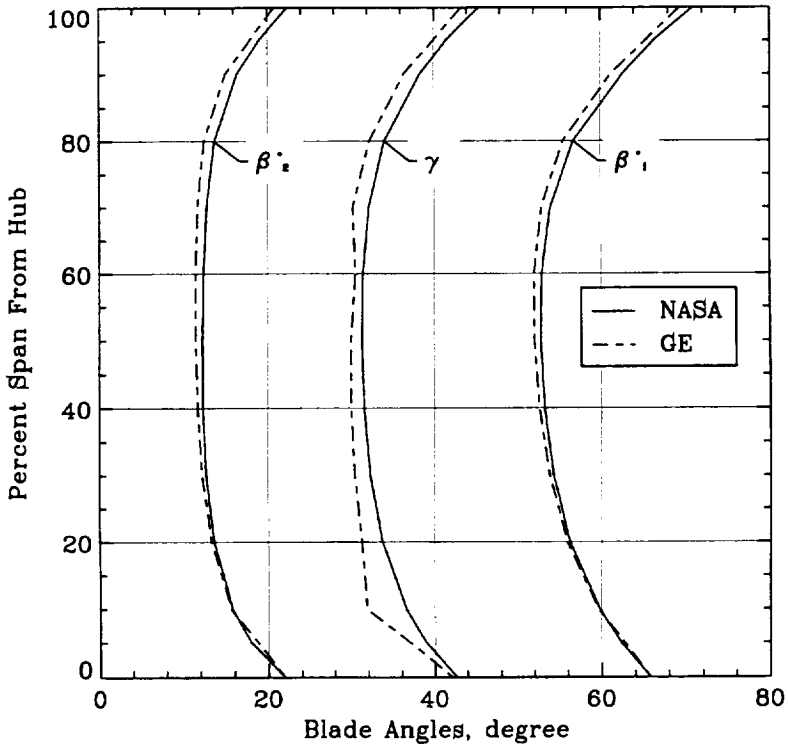

Figure III.10 Radial distributions of stator leading edge, trailing edge and setting angles.

CHAPTER IV

DATA REDUCTION AND ANALYSIS PROCEDURES

Overall Performance Parameters

Overall performance data include the compressor pressure rise characteristic, work coefficient and efficiency deduced from static pressure and shaft torque measurements. These are all given with respect to flow coefficient, defined as the mean inlet velocity normalized by the tip speed. The discussion of overall performance parameters follows closely that presented by Wisler [16] but is included here for completeness.

Flow coefficient was computed from the measured airflow using Equation IV.1. The massflow rate ($\dot{m}$) was calculated from Equation IV.2 where Cd represents a previously determined discharge coefficient dependent upon the Reynolds number and $\dot{m}_{1d}$ represents the theoretical one-dimensional massflow rate. The density and velocity at Station 0.1 were determined from compressible flow relations assuming isentropic flow from the bellmouth and constant static pressure at Station 0.1. Stagnation properties for Equation IV.2 were obtained from the reference conditions measured upstream of Station 0.1, while the static pressures were taken from an average of casing and hub pressure measurements at Station 0.1.

$$\phi = \frac{\dot{m}}{\rho_{ref}\, A_{0.1}\, U_{tip}} \tag{IV.1}$$

$$\dot{m} = C_d\, \dot{m}_{1d} = C_d\, (\rho_{0.1}\, A_{0.1}\, V_{0.1})_{1d} \tag{IV.2}$$

The pressure rise coefficient is defined by Equation IV.3. Here, ψ' truly represents an isentropic enthalpy rise: however, the rise in enthalpy was calculated from the pressure rise as given in Equation IV.4. For this calculation it was assumed that the rise in static pressure equaled the rise in stagnation pressure. The average inlet and outlet pressure measurements were obtained from casing and hub static taps positioned ahead of the first rotor and behind the last stator.

$$\psi' \equiv \frac{(H^o_{out} - H^o_{in})_{isen}}{\frac{1}{2}\, U^2_{tip}} \tag{IV.3}$$

$$(H^o_{out} - H^o_{in})_{isen} = \frac{\gamma}{\gamma - 1}\left(\frac{P_{ref}}{\rho_{ref}}\right)\left[\left(\frac{P_{out}}{P_{in}}\right)^{\frac{\gamma-1}{\gamma}} - 1\right] \tag{IV.4}$$

The work coefficient is defined in Equation IV.5. The actual enthalpy rise was calculated using Equation IV.6. Here, Tq is the measured torque while Tq_{tare} is the tare torque which was previously determined.

$$\psi = \frac{(H^o_{out} - H^o_{in})}{\frac{1}{2} U^2_{tip}} \tag{IV.5}$$

$$(H^o_{out} - H^o_{in}) = \frac{(Tq - Tq_{tare})\, w\, g_c}{\dot{m}} \tag{IV.6}$$

The efficiency was calculated by taking the ratio of the pressure rise coefficient to work coefficient (Equation IV.7).

$$\eta = \frac{\psi'}{\psi} \tag{IV.7}$$

Individual Stage Performance Parameters

Stage performance data include stage pressure rise characteristics along with radial distributions of stage pressure rise coefficient, work coefficient and efficiency. Pressure rise characteristics were deduced from casing static pressures, while stage performance parameters were obtained from pneumatic probe measurements.

The stage pressure rise characteristics were calculated by using Equation IV.4, where the inlet and outlet conditions corresponded to the appropriate static pressures for each stage. As with overall performance parameters, the stage characteristics are given with respect to inlet flow coefficient. Note that the inlet flow coefficient corresponds to the inlet of the machine and not the inlet to a particular stage. Hence, no corrections to the data were made which accounted for differences in the local flow coefficient which were caused by density changes. A quick analysis, assuming a 100% efficient machine at peak pressure, showed that the maximum discharge density was only 1.8% higher than the inlet density. Therefore, only small changes to the slope of the stage characteristics were expected due to changes in the local flow coefficient.

Stage performance parameters were defined exactly as overall performance parameters. Radial distributions of these parameters were obtained by circumferentially mass averaging appropriate flow quantities obtained from pneumatic probes. For the stage pressure rise coefficient, total instead of static pressures were used to set the outlet-to-inlet pressure ratio in Equation IV.4. Euler's equation (Equation IV.8) was employed across a rotor to determine the actual enthalpy rise in Equation IV.6.

$$(H^o_{out} - H^o_{in}) = (UV_\theta)_{out} - (UV_\theta)_{in} \tag{IV.8}$$

Radial movement of fluid particles through the rotor was accounted for when using Euler's equation. Therefore, inlet and outlet values of wheel speed and tangentail velocity in Equation IV.8 correspond to the same streamline. Spanwise shifting of

streamlines was determined from the measured distributions of axial velocity. Velocities were computed from measured total pressures, static pressures and flow angles using compressible flow relations. Total pressures were measured with miniature kiel-headed probes. Wedge probes were used to acquire the static pressure and flow angle at each radial and circumferential position.

Blade Element Performance Parameters

Blade element performance data provide two-dimensional cascade parameters and stage vector diagram quantities. All values were calculated from total pressures, static pressures and flow angles measured in a matrix of circumferential and radial positions. Data was taken at the rotor inlet, stator inlet and stator discharge for the third stage. These locations correspond to Stations 3.0, 3.5 and 4.0 respectively as shown in Figure III.1.Total pressures were acquired with a miniature kiel-head probe. Static pressures and flow angles were gathered with wedge probes. See Appendix B for a detailed discussion of probe calibration and data reduction proceedures. Appropriate absolute flow quantities were either area or mass averaged across one stator pitch to give the radial distributions of the circumferentially averaged flow. For rotor performance, total pressures were first converted to the relative frame at each measurment location and then averaged.

Inlet and outlet vector diagram quantities are presented for both the rotor and stator. Velocities and flow angles are shown relative to the blade in question. Velocities at each measurement location were calculated from the measured pressures using compressible flow relations. To calculate velocities, the pressures were corrected to standard day conditions and the total temperature (standard day condition) was assumed to be constant across the span. Velocity components at each position were found by multiplying the velocity magnitude with the appropriate trigonometric function of the measured flow angle. The circumferential averaged axial velocity was found from area averaging the axial velocity while the tangential velocity was mass averaged. The averaged velocity magnitude (Equation IV.9) and flow angle (Equation IV.10) were calculated from the area averaged axial velocity and mass averaged tangential velocity. Relative velocity triangle values corresponed directly to the averaged absolute values through the local wheel speed.

$$\overline{V} = \sqrt{\left(\overline{V_Z}\right)^2 + \left(\overline{V_\theta}^m\right)^2} \tag{IV.9}$$

$$\overline{\beta} = \tan^{-1}\left(\frac{\left(\overline{V_\theta}^m\right)}{\left(\overline{V_Z}\right)}\right) \tag{IV.10}$$

The two-dimensional cascade parameters presented are incidence, deviation, turning angle, diffusion factor, loss coefficient and loss parameter. Radial distributions of turning angle were calculated from the axisymmetric inlet and exit flow angles. The diffusion factor, defined in Equation IV.11, was determined from the appropriate averaged velocities. For the loss coefficient (Equation IV.12) the inlet and outlet total pressures were mass averaged across one stator pitch, while the static pressure was simply area averaged. When presenting circumferential distributions of loss coefficient the outlet total pressures were not averaged, but the inlet pressure values were. The loss parameter (Equation IV.13) is as given in Reference [17].

$$DF = 1 - \frac{\overline{V}_{out}}{\overline{V}_{in}} + \frac{\Delta \overline{V}_{\theta}^{m}}{2\sigma \overline{V}_{in}} \tag{IV.11}$$

$$\omega = \frac{\overline{P^o}_{in}^{m} - \overline{P^o}_{out}^{m}}{\overline{P^o}_{in}^{m} - \overline{P}_{in}} \tag{IV.12}$$

$$\omega_p = \frac{1}{2}\,\omega\,\frac{\cos\overline{\beta}_{out}}{\sigma}\left(\frac{\cos\overline{\beta}_{out}}{\cos\overline{\beta}_{in}}\right)^2 \tag{IV.13}$$

Seal-Tooth Leakage Rate Estimation

To estimate the maximum leakage through the labyrinth seal for a given clearance, Equation IV.14 was used. For this estimation, the nominal clearance gap and the upstream and downstream static pressures, measured by static pressure taps on the foot-ring, were known. The discharge coefficient, Cd, was found from Equation IV.15, which was taken from Reference [7].

$$\frac{\dot{m}_l}{\dot{m}} = Cd\left(\frac{A_\epsilon/A}{\sqrt{1-(A_\epsilon/A_1)^2}}\right)\frac{\sqrt{Cp_1 - Cp_2}}{\phi} \tag{IV.14}$$

$$Cd = 0.102\,\log\left(\frac{b}{\epsilon}\right) + 0.719 \tag{IV.15}$$

Equation IV.14 was derived by applying the conservation equations to the control volume defined in Figure IV.1. In the derivation flow was assumed to be incompressible and traveled isentropically from position (1) to the seal-tooth contraction. The static pressure distributions across the control volume inlet and outlet boundaries were considered uniform. The static pressure at the seal-tooth contraction equaled the static

pressure measured at (2). Finally the whirl was assumed constant from (1) to the seal-tooth contraction.

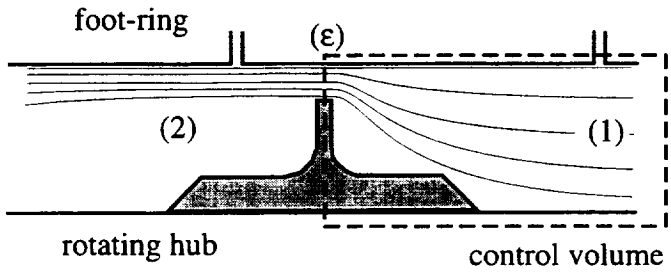

Figure IV.1 Schematic for seal-tooth leakage rate estimation.

CHAPTER V

CONFIGURATIONS TESTED

To fulfill the objectives of this study five compressor configurations were tested. For each of these configurations, changes were made to the shrouded stator hub geometry which either modified the leakage rate through the labyrinth tooth seal or removed the presence of the shrouded stator cavities altogether. For the first set of tests, Part 1, these modifications were incorporated on all four stages of the compressor. For the second set of tests, Part 2, alterations were made only to the third stage while the other stages (1,2 and 4) were kept at the baseline configuration. The configurations were chosen to give the following cases:

1. No shrouded stator cavities and no labyrinth seal-tooth leakage (No cavity / No leakage)
2. Minimized labyrinth seal-tooth leakage with shrouded stator cavities (Minimized leakage)
3. Baseline labyrinth seal-tooth leakage with shrouded stator cavities (Baseline leakage)
4. Increased labyrinth seal-tooth leakage with shrouded stator cavities (Increased leakage)
5. Maximum labyrinth seal-tooth leakage with shrouded stator cavities (Maximum leakage)

These modifications to the shrouded stator geometry are illustrated in Figure V.1. For the no cavity / no leakage configuration (Figure V.1a) wood extensions were attached to the stator foot-ring in order to remove the presence of the shroud cavities. In an attempt to eliminate seal-tooth leakage, a balsa strip was adhered to the foot-ring and the labyrinth seal-tooth was shimmed outwards. In theory this produced zero (or negative) clearance between the balsa strip and seal-tooth. In practice this created the minimum clearance attainable with this facility, since the seal-tooth wore into the balsa strip which generated a small clearance between the balsa and seal-tooth. This clearance was made somewhat larger due to 1) the lifting and axial movement of the rotor drum from rest to operating condition and 2) the machining tolerences and runout of the rotor drum and annular foot-ring. (It must be noted that foam face-seals were also tried in the rig to eliminate leakage, but these failed miserably.) For this configuration, the seal-tooth clearance was always the smallest of all throttling points in the shrouded stator cavity (the other two created by the wood extensions). For the minimized leakage configuration (Figure V.1b), the wood extensions were removed and the compressor was reassembled with the balsa strip and shimmed seal-tooth still in place. It is important to remember that some

seal-tooth clearance was present for this configuration. The other three configurations (Figure V.1c) were attained by simply adjusting the shimmed seal-tooth height until the proper seal-tooth clearance was obtained. For these three configurations the balsa strip was removed from the foot-ring and replaced with a strip of cherry wood, thereby eliminating any wear which previously occurred on the bottom of the foot-ring. Finally, all configurations were tested with stator blade ends (interface between the blade tip and case and the blade hub and annular foot-ring) sealed.

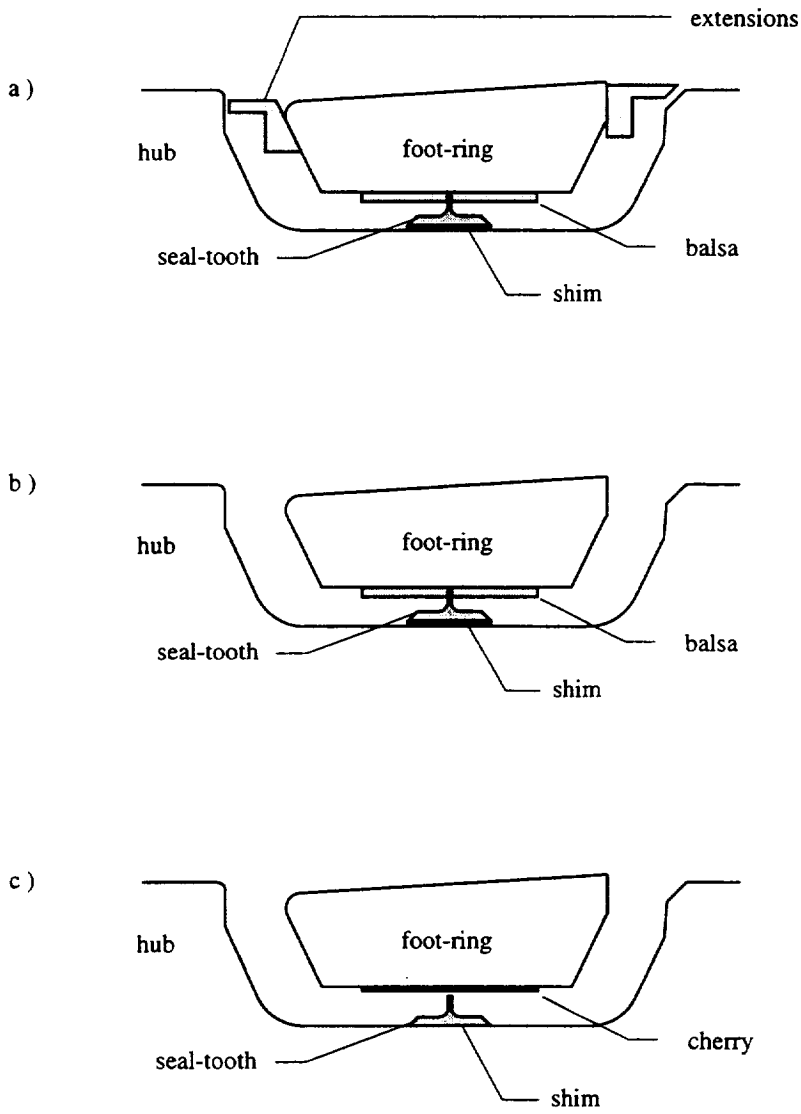

Figure V.1 Illustrations of configurations having a) no cavity with no leakage, b) cavity with minimized leakage and c) cavity with baseline, increased and maximum leakage.

Table V.1 Measured seal-tooth clearances for the first set of tests conducted on the LSAC.

Configuration	Seal-Tooth Clearance, ϵ / h, %				
	Stage 1	Stage 2	Stage 3	Stage 4	Nominal
No cavity / No leakage	0.54	0.19	0.21	0.06	0.25
Minimized leakage	0.54	0.19	0.21	0.06	0.25
Baseline leakage	0.67	0.42	0.69	0.46	0.56
Increased leakage	1.35	1.13	1.29	1.17	1.23
Maximum leakage	2.02	1.79	1.96	1.83	1.90

Table V.2 Measured seal-tooth clearances for the second set of tests conducted on the LSAC.

Configuration	Stage 3 Seal-Tooth Clearance, ϵ / h, %
No cavity / No leakage	0.46
Minimized leakage	0.46
Baseline leakage	0.71
Increased leakage	1.23
Maximum leakage	1.96

For both sets of experiments, seal-tooth clearances were measured statically at the 12 and 6 o'clock positions before and after each configuration change. The casing was composed of two halfs with the the split line running vertically. Removal of one half of the casing therefore allowed the easy measurement of clearances. These measured clearances are listed in Table V.1 for the first series of tests and in Table V.2 for the second series of tests. The values are nondimensionalized by the blade span (12.19 cm) for convenience. Both tables indicate that for each individual stage, the no cavity / no leakage clearance was equal to the minimized leakage clearance. This is because the same balsa strips and seal-tooth shims were used for these two configurations. Table V.1 shows for a given configuration the clearance values varied greatly between all four stages. This was caused by machining tolerances on the rotor and foot-ring concentricities and run-out of the cantilevered rotor drum. To obtain mean values, averages were taken for all four stages. These averages are represented by the nominal values given in TableV.1.

An analysis was conducted to correlate the changes in the seal-tooth clearance to the changes in seal-tooth leakage massflow. Figure V.2 displays the results of the analysis

for two operating conditions (near peak efficiency and increased loading). Here, the percent normalized massflow (estimated by Equation IV.14) is plotted against the percent clearance ratio. Each point represents the four stage average of the calculated massflow values and the measured clearance values for the first experiment (Part 1). For both flow conditions, the relation between normalized massflow and clearance ratio was nearly linear, since the discharge coefficient and the difference in pressure across the seal-tooth varied only slightly with each configuration. The slight inconsistency in slope, between the two sets of data, resulted from the obvious change in the pressure difference across the seal-tooth due to the different operating conditions. As shown in Figure V.2, some seal-tooth leakage was present for the minimized leakage configuration, since a small amount of clearance was present for that configuration. The no cavity / no leakage configuration had nearly no mass flowing through the seal-tooth. It appears the extensions, which were installed on the foot-ring to remove the upstream and downstream cavity (Figure V.1), acted as throttling devices and actually reduced the massflow through the seal-tooth even though the seal-tooth clearance was identical to the minimized leakage configuration clearance.

Existing literature indicates the ranges of seal-tooth massflow ratio tested were well within the bounds set by current engine design practice [7]. The baseline configuration produced a leakage rate (nominally 0.45% of the power stream massflow) which could be found in aircraft core compressors utilizing current sealing technology [18]. The baseline leakage rate was also comparable to that quoted by Adkins and Smith [8]. The

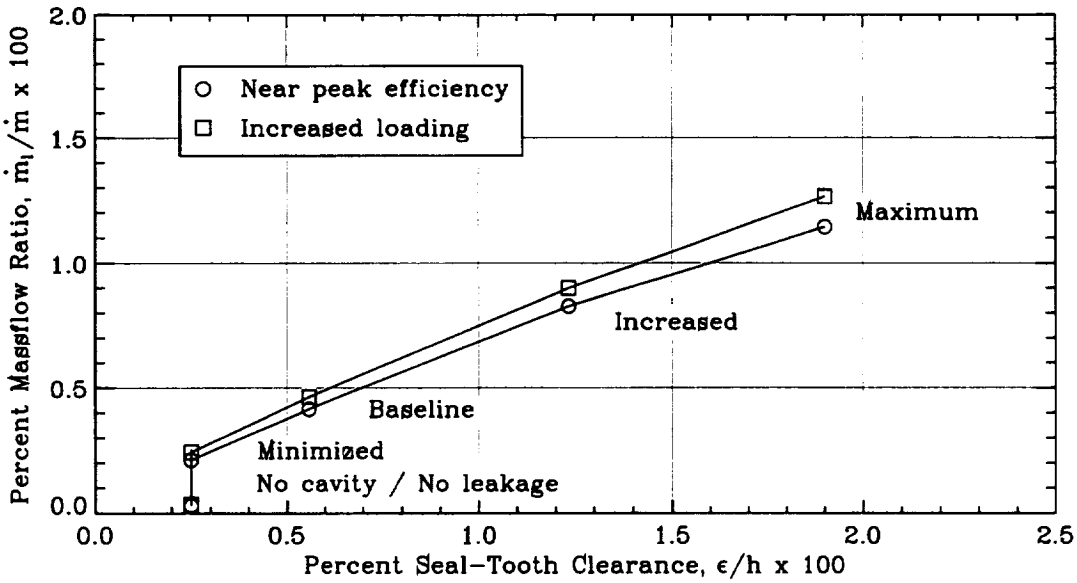

Figure V.2 Correlation between nominal seal-tooth massflow and the nominal clearance values for the first experiment (Part 1).

no cavity / no leakage and minimized leakage configurations could represent leakage rates obtained in advanced sealing technologies such as brush seals [19]. The increased leakage configuration approximately doubled the baseline clearance (and hence doubled leakage), while the maximum leakage configuration tripled the baseline clearance. Both of these cases represent leakage rates which may occur when labyrinth seal-teeth wear.

CHAPTER VI

RESULTS AND ANALYSIS OF DATA: PART 1

This chapter reviews the overall, stage and blade element performance data acquired when configuration changes where made to all four stages of the compressor simultaneously. Each of the five configurations listed in Chapter V were tested. Overall and stage performance measurements were gathered over most of the operating range of the compressor. The collection of radial and circumferential distributions of blade element performance data was concentrated on the third stage at two operating conditions. Measurements with modifications made to only the third stage geometry are discussed in Chapter VII.

Overall Performance

Overall performance data were acquired to determine the gross effects of seal-tooth leakage on compressor operation. These data were obtained while establishing speed lines at the beginning and end of each run day. Data were recorded over most of the operating range near 100% design speed. The results presented for each configuration are an arithmetic average of seven separate sets of data. Detailed data uncertainty estimates are discussed in Appendix A.

The systematic influence of each configuration change on the compressor pressure rise coefficient is shown in Figure VI.1. As seen, the compressor characteristic was affected over most of the operating range by each configuration change. Near peak efficiency ($\phi = 0.395$) a 4% decrease in pressure rise occurred when going from no cavity / no leakage to maximum leakage. At increased loading ($\phi = 0.350$) the difference was nearly 6%. Figure VI.2 shows that the decrease in pressure rise was nearly linear with respect to the seal tooth clearance for near peak efficiency and increased loading operation. Here, the no cavity / no leakage configuration data were used to normalize the decrease in pressure rise. The no cavity / no leakage configuration was also assumed to be the zero clearance case.

Figure VI.1 suggests insignificant change in the flow coefficient where stall first occurred ($\phi \approx 0.295$) with the different configurations. For the no cavity/no leakage, baseline leakage and maximum leakage cases, the data include the last acquired data point before dropping into stall. The slight differences in the stall inception flow coefficient for the minimized leakage and increased leakage cases were caused by binding friction of the throttle sleeve valve which controlled the massflow through the compressor. The binding of the throttle valve made it extremely difficult to close the valve smoothly (only at one mechanical position) and hence the compressor would either slowly slide or jump

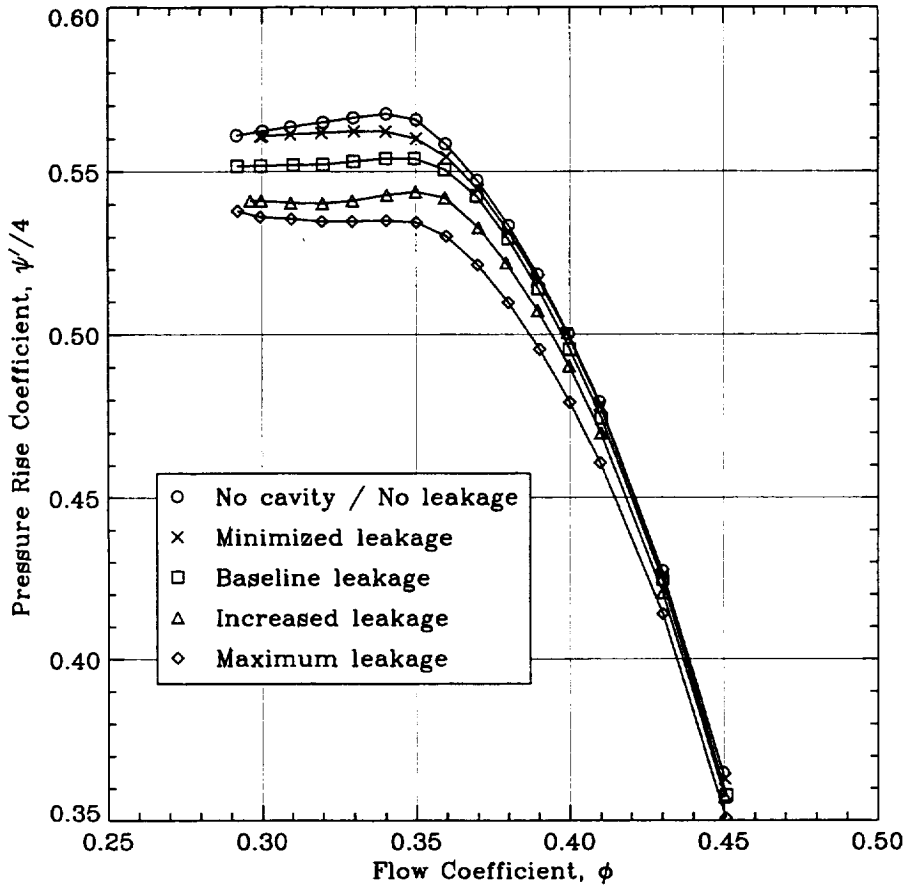

Figure VI.1 Overall pressure rise characteristics for the five test configurations.

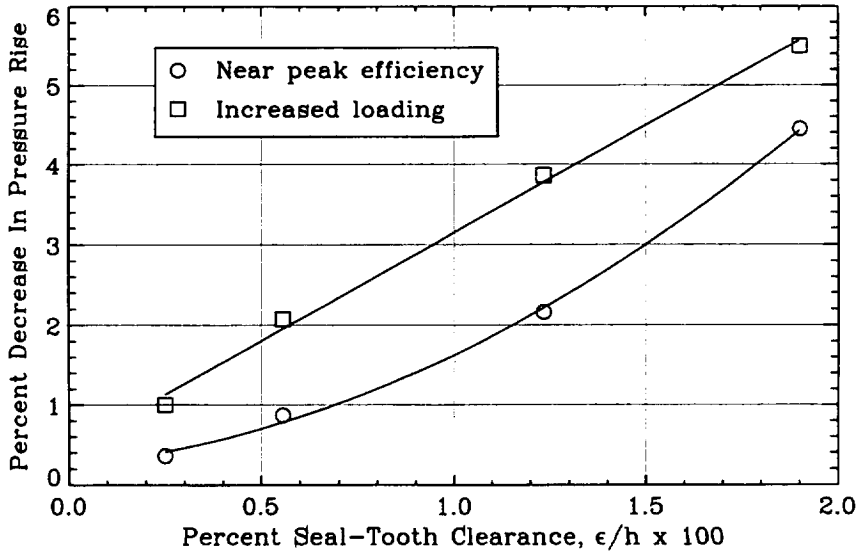

Figure VI.2 Overall pressure rise penalties at two operating conditions.

into stall after the valve was able to overcome the binding friction. It is unfortunate that the binding occurred for two of the configurations; however, from the other three cases, it could be assumed that neither the leakage rate nor the presence of the cavity had much influence on the stall inception point of this compressor.

The variation in compressor work coefficient with configuration change is given in Figure VI.3. For the two largest leakage cases there was a noticeable drop in work input across the entire operating range; however, the basic shape of these curves did not change. Figure VI.4 shows that the decrease in work input varied nearly linearly with seal-tooth clearance for two operating conditions. It is interesting to note that work input and pressure rise both decreased with increasing clearances, with the percentage decrease in work input about half that of the pressure rise.

The above discussion leads to the conclusion that increasing seal-tooth leakage tends to decrease efficiency. This is demonstrated in Figure VI.5. The efficiency level was affected over most of the operating range for each configuration. Near peak efficiency two points were lost when going from no cavity / no leakage to maximum leakage. At increased loading a decrease of nearly 2.5 points occurred. Figure VI.6 shows the expected linear fit of the decrease in efficiency with the increase in seal-tooth clearance. Figure VI.6 also indicates good consistency with data presented by Ludwig [1] for a compressor with shrouded stators and multiple (two) non-stepped labyrinth teeth.

Loss in compressor efficiency when rotor and stator endwall clearances are increased is generally accepted. Many studies have established this. A common rule for rotor blades is to expect a 1.5 point drop in efficiency for each 1% increase in the tip clearance to span ratio (a slope of 1.5) [7,1,2,20]. Multistage machines have been reported to have efficiency penalty slopes as high as 2.0 for changes in rotor tip clearances [1]. For cantilevered stators these slopes range from 1.0 for large clearances ($\epsilon/h > 1.0\%$) to 2.0 for tight clearances ($\epsilon/h < 1.0\%$) [7,1,3]. Larger clearances are the norm for cantilevered stators. The data from this compressor suggest efficiency penalty slopes of 1.0 for seal-tooth clearance changes, which are only slightly lower than most reported values for rotors and equal to the values reported for cantilevered stators used in practice. Therefore, when predicting compressor performance, it appears that it is equally important to account for the effects of seal-tooth leakage as it is to include the consequences of rotor tip clearance flows or cantilevered stator hub clearance flows.

In the above discussions, reductions in pressure rise, work input and efficiency were all satisfactorily correlated with increasing seal-tooth clearance. This was done out of convenience and has, in the past, been favored by many investigators because of its simplicity and practicality. The clearance was nondimensionalized by the blade span to also follow past convention. It is important to remember, though, that the aerodynamic parameter altered by the various configurations was the massflow through the seal-tooth.

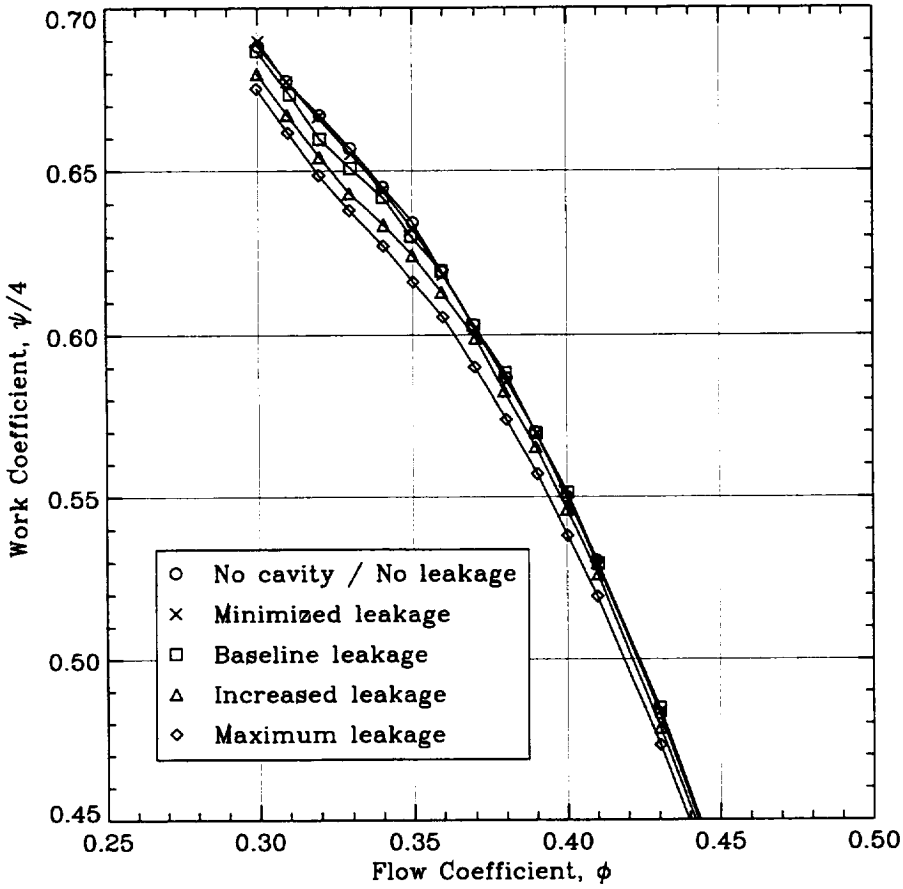

Figure VI.3 Overall work coefficient for the five test configurations.

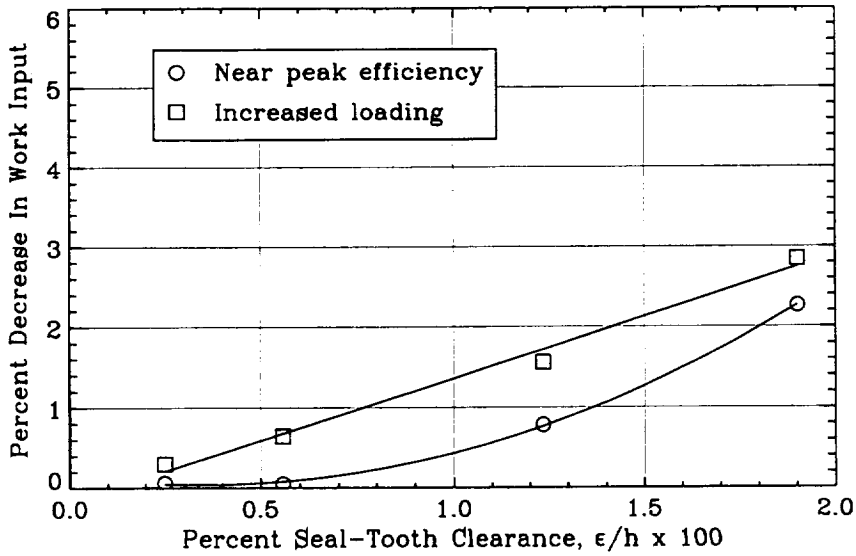

Figure VI.4 Decrease in overall work input at two operating conditions.

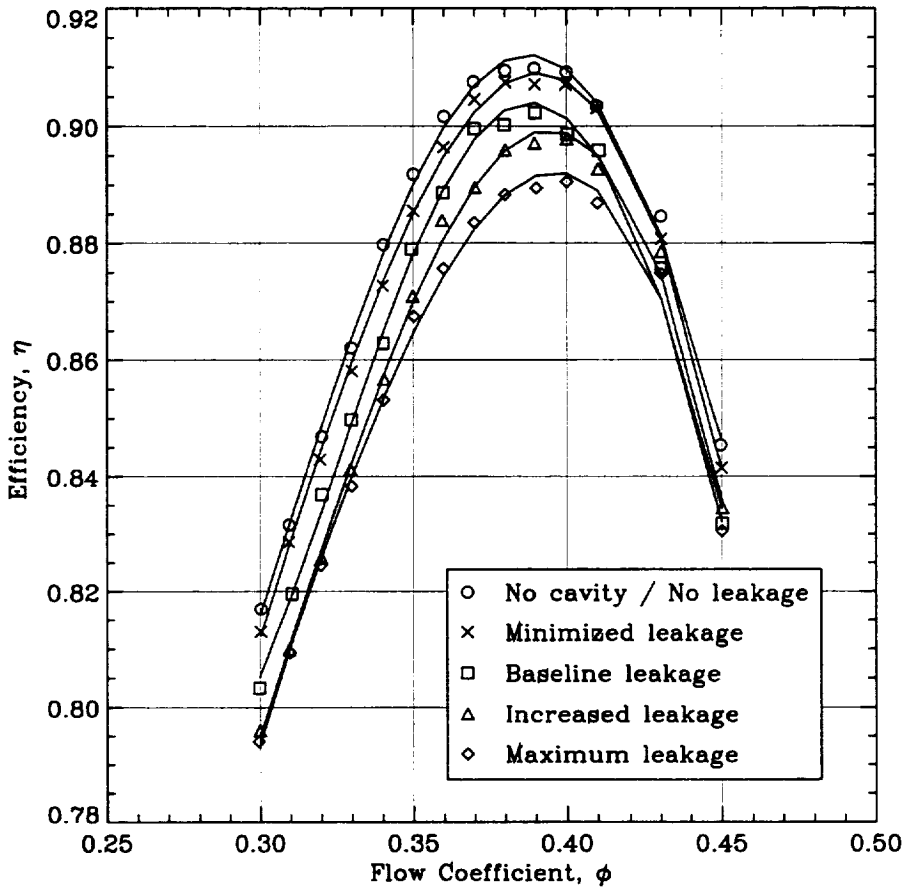

Figure VI.5 Overall efficiency curves for the five test configurations.

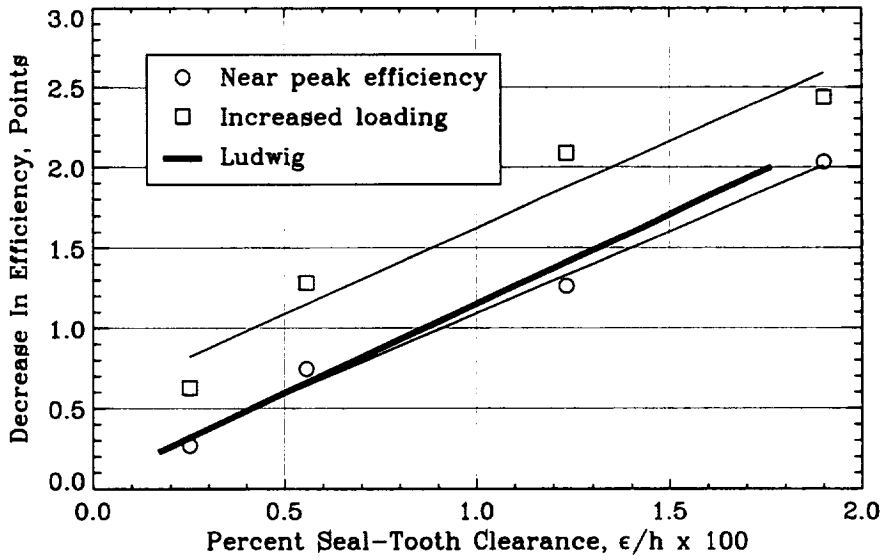

Figure VI.6 Overall efficiency decrease at two operating conditions.

Figure VI.7 Estimated performance improvements
when shrouded stator cavities were removed.

Performance Parameter	Extrapolated Performance Values	
	Near Peak Efficiency	Increased Loading
Pressure Rise Coefficient, ψ'	0.30 %	0.45 %
Work Coefficient, ψ	0.00 %	-0.20 %
Efficiency, η	0.10	0.55

Luckily, seal-tooth massflow varied nearly linearly with seal-tooth clearance (Figure V.2), therefore, performance penalties could also be easily correlated to increasing seal-tooth massflow.

The shrouded stator cavities themselves appeared to have little influence on the overall performance of this compressor. This was determined by extrapolating the curves given in Figures VI.2,VI.4 and VI.6 to zero clearance and hence no seal-tooth leakage. The vertical intercept of each curve gave an estimation of the effects of the presence of the shrouded stator cavities alone (without seal-tooth leakage) on the individual overall performance values since the no cavity / no leakage data was used as the zero clearance case and since the no cavity / no leakage configuration had virtually no leakage as demonstrated in Figure V.2. The performance gains which could be expected if the shrouded stator cavities were removed are listed in Table VI.7 for both operating conditions. The largest gain in performance would be a 0.45% increase in pressure rise and 0.55 point increase in efficiency for increased loading operation. Unfortunately, the scatter and uncertainty in the efficiency data could account for the improvement and therefore the attribution of the gain to the removal of the cavities could be questioned.

Individual Stage Performances

Stage pressure characteristic data were acquired for the five test configurations for all four stages. These pressure characteristics were obtained concurrently with overall performance data. Again, detailed error estimates can be found in Appendix A.

Stage pressure rise characteristics are shown in Figure VI.8. Two trends should be noted. First, increasing seal-tooth leakage lowered the pressure rise of all stages. Second, the stage performance degradation became progressively worse in downstream stages. This is better illustrated in Figures VI.9 and VI.10, where the percent decrease in pressure rise is shown for each stage at two operating conditions. Curves representing the overall performance data are reproduced in these figures as bold face lines. Both figures suggest a definite trend in which downstream stages suffer more degradation than

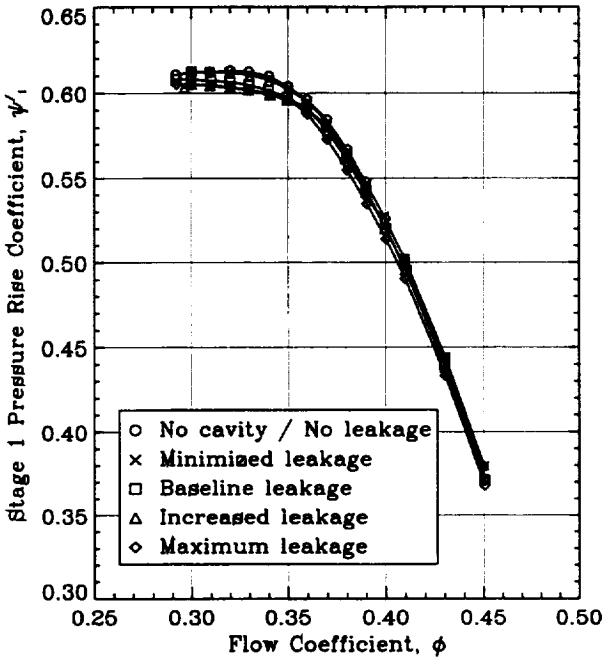

a) Stage 1 characteristics

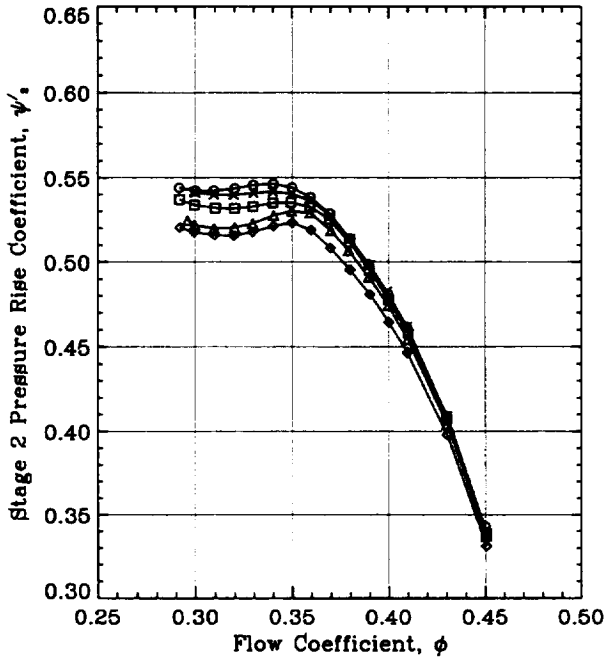

b) Stage 2 characteristics

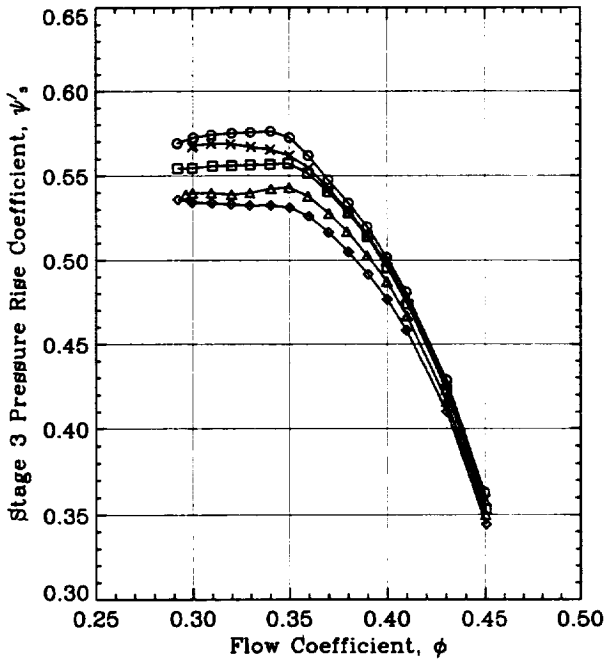

c) Stage 3 characteristics

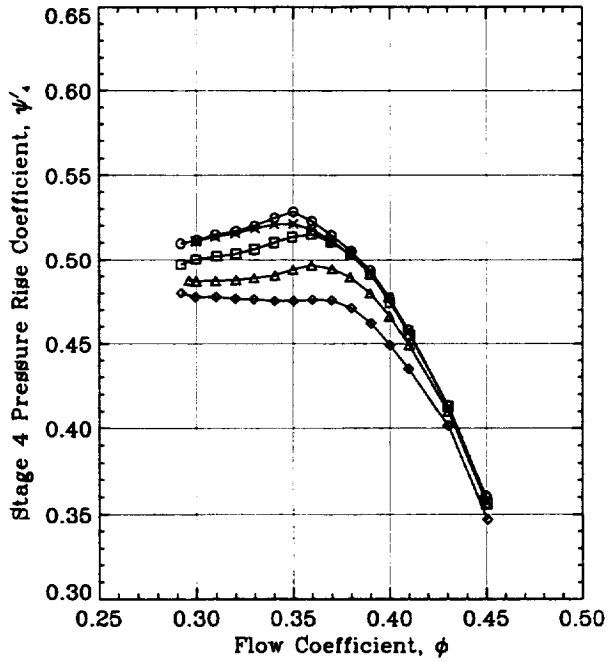

d) Stage 4 characteristics

Figure VI.8 Stage pressure rise characteristics for the five test configurations.

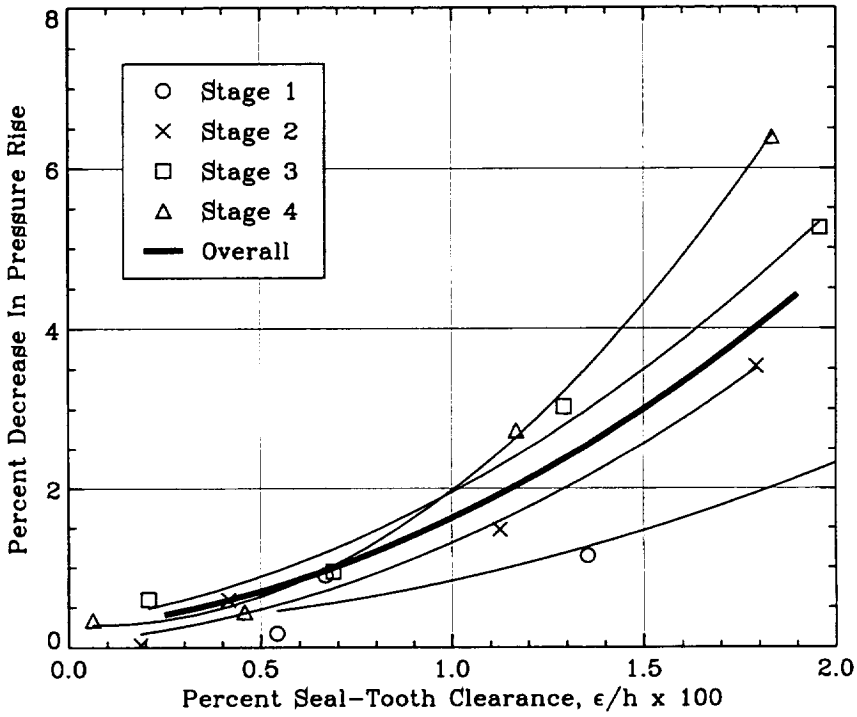

Figure VI.9 Stage pressure rise penalties for near peak efficiency operation.

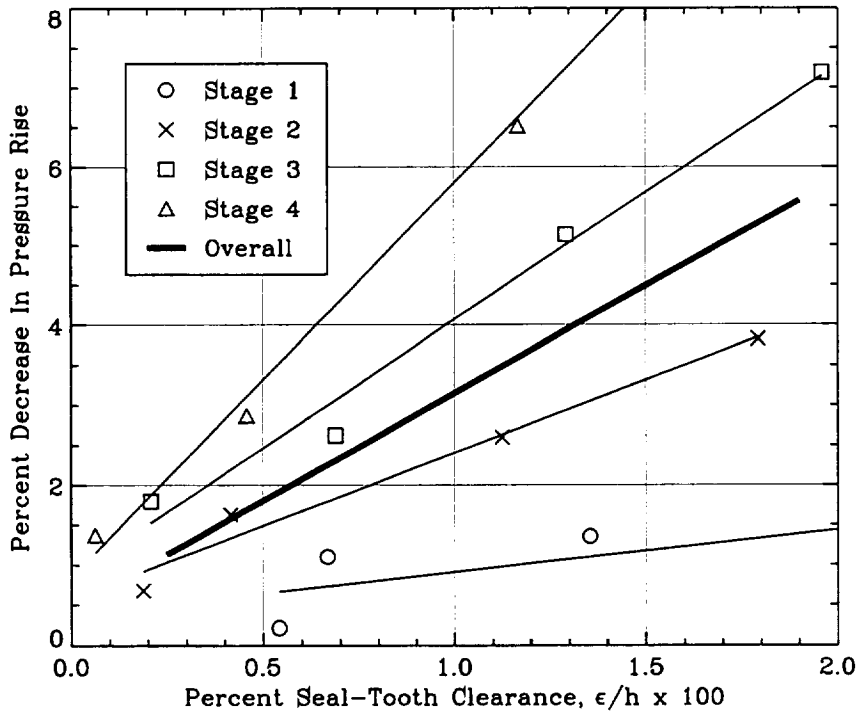

Figure VI.10 Stage pressure rise penalties for increased loading operation.

upstream stages. Near peak efficiency the trend was most noticeable at larger clearances ($\epsilon/h > 1.0\%$), while at increased loading operation it was present at all clearance values

It should be noted in passing that two concerns surfaced after studying these stage data. First, even near peak efficiency the apparent pressure decrease with increased leakage was large. How much of this decrease can be attributed to the fact that the inlet flow coefficient instead of the local flow coefficient, which changed for each configuration, was used as the abscissa? Second, the compressor design intent was to model a repeating stage environment. Why then, for the same seal-tooth clearance at the same operating condition, did the performance degradation progressively become larger in the downstream stages, instead of "leveling out" to a steady value?

The first concern was easily resolved by estimating the maximum possible change in the local flow coefficient for a given stage at a given operating condition. The analysis assumed that the local flow coefficient ratio (best case to worse case) was adequately approximated by Equation VI.1. This ratio became a maximum when the polytropic efficiency was 100%, which was an obvious upper bound to the approximation. The best-to-worse pressure ratio was taken from the compressor discharge static pressure values. The maximum change in the local flow coefficient was estimated to be less than 0.04%. A value of 0.04% seems quite reasonable, since a similar analysis determined that the compressor discharge flow coefficient was never larger than 1.8% of the inlet flow coefficient. Note 0.04% represents an extent much less than the size of the symbols in Figure VI.8. Furthermore, by assuming a characteristic slope ($\partial\psi'/\partial\phi$) of 2.5, the corresponding relative pressure change was less than 0.1%. Changes in the local flow coefficient were thus considered to have negligible effect on the apparent pressure rise decrease with seal-tooth leakage increase.

$$\left(\frac{\phi_b}{\phi_w}\right)_{max} = \left(\frac{\rho_w}{\rho_b}\right)_{max} = \left[\left(\frac{P_w}{P_b}\right)^{\frac{\gamma\eta_p-\gamma+1}{\gamma\eta_p}}\right]_{max} \qquad \text{(VI.1)}$$

The second concern was less easily dismissed. Before continuing, it is worthwhile to point out that the repeating stage environment is a hypothesized model of a multistage compressor individual stage flow field. The model postulates the velocity, pressure and temperature distributions leaving a stage are identical to those entering it, although the absolute levels of pressure and temperature are allowed to increase downstream. The concept is not new, and the pioneering work by many authors have shown it to be reasonably accurate. However, it might be presumptuous to assume that just because the blade geometries of a multistage machine are the same, the repeating stage environment will naturally develop within a few stages. Smith [21] has discussed at least three build-ups of a large low-speed four-stage axial-flow compressor which never developed a

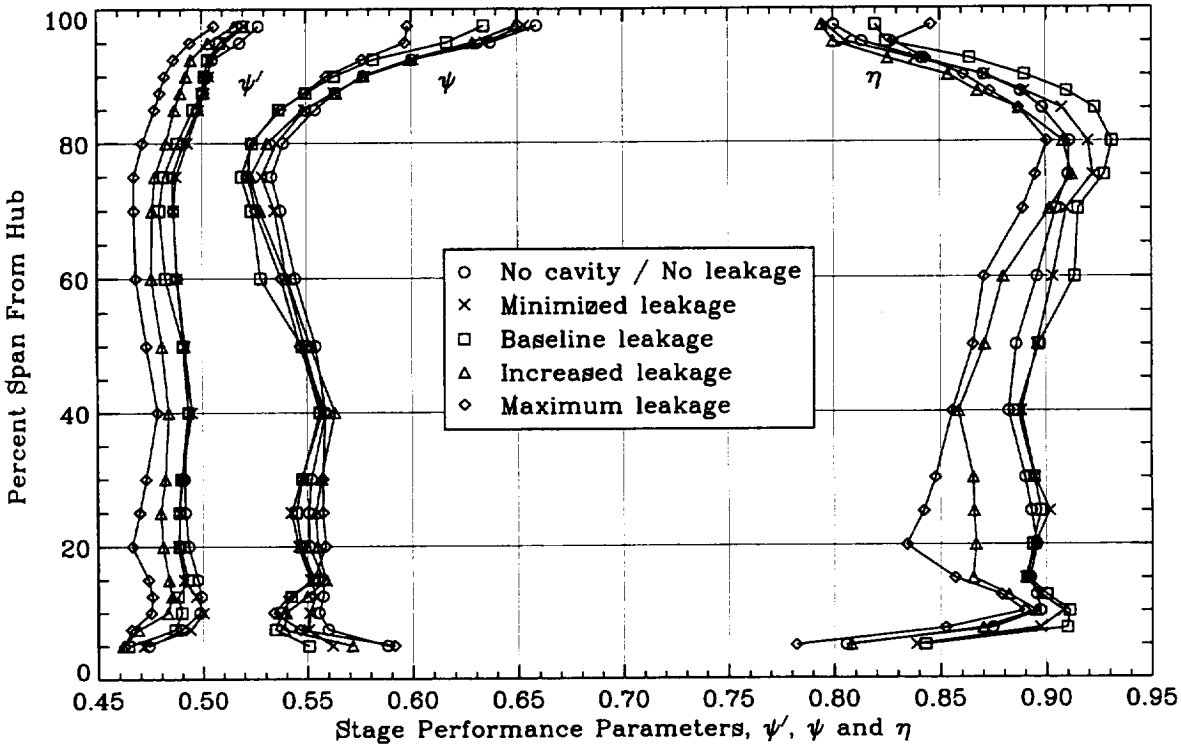

Figure VI.11 Third stage performance near peak efficiency operating condition.

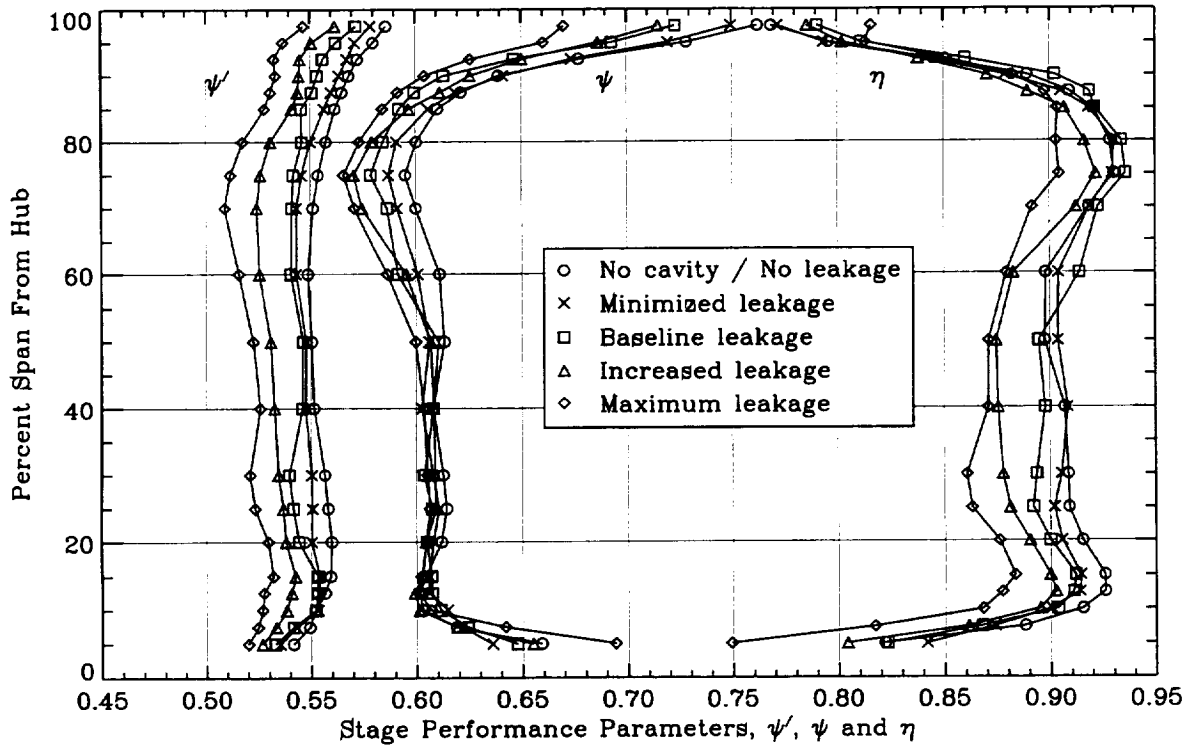

Figure VI.12 Third stage performance at increased loading operating condition.

repeating stage environment. The cause was blamed on the deterioration of the hub flow through all four stages. This deterioration of the hub flow was also believed, although not proven, to be the cause of the worsening of the performance of the nonrepeating downstream stages of our compressor.

Third Stage Performance Details

Detailed measurements to calculate the axisymmetric radial distributions of pressure rise, work input and efficiency for near peak efficiency and increased loading operating conditions were collected for the third stage only. These parameters were calculated using slow response pneumatic probe data collected over one stator pitch. Error estimates were not performed for these radial distributions of performance parameters.

The spanwise distributions of third stage performance data at near peak efficiency and increased loading operation are displayed in Figures VI.11 and VI.12, respectively. Both figures show a decrease in actual pressure rise (isentropic work input) across the entire span with increased seal-tooth leakage. Figure VI.12 clearly reveals that for increased loading the actual work input for the bottom half of the span was unchanged with increasing leakage, while substantial decreases in the actual work input occurred with increasing leakage over the upper 50% span. These trends are less clear in Figure VI.11, for near peak efficiency. Furthermore, the baseline work coefficient data above 50% span in Figure VI.11 are not consistent with the data for the other leakage amounts. This was caused by a small but uncorrectable error in the rotor discharge velocity measurements. The data are included in Figure VI.11 simply to expose the difficulty in obtaining work input measurements using conventional pneumatic probes. The efficiency distributions for both operating conditions indicated greatest efficiency reductions near the hub when leakage was increased. Efficiency distributions near the case were virtually unchanged provided the baseline data in FigureVI.11 are disregarded.

The radial distributions of stage performance data were mass averaged across the span in order to obtain representative single-valued stage performance quantities. The results of these calculations are shown in Figures VI.13 and VI.14. The trends of decreased pressure rise with increased leakage (Figure VI.13) are consistent with overall and stage performance data presented in Figures VI.2,VI.9 and VI.10. The stage efficiency penalty data (Figure VI.14) were a bit more scattered than for overall performance data (Figures VI.6); however, it was encouraging to find that the efficiency penalty slopes were nearly the same for overall and third stage data.

Circumferentially Averaged Third Stage Flow Details

Blade element data were gathered to quantify the changes in axisymmetric flow properties of the third stage with varying leakage. The data also help to explain how

the overall performance was influenced by each varying leakage. Area surveys with pneumatic probes were used to obtain these data. Measurements were concentrated in the inter-blade stations of the third stage with the data acquired in a matrix of 21 radial and 21 circumferential locations. Clustering of measurements near stator wakes and both endwalls allowed better definition of flow properties in those regions.

Both rotor and stator blade flow fields were substantially influenced by the amount of seal-tooth leakage. Data which support this statement are shown in Figures VI.15-

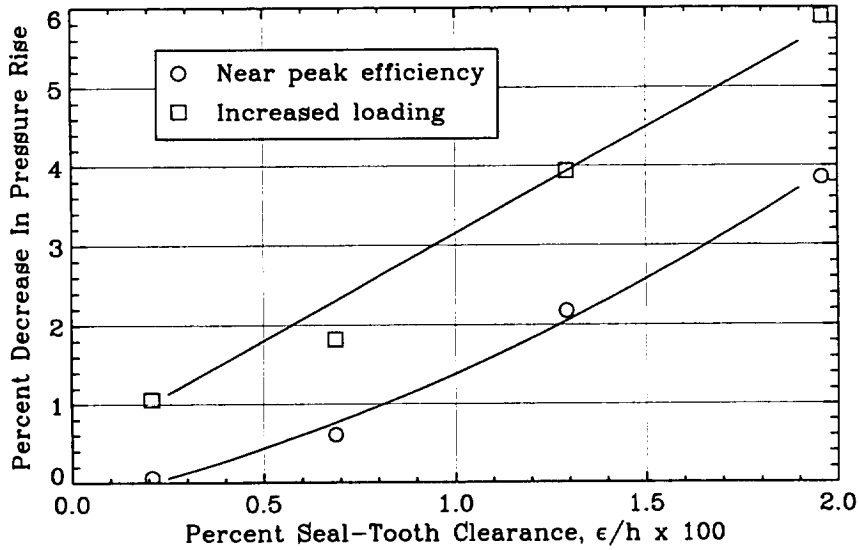

Figure VI.13 Third stage pressure rise penalties at two operating conditions.

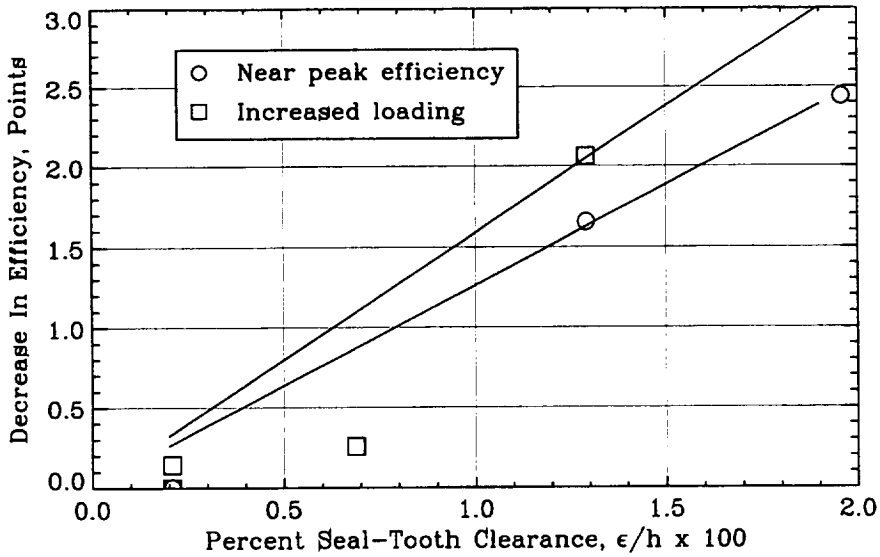

Figure VI.14 Third stage efficiency penalties at two operating conditions.

VI.18. Rotor and stator data for the near peak efficiency operating condition are shown in Figures VI.15 and VI.16, respectively. Data for to the increased loading condition are presented in Figures VI.17 (rotor) and VI.18 (stator). Similar tendencies in the data at both operating conditions are apparent. Discussion is therefore a combined view of what happened in common at both operating conditions. Furthermore, definite trends can be seen when sequentially viewing data from the no cavity / no leakage to maximum leakage configurations. Therefore to ease reading, the observed trends are always correlated to increasing seal-tooth leakage.

At the inlet to the third rotor a large deficit in axial velocity developed near the hub (5–25% span) when seal-tooth leakage increased while a slight decrease in the relative tangential velocity occurred over most of the span. Increased blockage near the hub forced the axial velocity across the rest of the span (30–100%) to increase. The reduction in the relative tangential velocity did not offset the decrease in axial velocity into the rotor hub (0–20% span) and consequently the rotor incidence (relative inlet flow angle) at the hub increased. Across the rest of the span (30–100%), the decrease in tangential velocity and the increase in axial velocity reduced the rotor incidence angles. These trends are clarified in Figure VI.19. Here, schematics of the stage velocity triangles are presented for the flow near the hub (VI.19a) and across the rest of the span (VI.19b). In Figure VI.19 note that solid lines correspond to the no cavity / no leakage configuration while dashed lines represent what occurred when seal-tooth leakage was increased.

The low axial velocity fluid near the hub mixed with surrounding fluid and streamlines shifted radially as it passed through the rotor and hence the hub blockage was not so concentrated in one region at the rotor discharge. Still, a substantial axial velocity deficit existed over the lower half of the span for the two largest leakage cases. For the lower 50% of span, the rotor discharge relative tangential velocity was decreased, while a slight increase occurred for the upper 50% of span with increased seal-tooth leakage (seen only in increased loading data). Rotor deviation values (relative exit flow angles) were only slightly altered with varying leakage, even though moderate variations in rotor incidence were present across the entire span. It should be noted there were differences in rotor deviation distributions (20–80% span) for the two operating conditions. Diffusion factor data show decreased rotor loading for the upper 50% span and increased loading for the lower 50%. This is consistent with velocity and flow angle data previously mentioned. It is also consistent with the notion that increased blockage at the hub forces more fluid to pass above, thereby unloading the tip and loading the hub as seen in Figures VI.11 and VI.12. Some changes in the rotor loss values occurred across most of the span when leakage changed. Near the tip, no definite trend was observable. Near mid-span, loss values were raised, while near the hub, they were significantly reduced. Although startling at first, the decrease in loss near the hub probably represents the radial shifting

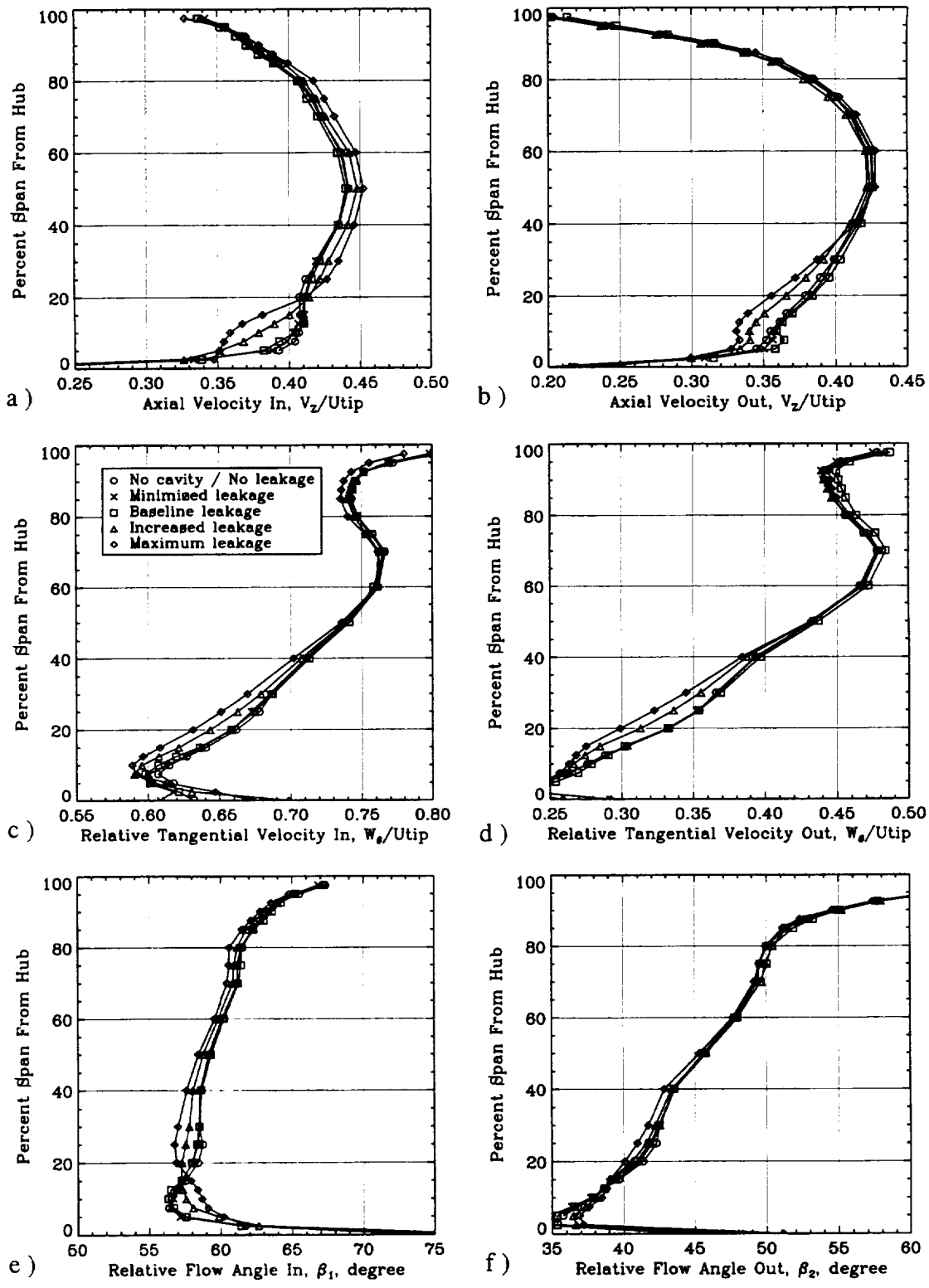

Figure VI.15 Rotor 3 blade element performance near peak efficiency operating condition: a) and b) axial velocity, c) and d) relative tangential velocity, e) and f) relative flow angle.

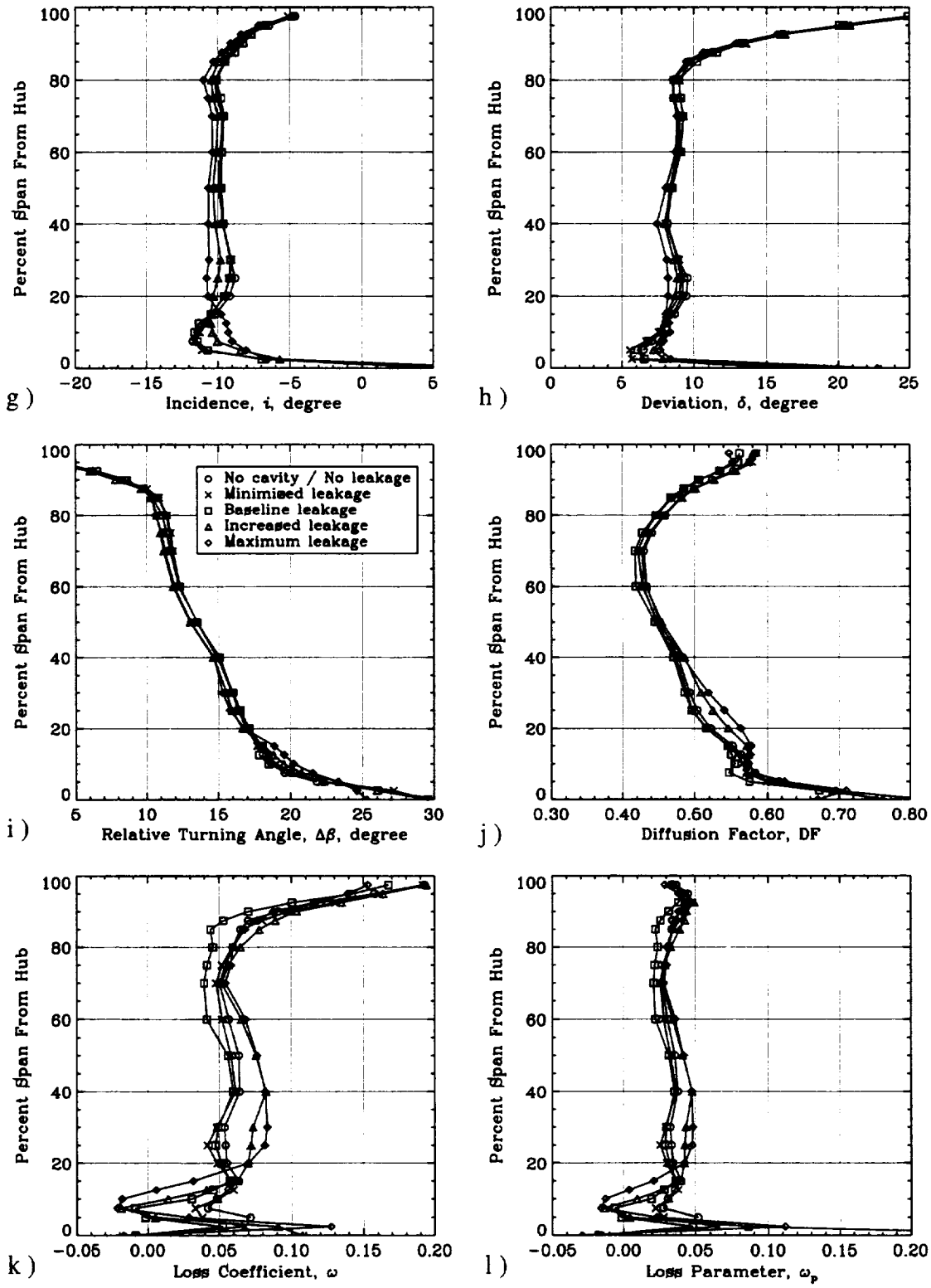

Figure VI.15 (continued) g) incidence, h) deviation, i) relative turning angle, j) diffusion factor, k) loss coefficient and l) loss parameter.

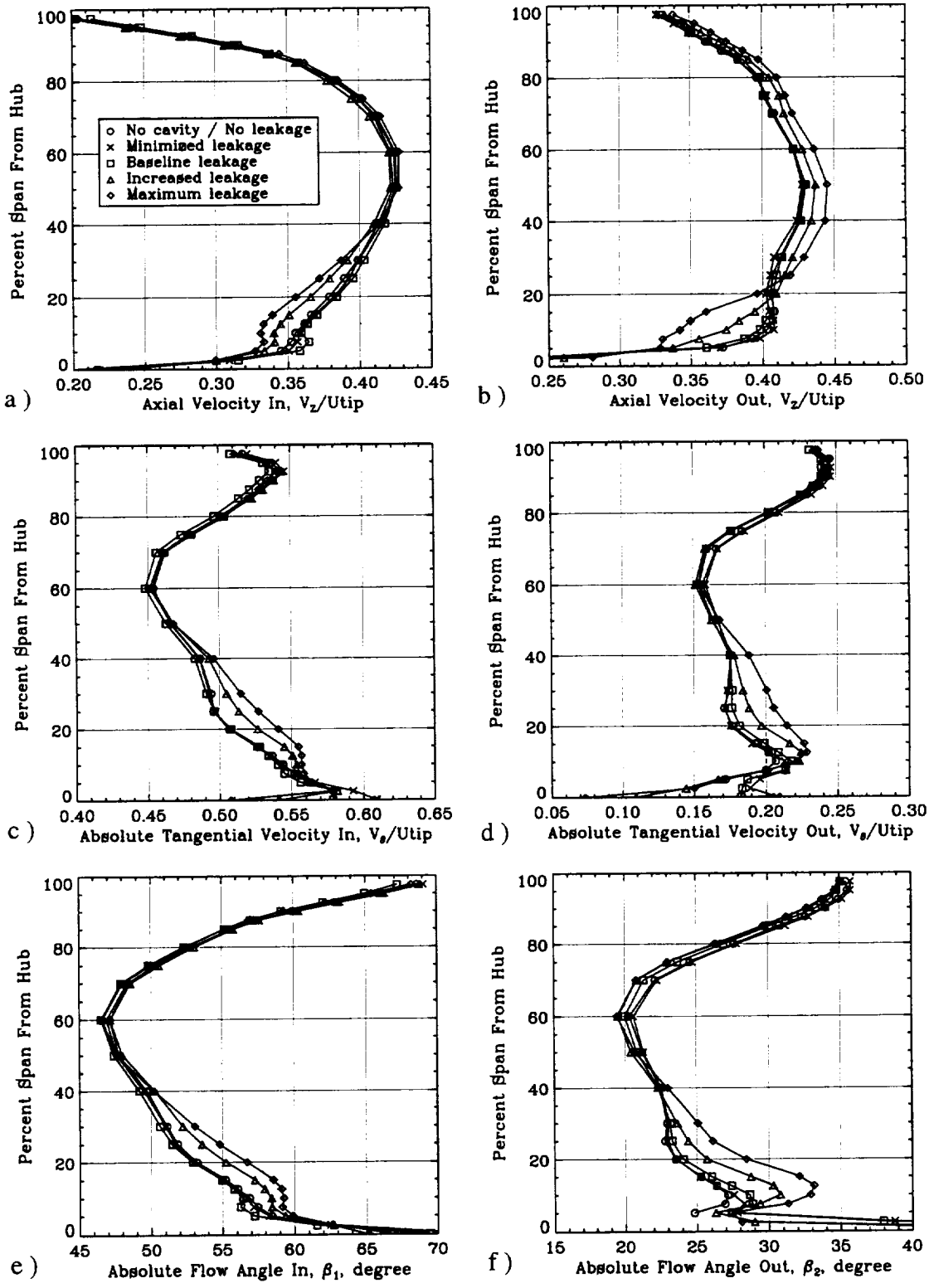

Figure VI.16 Stator 3 blade element performance near peak efficiency operating condition: a) and b) axial velocity, c) and d) absolute tangential velocity, e) and f) absolute flow angle.

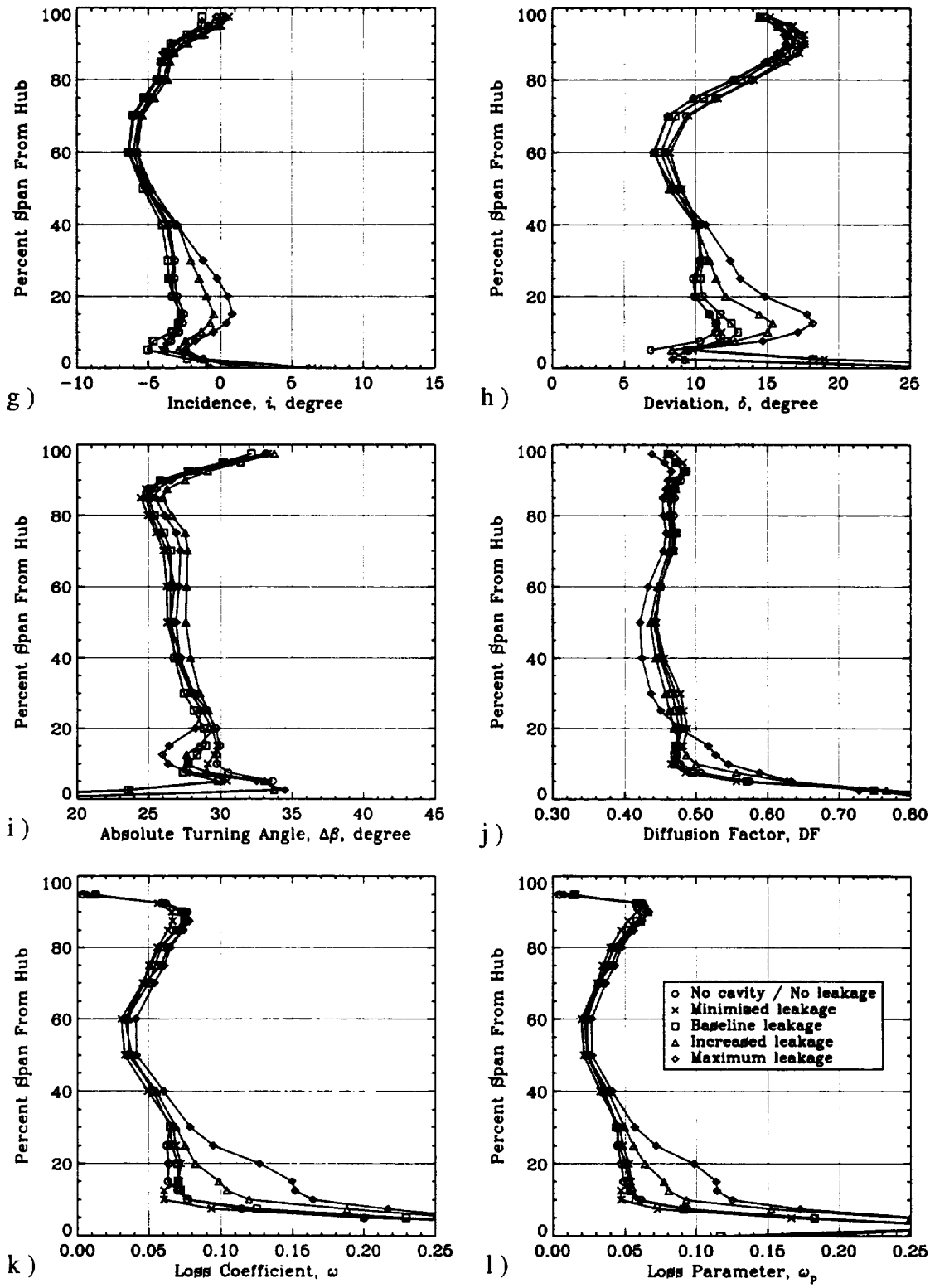

Figure VI.16 (continued) g) incidence, h) deviation, i) absolute turning angle, j) diffusion factor, k) loss coefficient and l) loss parameter.

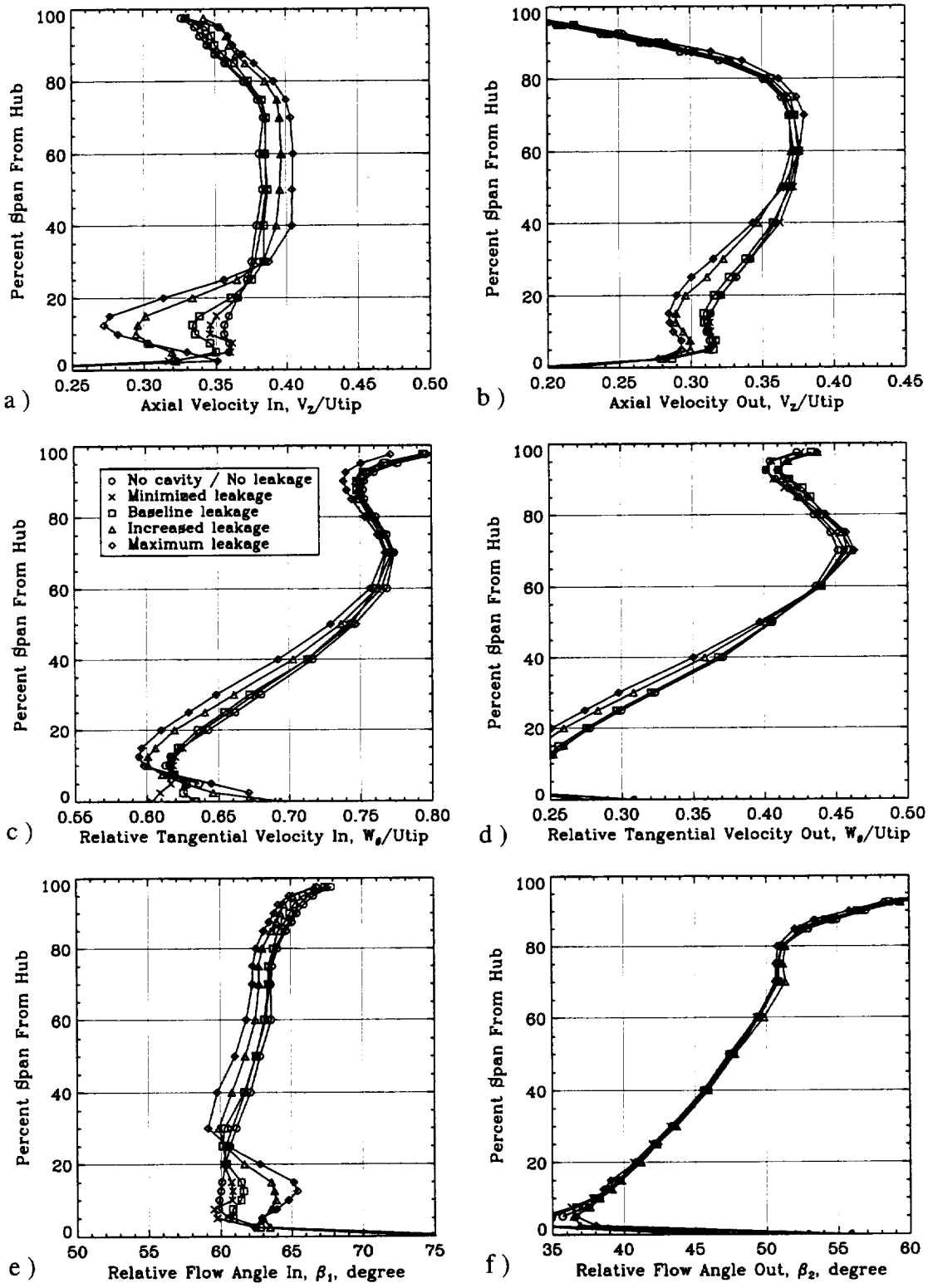

Figure VI.17 Rotor 3 blade element performance at increased loading operating condition: a) and b) axial velocity, c) and d) relative tangential velocity, e) and f) relative flow angle.

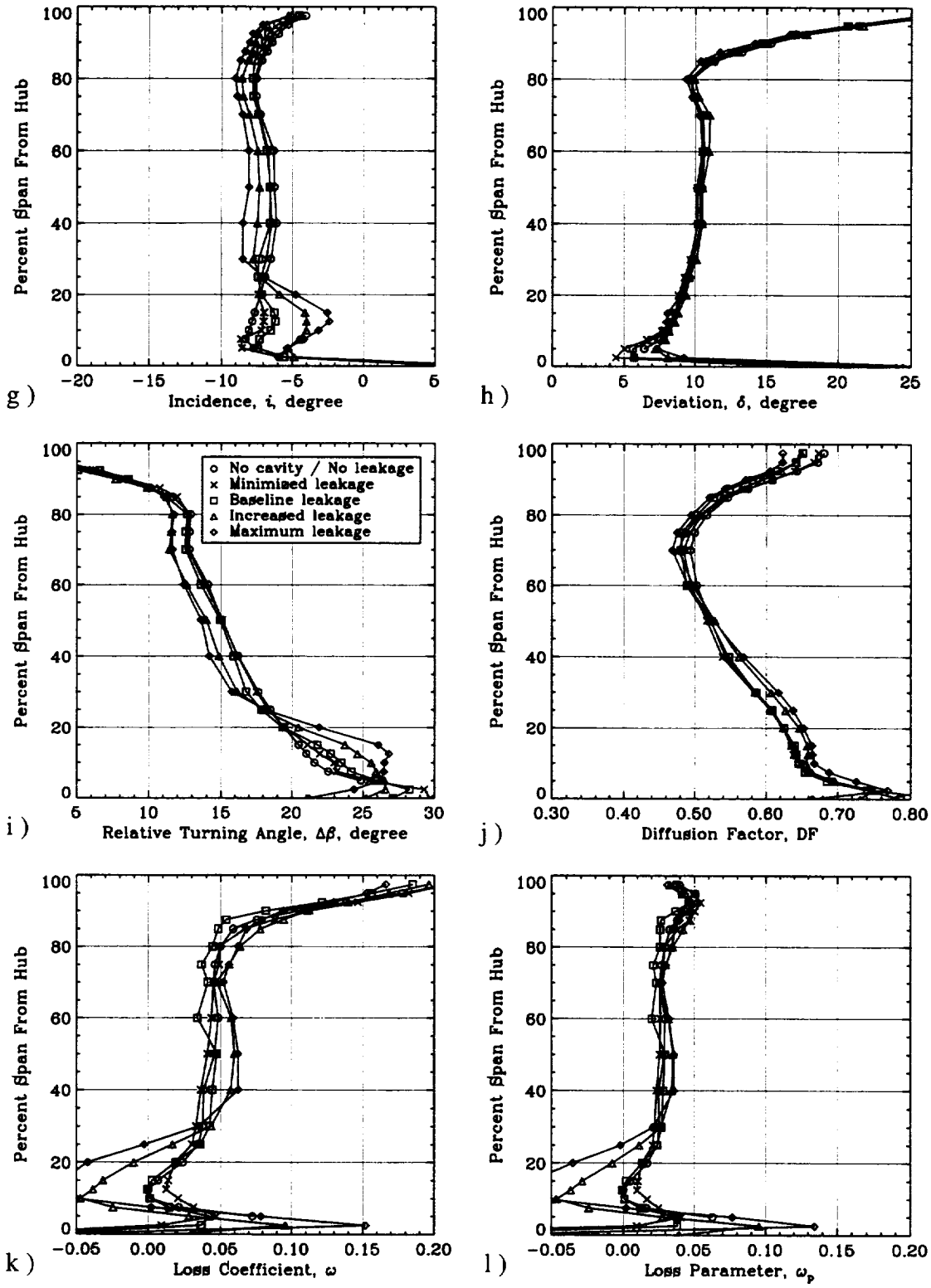

Figure VI.17 (continued) g) incidence, h) deviation, i) relative turning angle, j) diffusion factor, k) loss coefficient and l) loss parameter.

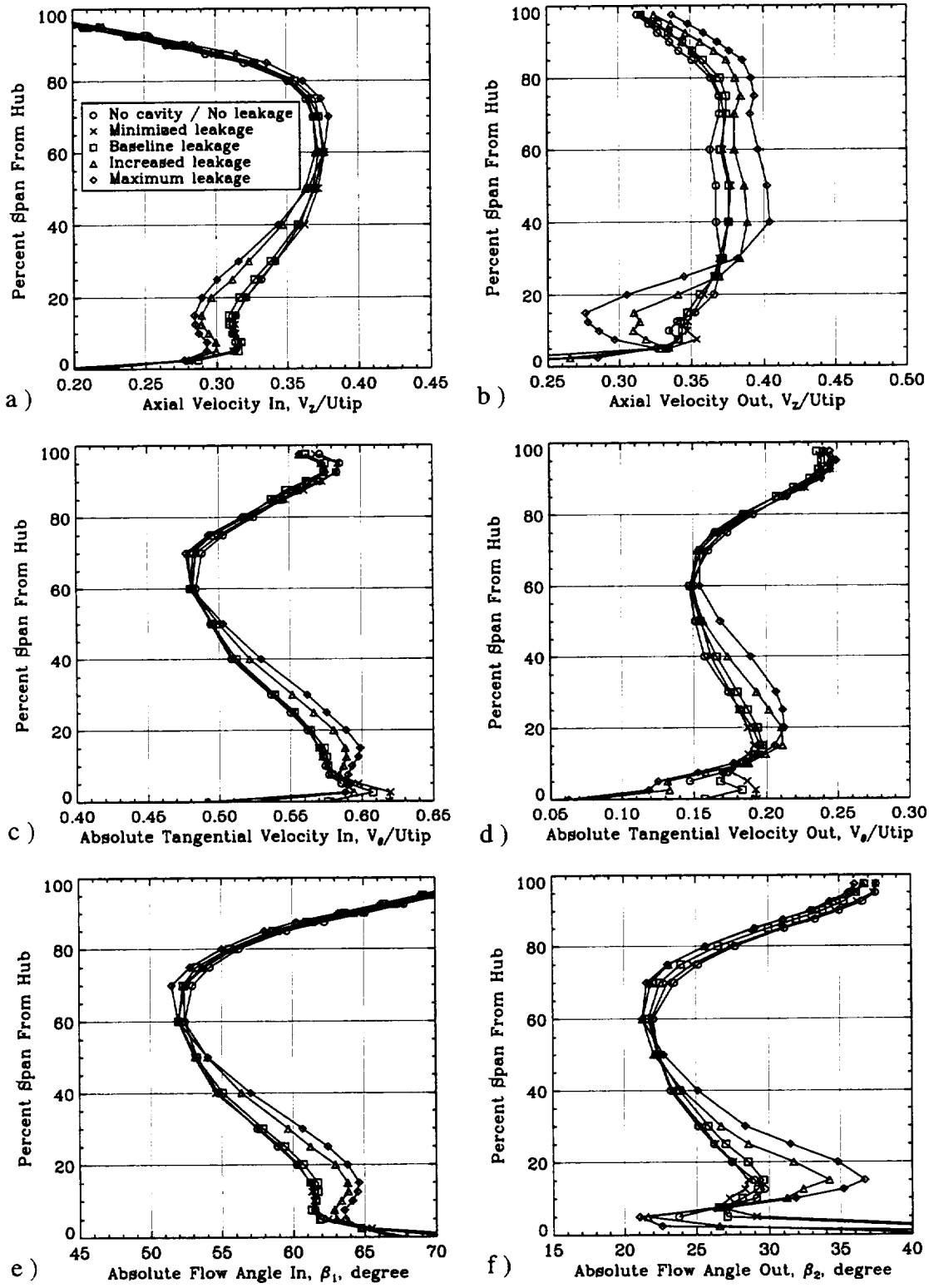

Figure VI.18 Stator 3 blade element performance at increased loading operating condition: a) and b) axial velocity, c) and d) absolute tangential velocity, e) and f) absolute flow angle.

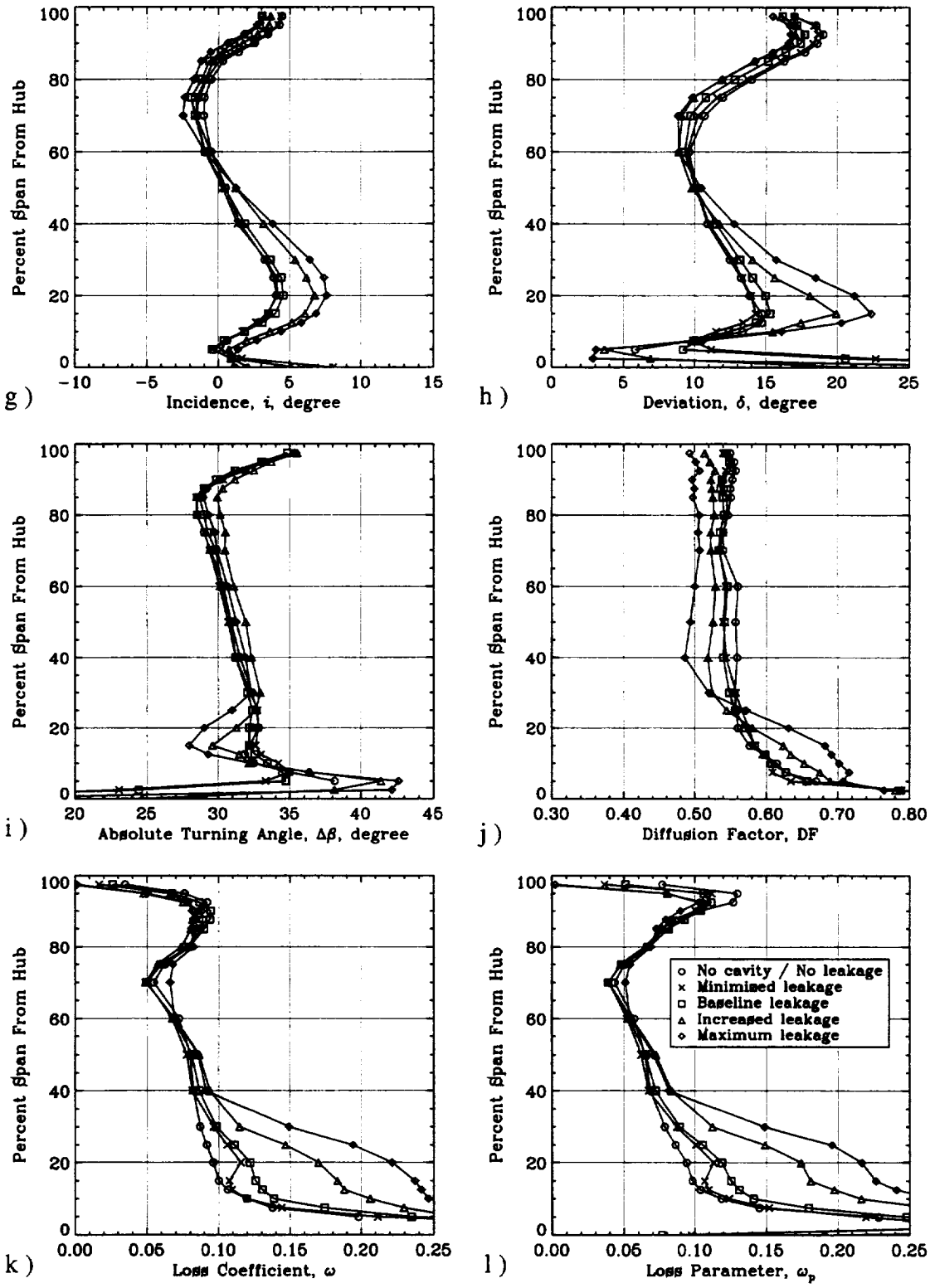

Figure VI.18 (continued) g) incidence, h) deviation, i) absolute turning angle, j) diffusion factor, k) loss coefficient and l) loss parameter.

and mixing of the large inlet total pressure deficit as it passed through the rotor. This is supported by the axial velocity data and the increased levels of loss near mid-span where rotor incidence values were actually reduced. Two dimensional thinking does not always work for three-dimensional flows.

The third stator accepted the velocity distributions from the rotor discharge. These distributions were shown to have decreased levels of axial velocity over the lower 50% of span and slightly raised levels for the rest of the span when leakage was increased. The absolute tangential velocity into the third stator was increased over the lower half of the span. This corresponded with the decrease in rotor discharge relative tangential velocity. Both of these trends, decreased axial velocity and increased tangential velocity, led to increased stator incidence (inlet flow angle) near the hub. Near the tip, stator incidence

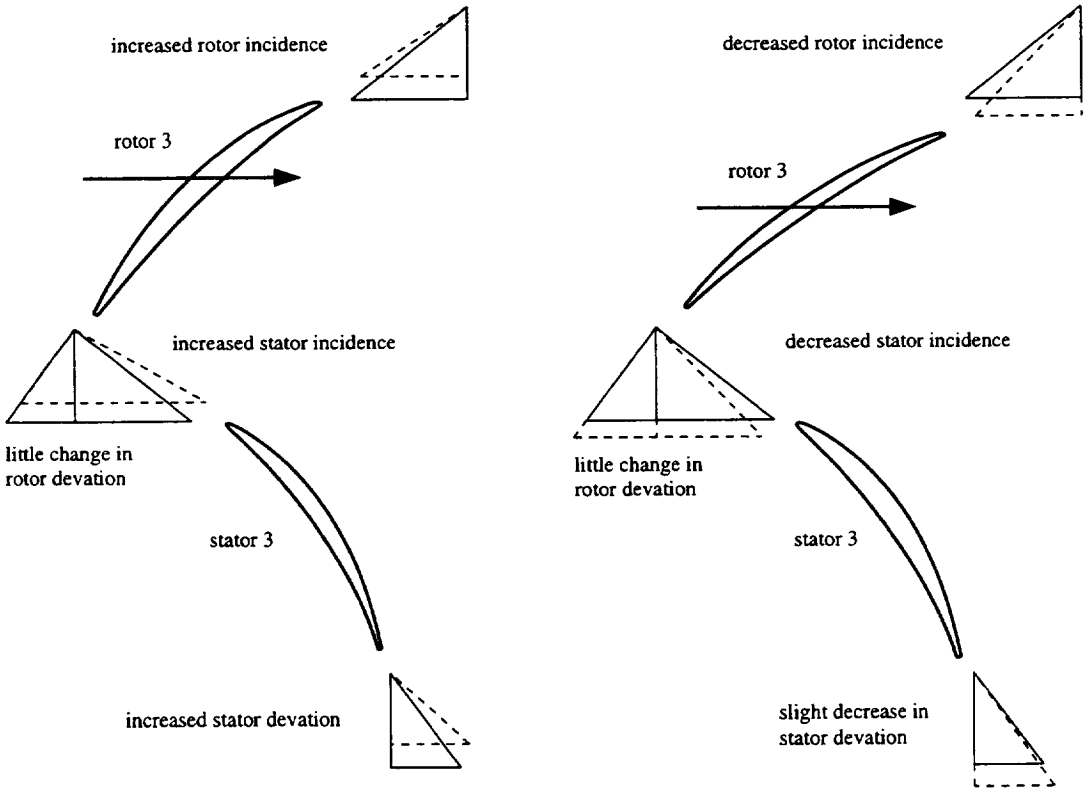

a) near the hub b) across the rest of the span

Figure VI.19 Trends in the stage velocity triangles when seal-tooth leakages were increased (solid line no cavity / no leakage, dashed line increased leakage).

angles were slightly reduced. Again, see Figure VI.19 to more clearly visualize the impact leakage had on the stator velocity triangles.

The third stator exit flow was similar to that of the second stator. More blockage developed through the passage when seal-tooth leakage was increased. Consequently, a large region of low axial velocity existed near the hub (5–25% span). The blockage near the hub forced fluid up toward the tip, which substantially increased the axial velocity there. From this experiment one can not determine whether the blockage near the hub was created by the increase in incidence and/or by the extra leakage through the seal-tooth which was entrained by the power stream ahead of the stator. More discussions on this subject are presented in Part 2. Near the hub (10-50% span) an increase in stator exit tangential velocity existed: however, at the hub (0–10%), a decrease was apparent. Considerable variations in stator deviation angles existed with varying leakage; near the case (60–95% span) deviation decreased, near the hub (10–50%span) deviation increased and at the hub (0–10%span) deviation decreased. At 15% span there existed a 7° difference in deviation between the no cavity / no leakage and maximum leakage configurations at both operating conditions. At the hub (0–10%), reduced deviation values corresponded to decreased tangential velocity levels and indicate a tendency for hub fluid to become overturned. At first, these variations in stator deviation angle with span and leakage amount appeared to correspond well to the variations in stator incidence angle with span and leakage amount. However, as with blockage development near the hub, analysis of data from this experiment alone can not determine whether the changes in stator deviation were only caused by stator incidence changes. Stator diffusion factor data show decreased loading over much of the span (25–100%), while near the hub loading increased. The reduction in diffusion across most of the span indicates that the stator produced less static pressure rise when seal-tooth leakage was increased. Marginal changes in total pressure loss occurred outboard 50% span; however, across the lower 50% of span large loss increases transpired. At 20% span, the loss nearly doubled when going from no cavity / no leakage to maximum leakage. This dramatic increase in loss can obviously be detrimental to compressor efficiency.

Circumferential Distributions Of Third Stator Flow

The radial distributions of circumferentially averaged blade element data substantially changed when the seal-tooth leakage was increased. To gain further insight into the causes of these changes, a few selected circumferential distributions of third stator flow are reviewed here. Data are presented for only the increased loading operating condition, although similar trends were seen in the near peak efficiency data. Measurements at two radial positions, 80% and 20% span, are given. Inlet and outlet axial velocity distributions are shown in Figures VI.20 and VI.21, respectively, while absolute tangential velocity data

are given in Figures VI.22 (inlet) and VI.23 (outlet). Incidence (Figure VI.24), deviation (Figure VI.25) and total pressure loss (Figure VI.26) variations are also displayed.

At the inlet of the third stator, measurements suggest the variations in circumferentially averaged blade element performance values with change in leakage were caused by constant incremental shifts in flow property levels across the entire passage. Moderate shifts in axial and tangential velocities were present at 20% span, while only small shifts transpired at 80% span. Since the velocity distributions were not altered, the pitchwise distributions of incidence for each leakage amount remained similar but had shifted levels. The sinusoidal distributions of inlet axial velocity, inlet tangential velocity and incidence seen at both radial locations were common at all spans. These distributions were primarily caused by the potential interaction of the downstream stator blade on the upstream flow field. This interaction directly varied the flow angle and static pressure distributions

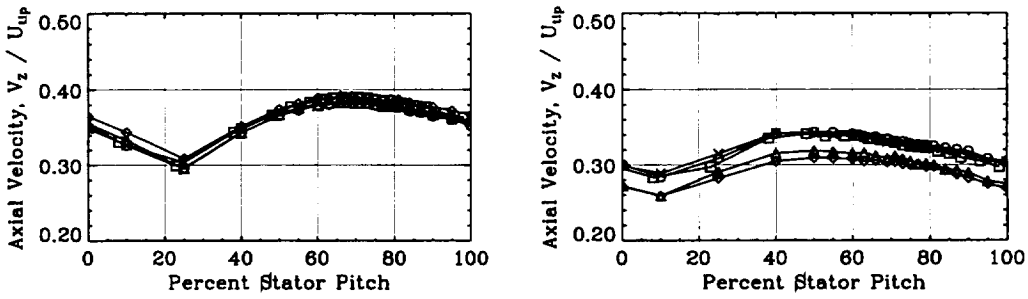

a) 80% span from hub b) 20% span from hub

Figure VI.20 Circumferential variations of inlet axial velocity for stator 3 at increased loading.

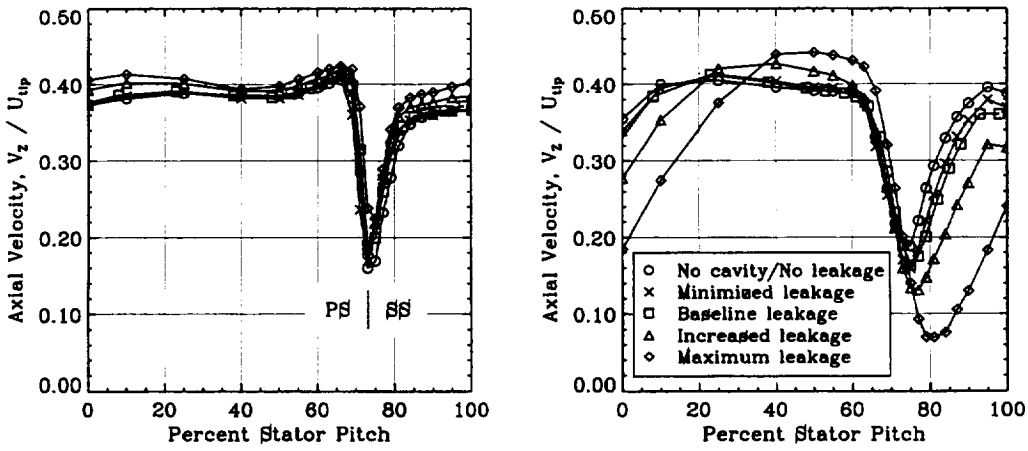

a) 80% span from hub b) 20% span from hub

Figure VI.21 Circumferential variations of outlet axial velocity for stator 3 at increased loading.

across the passage in front of the stator. A secondary cause of the observed sinusoidal distributions was the fixed "avenue" chopped segments of the upstream stator wake. Although traveling more than a chord length before reaching the third stator inlet, the upstream second stator wake segments were not fully mixed out and, hence, contributed to the small pitchwise variation in total pressure at the entrance of the third stator.

Contrary to data for flow into the stator, data for flow exiting the stator demonstrated sizable changes in the pitchwise distributions of flow properties with leakage. This was especially true near the hub. Stator exit axial velocity data show that at 20% span the large region of blockage depicted in Figures VI.16 and VI.18 developed near the suction side of the blade wake. Pressure and suction sides of the wake are denote by PS and SS, respectively with the split determined by the location of the minimum axial velocity. Comparisons of the no cavity / no leakage data to that of the maximum

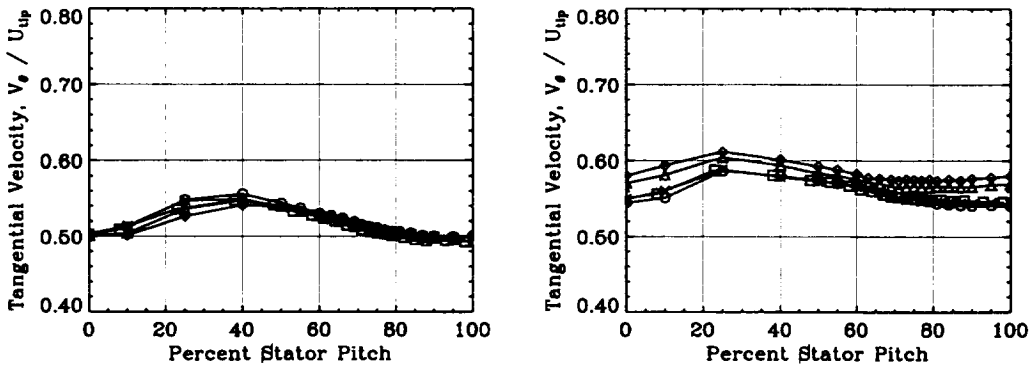

a) 80% span from hub b) 20% span from hub

Figure VI.22 Circumferential variations of inlet absolute tangential velocity for stator 3 at increased loading.

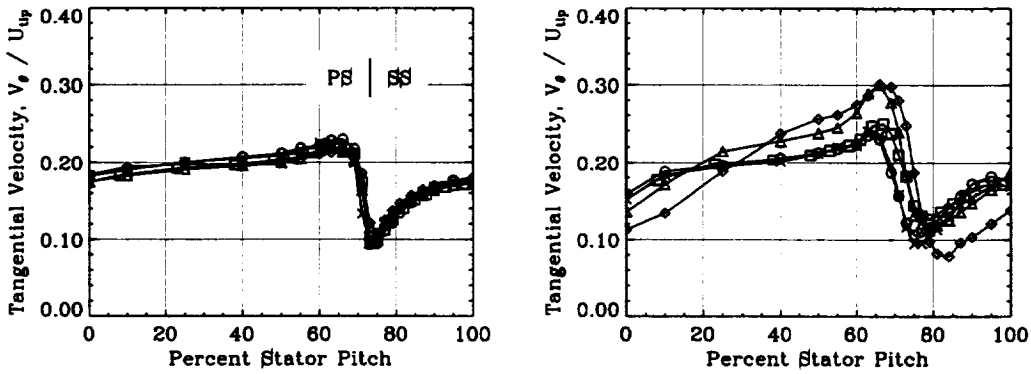

a) 80% span from hub b) 20% span from hub

Figure VI.23 Circumferential variations of outlet absolute tangential velocity for stator 3 at increased loading.

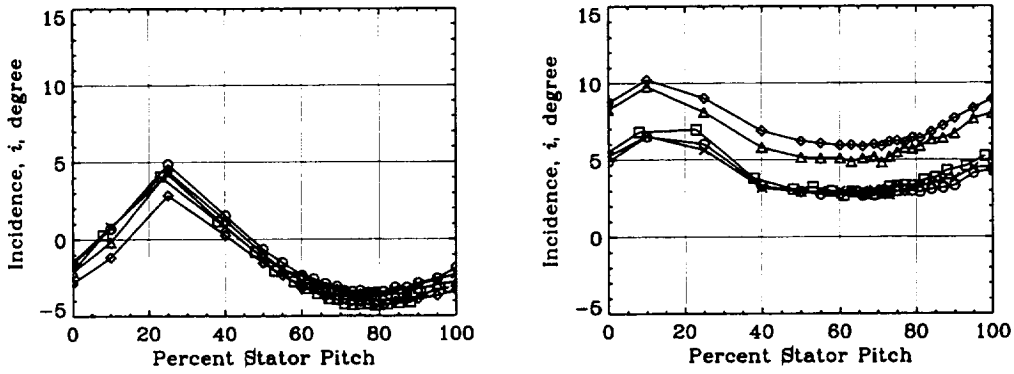

a) 80% span from hub b) 20% span from hub

Figure VI.24 Circumferential distributions of stator 3 incidence at increased loading.

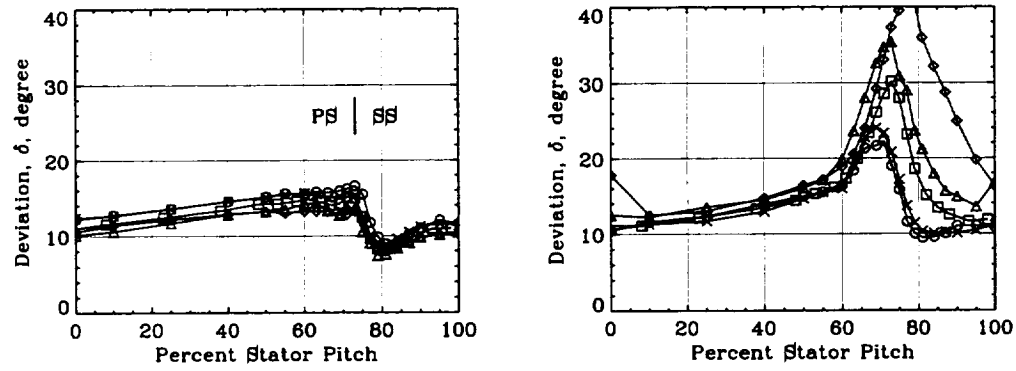

a) 80% span from hub b) 20% span from hub

Figure VI.25 Circumferential distributions of stator 3 deviation at increased loading.

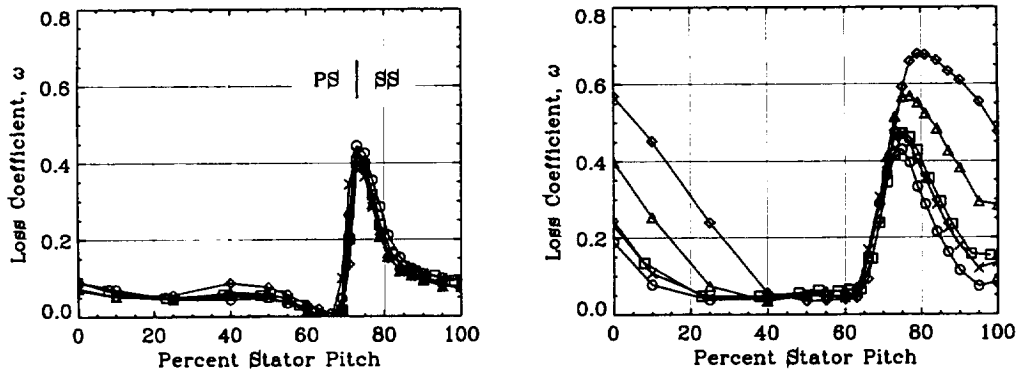

a) 80% span from hub b) 20% span from hub

Figure VI.26 Circumferential distributions of stator 3 loss at increased loading.

leakage configuration indicate the stator wake width increased from 40% to 80% pitch while the wake depth grew from 50% to nearly 90% of the free stream value. Large variations in the pitchwise distributions of tangential velocity also existed near the hub (20% span). It appears that the suction side tangential velocity decreased with increased seal-tooth leakage while the pressure side tangential velocity actually increased. Only small changes to the wake width and depth occurred at 80% span and virtually no change to the levels or distributions of tangential velocity were detected there.

Pitchwise distributions of deviation and loss data at 80% span show nearly no change with leakage. At 20% span, though, large variations in deviation and loss with leakage change were present across most of the passage. A definite trend existed in which the suction side deviation and loss values increased with increased seal-tooth leakage. The deviation value became greater than 40° at 80% pitch for the maximum leakage case. The loss in total pressure at the same location and for the same configuration reached nearly 0.7. Both of these values, along with the significant decrease in axial velocity, suggest that the suction surface boundary layer was severely disrupted when seal-tooth leakage was increased. It is interesting to note that even though the suction side deviation severely worsened, the flow deviation between blade wakes (10% to 60% pitch) were not significantly altered.

CHAPTER VII

RESULTS AND ANALYSIS OF DATA: PART 2

The results of Chapter VI revealed that significant variations in overall, individual stage and blade element performance occurred when shrouded stator seal-tooth leakage was changed. However, since the leakage amounts of all four stages were altered uniformly and simultaneously, the inlet flow profiles of the last three stages varied greatly with each change. These conditions made it difficult to identify the influence of seal-tooth leakage alone on the performance of each individual stage. A second experiment was therefore performed in order to specifically determine the influence of seal-tooth leakage on the performance of an embedded stage. For this experiment individual stage and blade element data were collected when only the third stage leakage was modified. Stages one, two and four were kept at the baseline leakage configuration. The seal-tooth clearance values implemented on the third stage for this series of tests are described in Chapter V. This chapter summarizes the results of this second experiment with frequent reference to data presented in Chapter VI.

Individual Stage Performances

Changes to the third stage shrouded stator cavity geometry moderately altered the third and fourth stage pressure rise characteristics. No measurable differences were detected in the first and second stage pressure rise values. This is shown in Figure VII.1. No change in first and second stage characteristics were expected since the redistributions of the flow field in the third stage were not considered large enough to influence the upstream stages. The performance degradation of the third and fourth stages was also expected. The reduction of third stage pressure rise was directly influenced by the amount of seal-tooth leakage of that stage. Since the fourth stage seal-tooth clearance was the same for all configurations in this experiment, the fourth stage pressure rise decrease was caused by the different inlet conditions into the fourth rotor.

Reductions in the normalized third stage pressure rise values at two operating conditions are shown in Figure VII.2 for third stator seal-tooth clearance values. Third stage data already presented in Figures VI.9 and VI.10 of Part 1, are also displayed in Figure VII.2 and represented by filled symbols. For both experiments, the no cavity / no leakage data were considered the zero clearance references. Data for variation of the third stator clearance only show a 2.0% to 2.5% reduction in the stage pressure rise at both operating conditions when going from no cavity / no leakage to maximum leakage. The pressure decrease was represented well by a linear approximation. Comparisons of the Part 1 and Part 2 data suggest that nearly 40% of the third stage pressure decrease

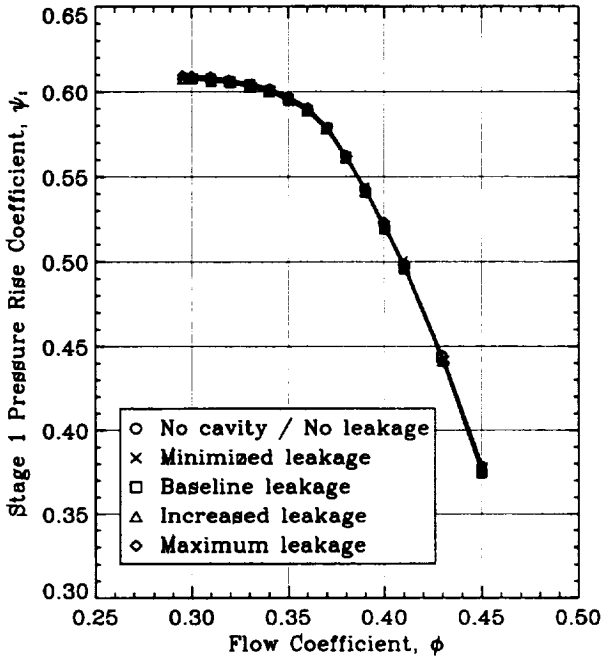

a) Stage 1 characteristics

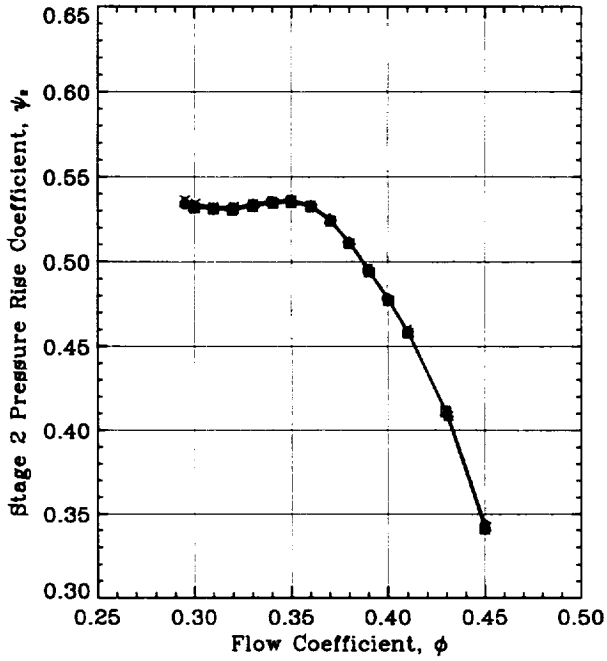

b) Stage 2 characteristics

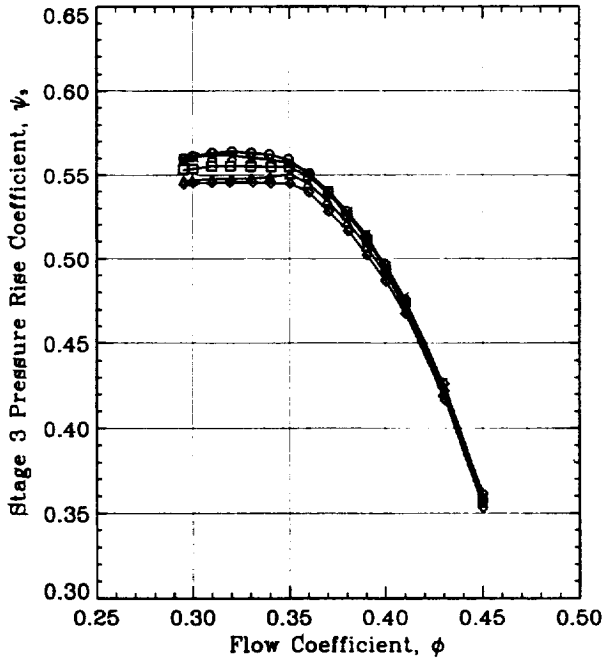

c) Stage 3 characteristics

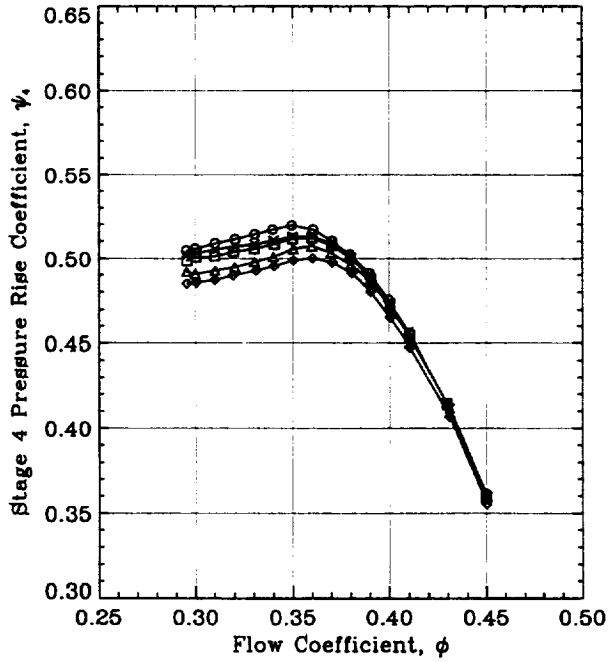

d) Stage 4 characteristics

Figure VII.1 Stage pressure rise characteristics for the five test configurations.

observed in Part 1 could be directly attributed to the change in the third stator seal-tooth leakage alone.

The variations in the fourth stage pressure rise values depicted in Figure VII.1d indicate that alterations to the fourth rotor inlet flow field associated with third stator seal clearance changes only were responsible for a large portion of the stage pressure rise decreases present in the data of Part 1 (Figure VI.8d). At increased loading operation ($\phi = 0.350$) the decrease in forth stage pressure rise was approximately 0.025 compared to 0.050 for Part 1 (Figure VI.8d). Therefore, nearly half of the forth stage pressure rise degradation in Part 1 can be attributed to the variations in the incoming flow to rotor 4. This fact coupled with the conclusions drawn from stage 3 data indicate that the presence of seal-tooth leakage affects stage performance in two distinct ways. First, a stage performance penalty will be suffered because of the amount of leakage associated with that stage. Second, performance of downstream stages can be degraded by any upstream stator flow field disruptions due to increased seal-tooth leakage of that upstream stator.

On a final note, some care should be taken when reviewing the stage performance data of Part 2, since the values of the pressure rise coefficient quoted contain a small error which was not accounted for during the data reduction process. The error arose because a repeating stage environment was assumed when calculating the isentropic enthalpy

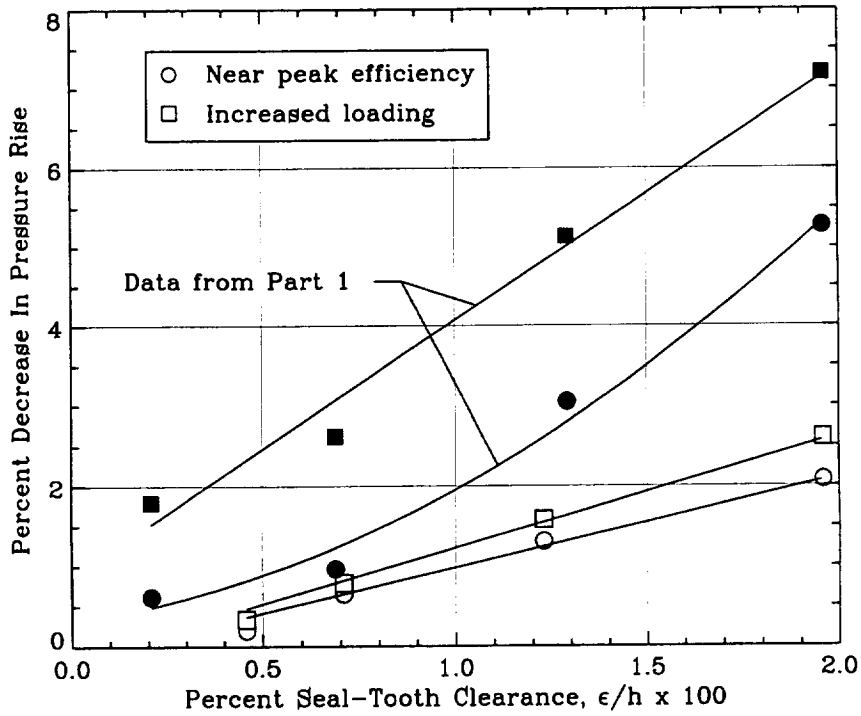

Figure VII.2 Third stage pressure rise penalties for near peak efficiency and increased loading operating conditions.

rise values from the casing static pressures. The assumption of a repeating stage was surely incorrect since modifications were made to only the third stage geometry, creating different stage outlet flow conditions compared to the inlet conditions for the last two stages. Quick estimates of this error were found to be less that 0.2% of the maximum pressure rise coefficient (about the size of the symbols in Figure VII.2): however, complete spanwise inter-stage measurements were not gathered preventing a thorough analysis to be completed. Therefore, the reader is simply cautioned when examining Part 2 individual stage performance data.

Circumferentially Averaged Third Stage Flow Details

Blade element data were again gathered for the different seal-tooth leakage rates in order to quantify the changes in radial distributions of circumferentially averaged flow properties. For this experiment, pneumatic probe traverses of the third stage were performed over the lower 50% of span (only 30% of the span was traversed for the baseline case). Unfortunately, fourth rotor discharge measurements were not gathered. Data were acquired in a matrix of 19 radial locations and 26 circumferential positions at two operating conditions for most leakage rates. Measurements were also appropriately clustered near large gradients in the flow properties.

Data collected for Part 2 indicated no measurable differences in the third rotor blade element performance values for the various leakage rates except for a small region at the hub (0–3% span). Since the first and second stages performed overall the same for all cases (shown in Figures VII.1a and VII.1b), the flow into the third rotor was identical for each leakage rate, although obvious differences in the data existed when comparing dissimilar operating points. The measured third rotor inlet flow distributions corresponded to the baseline values denoted by squares in Figures VI.15a,c,e,g and VI.17a,c,e,g from Part 1. The flow out of the third rotor was nearly identical for each leakage. The only difference detected in the data between the various configurations was a slight increase in the relative tangential velocity at the hub (0–3% span) when seal-tooth leakage increased. The third rotor exit flow data of Part 2 closely followed the baseline distributions already presented in Figures VI.15b,d,f,h and VI.17b,d,f,h (Part 1) and are not presented here.

Radial distributions of stator three blade element performance are given in Figure VII.3 for the near peak efficiency operating condition. Data corresponding to the increased loading operating condition are present in Figure VII.4. For increased loading all performance parameters which utilized the exit wedge probe measurements for the no cavity / no leakage configuration were discarded, since probe damage occurred prior to conducting the survey. As with Part 1, stated trends are correlated with increasing seal-tooth leakage.

As previously stated, the various leakage rates had little impact rotor 3 performance. Furthermore, rotor 3 discharge flow conditions were nearly identical for all five leakage rates when at the same operating condition. This is supported by the stator inlet flow data shown in Figures VII.3a,c,e,g and VII.4a,c,e,g. The small shifts in the levels of axial velocity, tangential velocity, absolute inlet flow angle and incidence for the peak efficiency condition are not much more than the measurement accuracy at that station. A reduction in whirl with increased seal-tooth leakage from 0–3% span was present at both operating conditions. This corresponds with the increased relative tangential velocity mentioned earlier. This reduction in tangential velocity reduced the incidence onto the stator by about 4° at 1% span at both operating conditions.

As in Part 1, Part 2 data show substantial alterations in the radial distributions of flow properties at the exit of stator 3. Likewise, the trends established in Part 1 when the seal-tooth leakage was increased were repeated in Part 2, but to a lesser extent. This is confirmed by comparing Figures VII.3b,d,f,h-l and VII.4b,d,f,h-l to Figures VI.16b,d,f,h-l and VI.18b,d,f,h-l, respectively. Increasing the third stage seal-tooth leakage lowered the axial velocity near the hub (0–20% span) while outboard of 30% span the axial velocity was raised. The absolute tangential velocity was reduced near the hub (0–8% span) but increased away from the endwall (10–50% span). Deviation angles increased except very near the hub. An increase of 5° occurred near 12.5% span for both operating conditions. Since the stator deviation grew, but incidence angles were unchanged, the absolute turning decreased over most of the span. Diffusion factor distributions show increased loading near the hub (0–15% span) and a reduction in loading outboard of 20% span. Finally, total pressure loss near the stator hub increased greatly. The region in which the loss increased extended out to 25% span near peak efficiency and 35% span for the increased loading operating condition. At 12.5% span, the loss increase for the maximum leakage configuration was nearly double the value associated with the no cavity / no leakage configuration.

The extent to which seal-tooth leakage directly affects the stator blade flow field can be inferred from the comparisons of Part 1 and Part 2 circumferentially averaged data. This, however, does not readily lead to a useful analysis. To make a more quantitative comparison, two additional parameters have been calculated. The first, defined by Equation VII.1, is an axial velocity displacement thickness. This can be taken as a type of one-dimensional axial velocity blockage factor, similar but not exact to what might be used in a throughflow calculation. This term is used to represent the "extra" hub blockage which developed in a stator passage due to the entrainment of leakage flow. The second parameter, given in Equation VII.2, is simply the mass averaged total

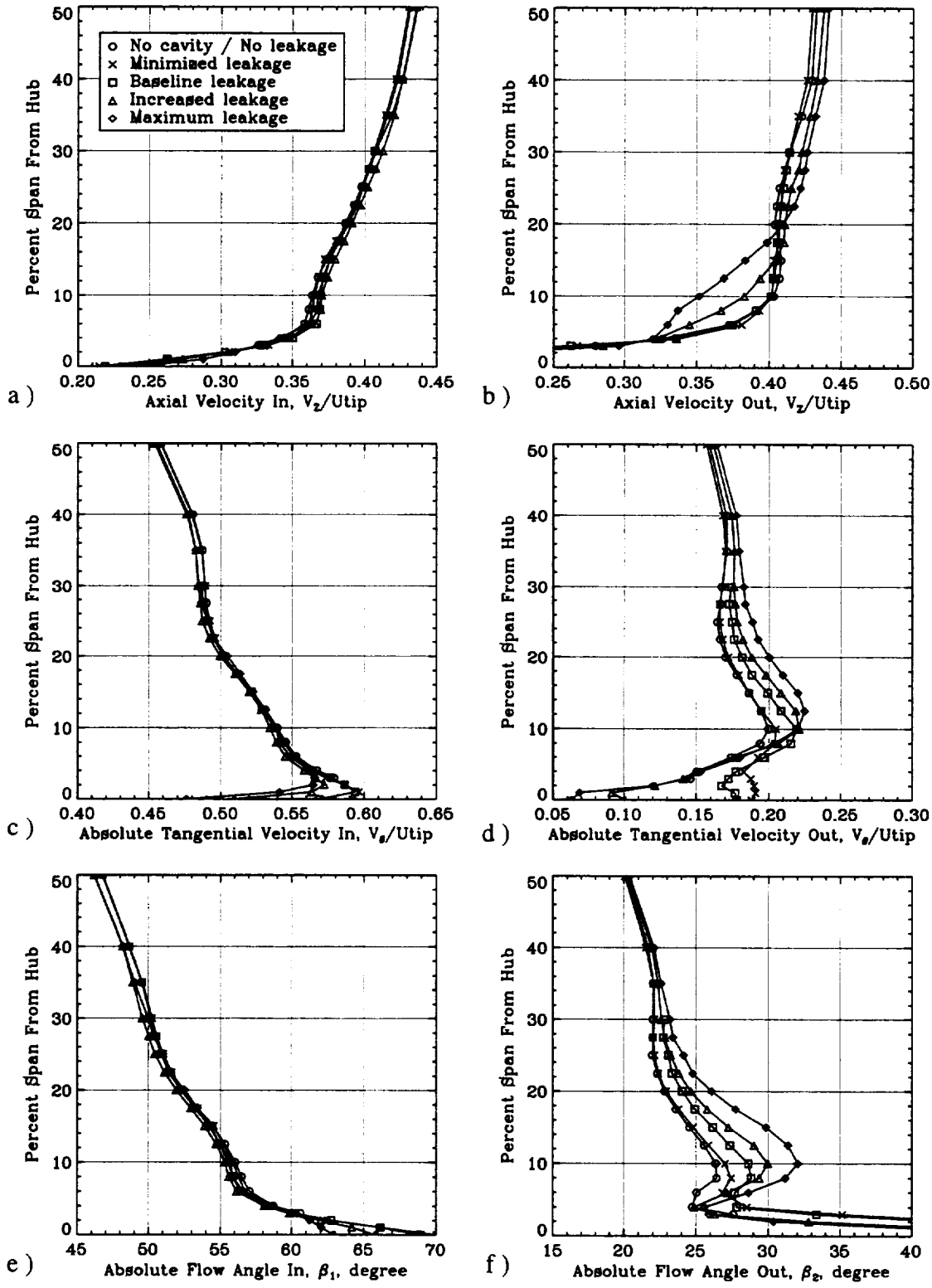

Figure VII.3 Stator 3 blade element performance near peak efficiency operating condition: a) and b) axial velocity, c) and d) absolute tangential velocity, e) and f) absolute flow angle.

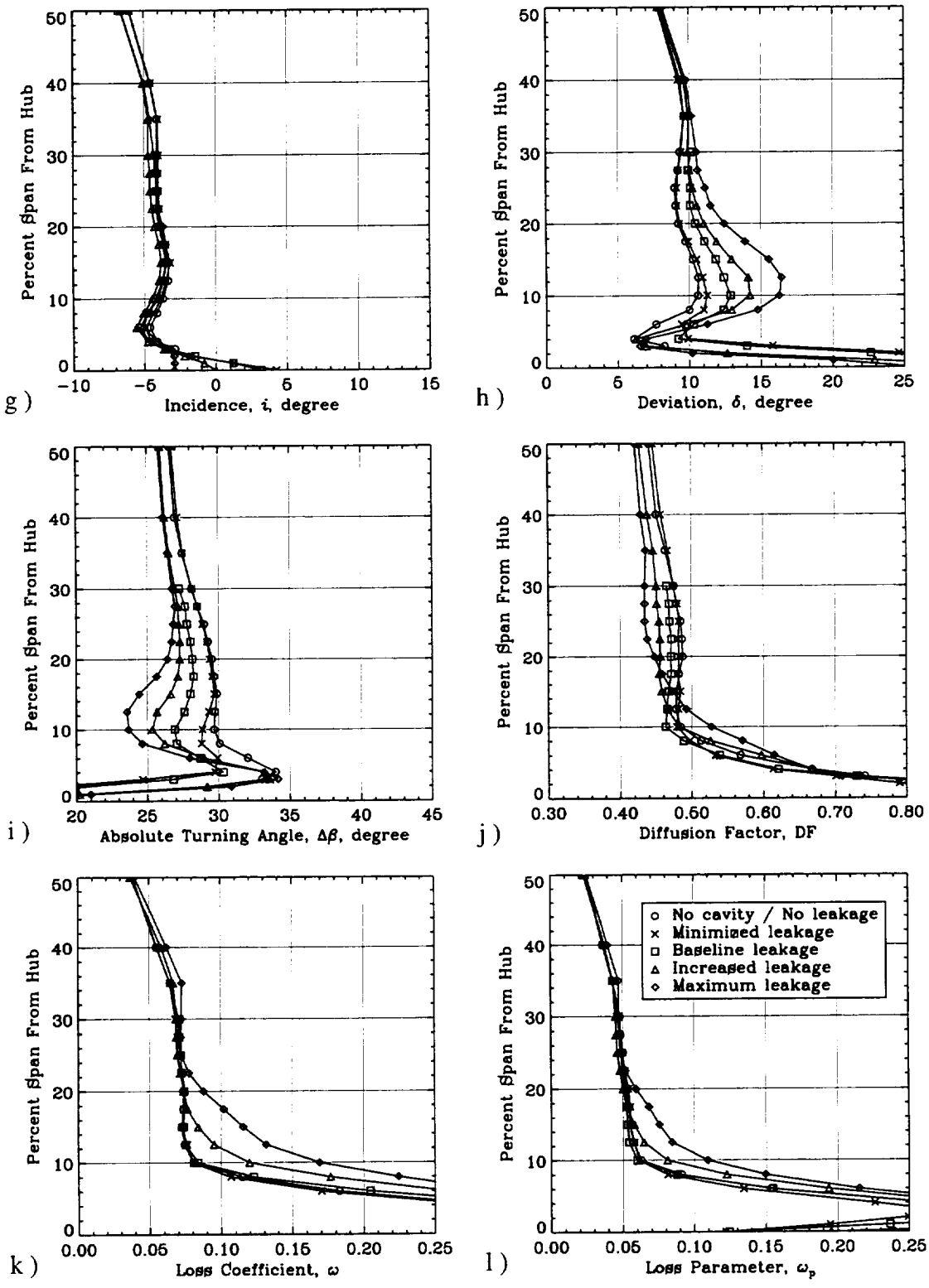

Figure VII.3 (continued) g) incidence, h) deviation, i) absolute turning angle, j) diffusion factor, k) loss coefficient and l) loss parameter.

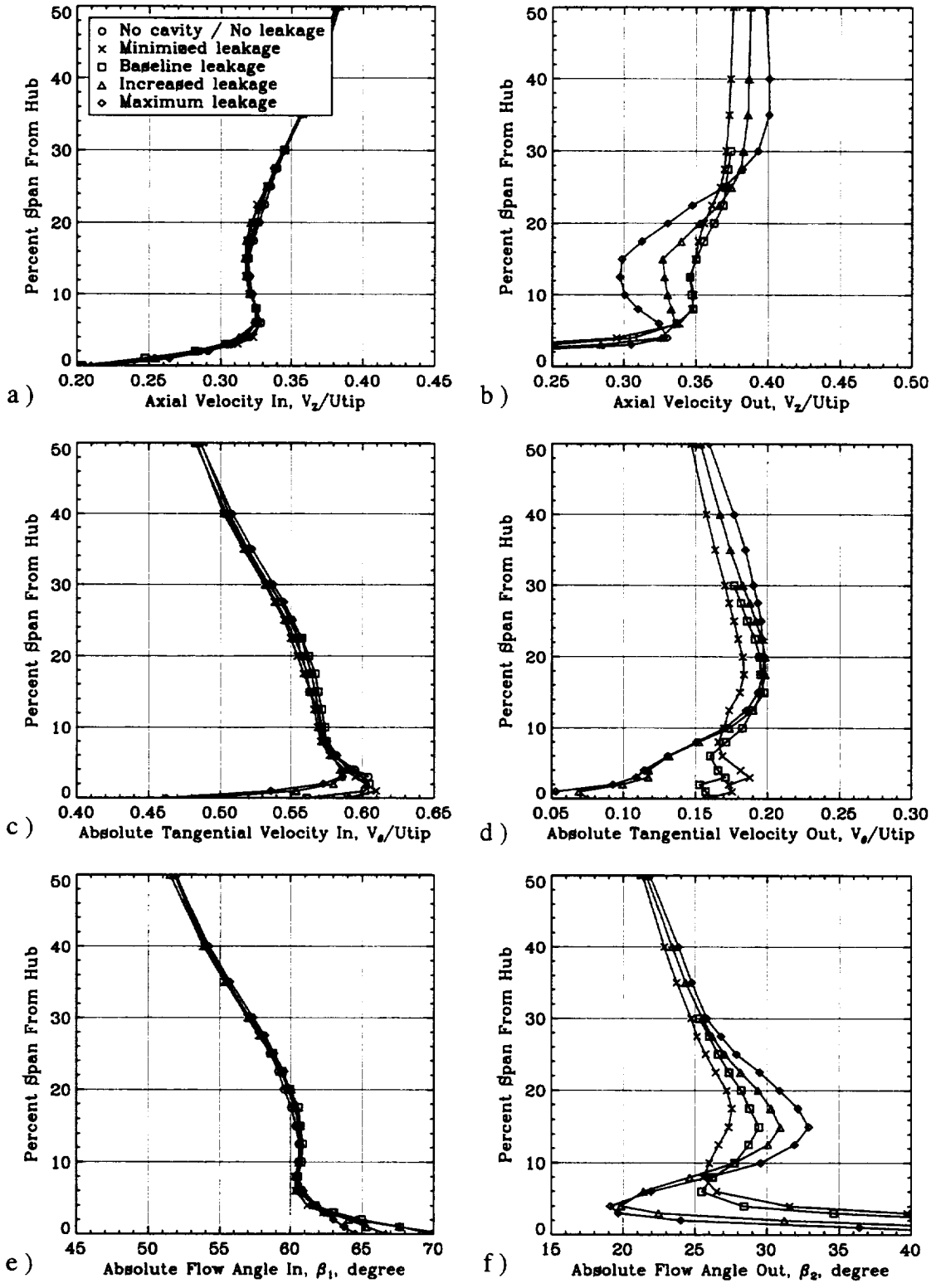

Figure VII.4 Stator 3 blade element performance at increased loading operating condition: a) and b) axial velocity, c) and d) absolute tangential velocity, e) and f) absolute flow angle.

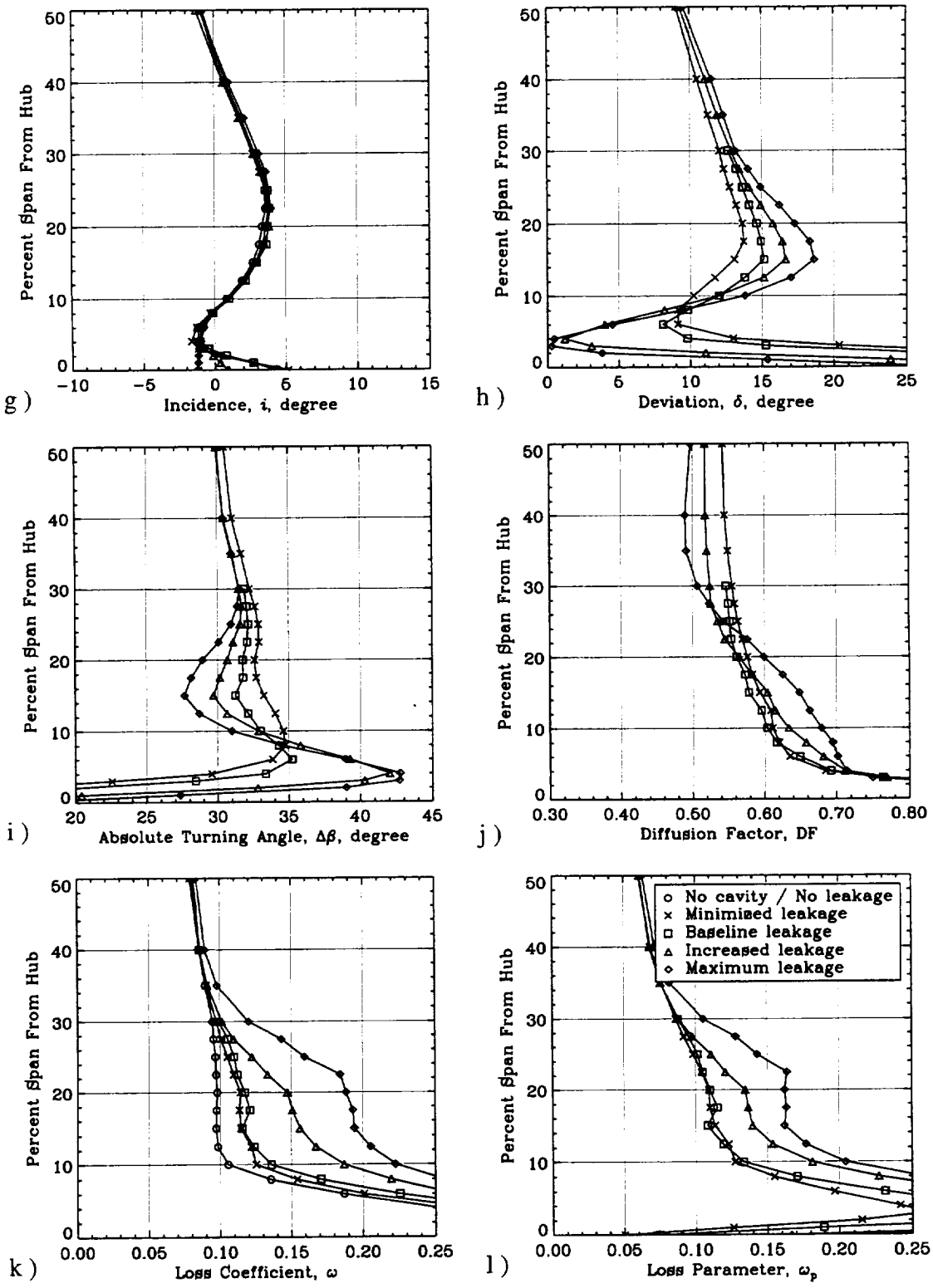

Figure VII.4 (continued) g) incidence, h) deviation, i) absolute turning angle, j) diffusion factor, k) loss coefficient and l) loss parameter.

pressure loss across a spanwise portion of the passage.

$$\delta^* = \frac{1}{r_h} \int_{r_1}^{r_2} \left(1 - \frac{V_z}{V_{z,ref}}\right) r \, dr \tag{VII.1}$$

$$\overline{\omega} = \frac{\int_{r_1}^{r_2} \omega \, V_z r \, dr}{\int_{r_1}^{r_2} V_z r \, dr} \tag{VII.2}$$

The calculation of both these parameters required some care. Integrations were performed by trapezoidal summations across 35% of the span (5% to 40%). Integration to the hub (0% span) was not performed since the measurement uncertainty rose below 5% span. Integration was stopped at 40% span since flow properties were nearly identical outboard of 40% for the various configurations. The values of axial velocity, V_z, were taken from the circumferentially averaged values already presented. The reference axial velocity, $V_{z,ref}$, was taken to be the value at 40% span. Note that this creates a different displacement thickness than defined by Smith [21], but still yields appropriate trends. As with axial velocities, total pressure loss values, ω, were also taken from the radial distributions. Therefore, the averaged loss term does not account for any extra loss in total pressure caused by the further mixing of circumferential or radial non-uniformities. Finally, when calculating both parameters, ideally it may have been more appropriate to integrate across a set of stream lines having constant mass flow instead of constant area. This proved to be difficult when tried in practice. The volumetric flow rate through the upper and lower integration bounds varied at most by only 5% for the range of leakage rates, which, although not perfect, was considered to be acceptable.

These parameters were calculated from both Part 1 and Part 2 data at near peak efficiency and increased loading operating conditions. Displacement thickness values are illustrated in Figure VII.5, while total pressure loss quantities are given in Figure VII.6. One trend should be noted immediately when viewing both figures. The values of either displacement thickness or loss for a specific operating condition should be nearly equal for the baseline leakage rate ($\epsilon/h \approx 0.7\%$), since, for both Parts, nearly identical incoming flow distributions and seal-tooth leakage rates were present for this case. This is seen to be true. A second trend to be noticed is that, for clearances less than baseline ($\epsilon/h < 0.7\%$), Part 1 near peak efficiency displacement thickness and loss values are less than those of Part 2. This could indicate the added benefit of having a "better" flow profile coming into the stator which occurred in Part 1. This trend may also be inferred by extrapolating the increased loading data to zero clearance. Finally, for clearances greater than baseline ($\epsilon/h > 0.7\%$), Part 1 displacement thickness and

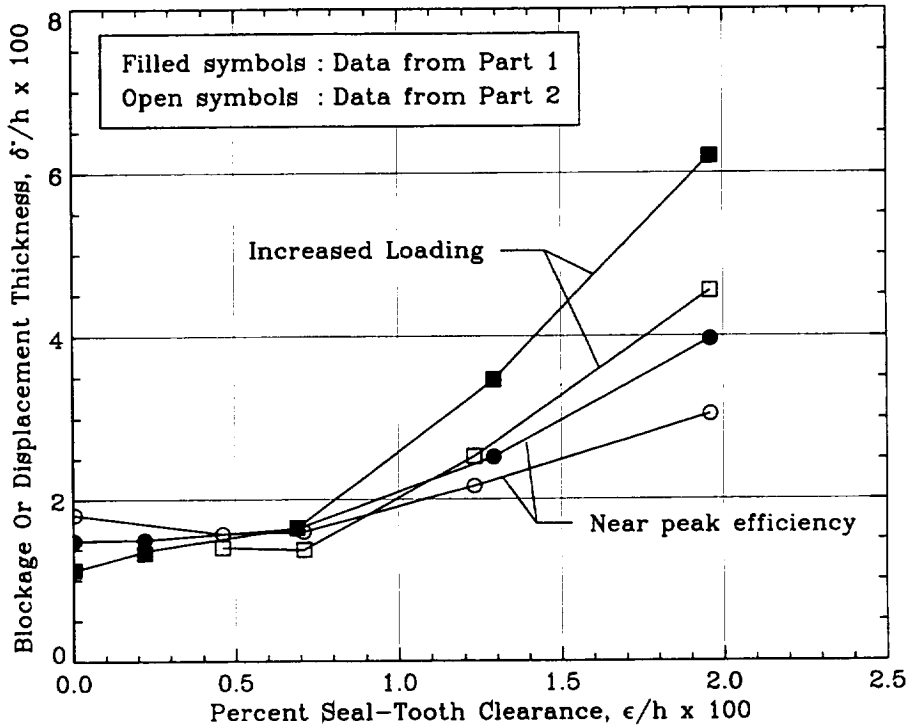

Figure VII.5 Axial velocity displacement thickness variations.

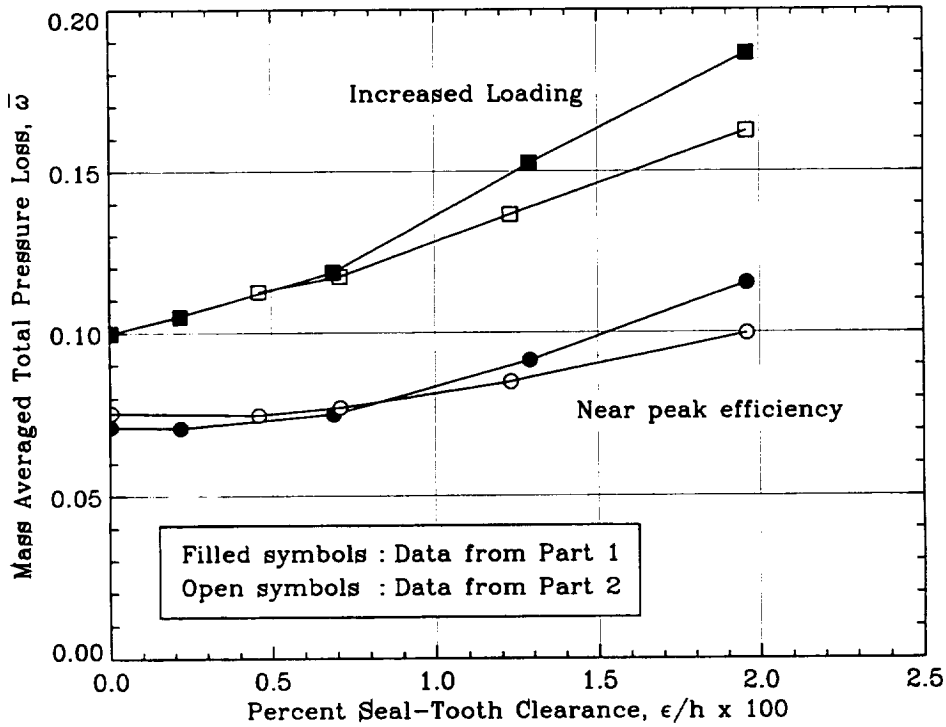

Figure VII.6 Variations in mass averaged total pressure loss.

loss values (at both operating conditions) are greater than those of Part 2. This indicates the extra detriment caused by having a "worsened" flow profile coming into the stator. For clearances larger than the baseline value, nearly 65% of the extra blockage which developed in Part 1 can be attributed solely to the increase in seal-tooth leakage under the third stator. The other 35% was caused primarily by different flow conditions into the stator. The loss increase found in Part 1 can also be broken into the two contributing factors. Increasing the seal-tooth leakage under stator three accounted for 56% of the increase in loss found in Part 1 (67% for increased loading), while 44% may be attributed to the different incoming flow distributions (33% for increased loading).

Comparisons of all the data from both Parts leads to two major conclusions. First, seal-tooth leakage affects rotor performance in a rather indirect manner. This conclusion was drawn because it was found that varying the amount of seal-tooth leakage in a stage negligibly alters the rotor performance of that stage. Instead, seal-tooth leakage disrupts the stator flow field which, in turn, produces different stator exit flow conditions. These different conditions into the downstream rotor then modify the performance of that rotor. Second, seal-tooth leakage influences the performance of a stator both directly and indirectly. Changing the amount of seal-tooth leakage in a stage can alter the stator performance for that stage. This was clearly seen in Part 2. Furthermore, provided the downstream rotor cannot "heal" the degraded incoming flow, the flow into the next stator may also be altered. This can alter the performance of that downstream stator. From these conclusions it becomes apparent that a designer must not only account for the influence of seal-tooth leakage in the design of the stator row in which leakage occurs but also consider the influence in downstream blade rows.

Circumferential Distributions Of Third Stator Exit Flow

Attention is now turned to the circumferential and radial distributions in the third stator exit flow properties. Discussion is not focused on the comparisons between Part 1 and Part 2 data, since similar trends can be seen in both data sets. Instead, these Part 2 distributions are presented in order to support hypotheses which describe how the entrained shrouded stator cavity leakage flow interacted with the power stream. Since the incoming flow was nearly identical for each case, spatial variations ahead of the stator are not reviewed. Similar tendencies in the data were observed at both operating conditions; however, only increased loading measurements are presented here. The variations in flow properties are presented as contour plots, covering a range of one stator pitch and 30% of the span. Exit velocity components are illustrated in Figures VII.7 (axial) and VII.8 (tangential). Flow angles and total pressure loss coefficients are depicted in Figures VII.9 and VII.10, respectively. Plots in each of the figures are placed from top to bottom in sequential order from the minimized to maximum leakage configuration. This aids in

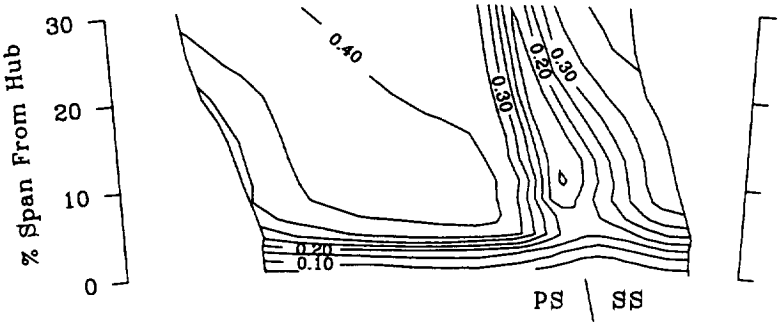

a) minimized leakage

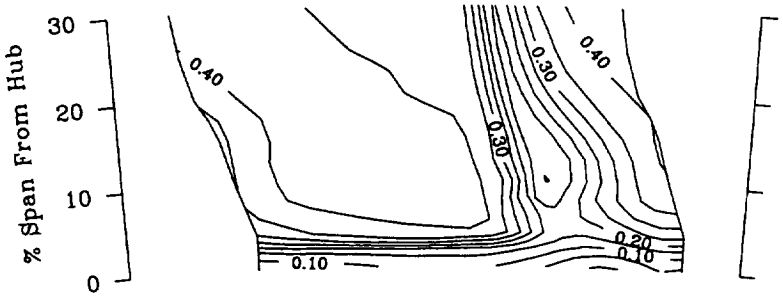

b) baseline leakage

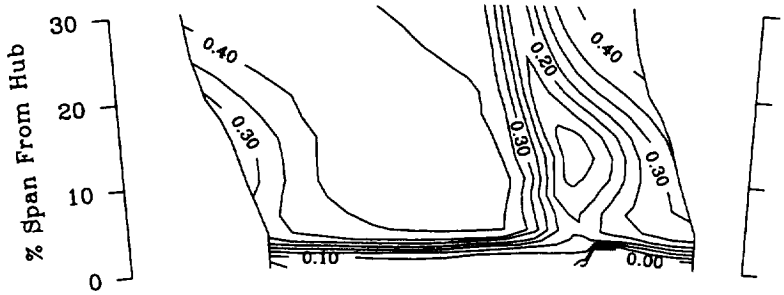

c) increased leakage

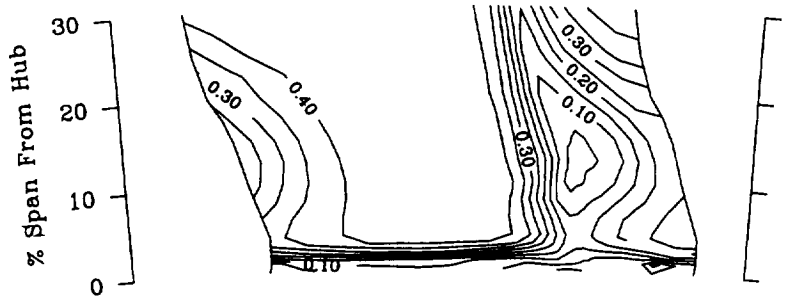

d) maximum leakage

Figure VII.7 Variations of stator 3 exit axial velocity at increased loading.

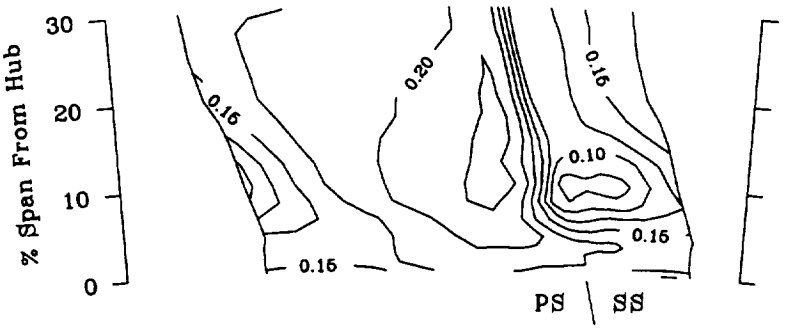

a) minimized leakage

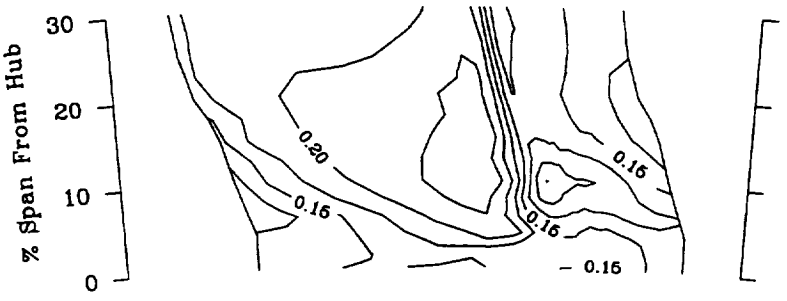

b) baseline leakage

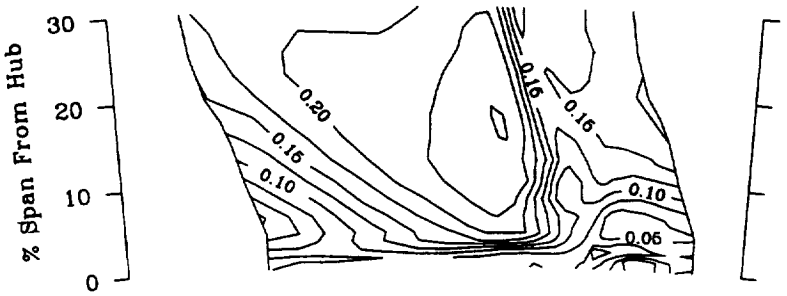

c) increased leakage

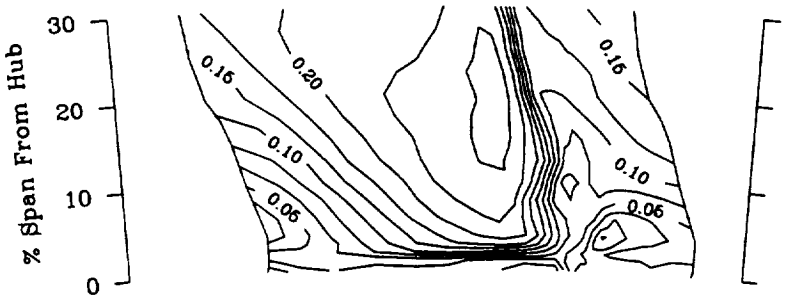

d) maximum leakage

Figure VII.8 Variations of stator 3 exit absolute tangential velocity at increased loading.

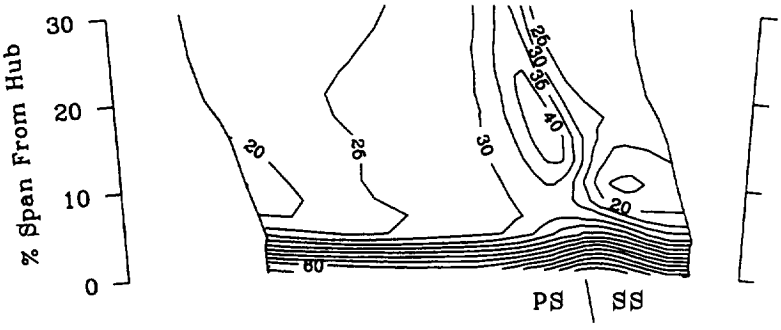

a) minimized leakage

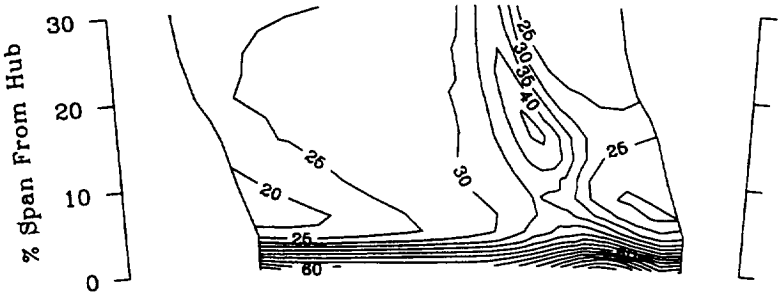

b) baseline leakage

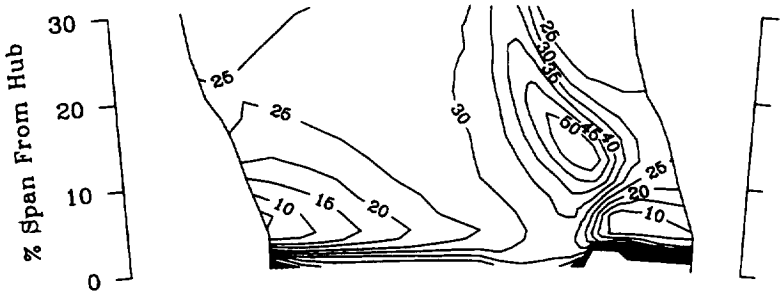

c) increased leakage

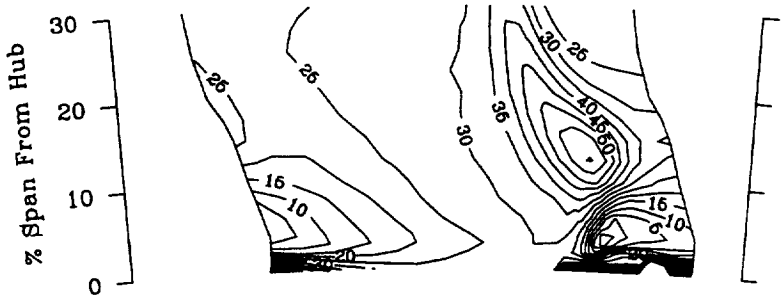

d) maximum leakage

Figure VII.9 Variations of stator 3 exit absolute flow angle at increased loading.

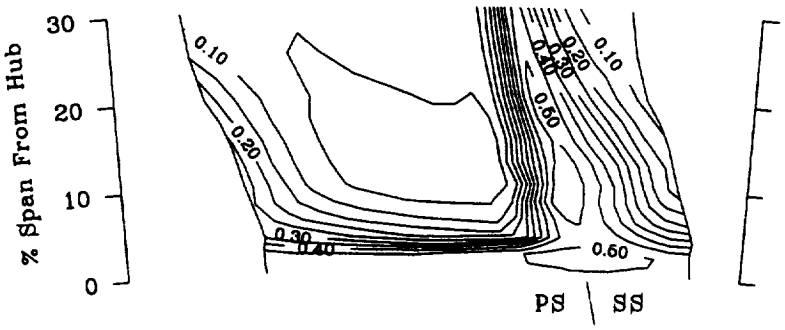

a) minimized leakage

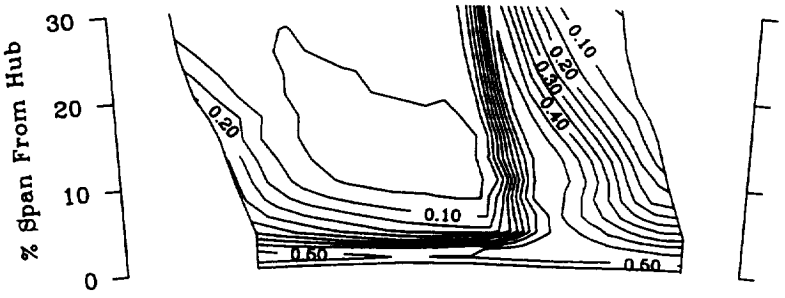

b) baseline leakage

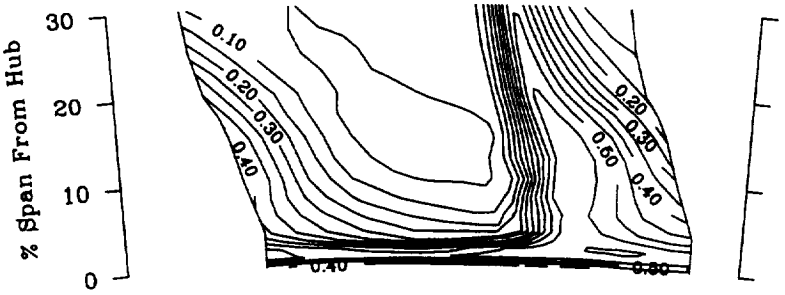

c) increased leakage

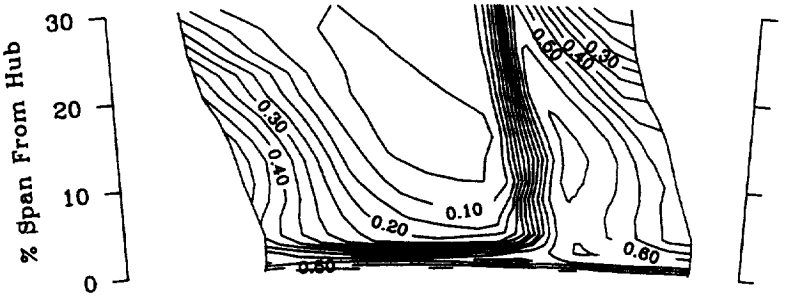

d) maximum leakage

Figure VII.10 Stator 3 total pressure loss distributions at increased loading.

viewing the dramatic influence seal-tooth leakage has on the stator exit flow field. Note that the no cavity / no leakage measurements are omitted.

It is proposed that as shrouded stator cavity leakage flow travels through the passage, it acts as suggested by Adkins and Smith [8]. Their concept is quickly reviewed here with some additional comments added. The flow in the upstream cavity is assumed to be low momentum fluid which becomes entrained by the power stream as it exits the cavity ahead of the stator. As it travels downstream through the passage, this low momentum fluid is driven circumferentially, from blade pressure to suction side, by the cross-channel pressure gradient which is set up by the turning of the primary flow. Some of the leakage fluid collects on the suction side of the blade and likely further worsens the state of the boundary layer there. The remaining leakage fluid exits the stator close to the hub, provided substantial mixing does not occur. This fluid is still low in momentum (low total pressure) and is highly overturned. As leakage is increased, the suction side boundary layer should appear to worsen over a larger percentage of the span because of the extra collected low momentum fluid there and/or additional degradation of the blade boundary layer. Furthermore, the region of the overturned flow exiting the stator should also increase in size with more fluid becoming further overturned. This process is illustrated in Figure VII.11 which shows idealized streamlines near the hub for small and large leakage amounts. Although described here in terms of pressure gradients and low momentum fluid, the process is identical to the tilting or stretching of a vorticity vector as it convects through the channel, with the production of secondary flows as envisioned by Smith [11] and Adkins and Smith [8]. The data in Figures VII.7–VII.10 support these premises.

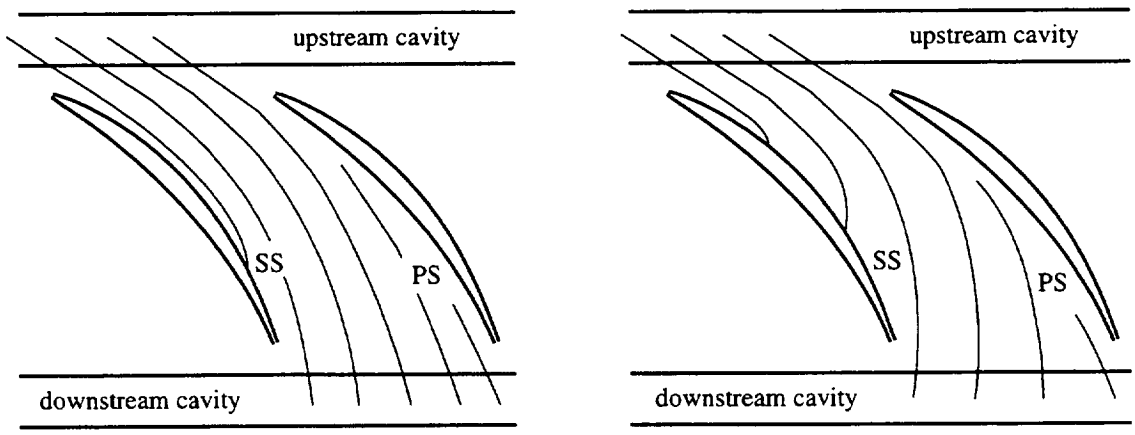

a) small amount of leakage b) large amount of leakage

Figure VII.11 Idealized streamlines near the hub for small and large leakage amounts.

Discussions are begun by first analyzing the stator exit flow field corresponding to the minimized leakage configuration. These data are represented by the top plots (a) in Figures VII.7—VII.10. For this configuration, the blade wake near the hub was slightly thickened. This can be seen in the axial velocity and loss distributions below 20% span when compared to 30% span data. At 10% span, a region of low axial velocity and high total pressure loss was present in about the middle of the blade wake. A small region of low tangential velocity also existed at the same radial location but slightly further off the suction side. In this area, flow angles were near 15°, which, for that radial location, implies zero deviation. Flow angles of 40° near 15% span (corresponds to deviation of 25°) indicate that perhaps a small region of separated / highly disrupted flow existed on the suction side of the blade. This is also supported by the higher values of loss there. (Separated flow was observed on the blade with tufts mounted to the suction side for the baseline configuration at increased loading.) From this review one may conclude that even though loading was quite high near the hub (DF = 0.6 at 10% span), the blade was performing quite well with only minimal regions of high blockage or loss and underturned or overturned flow exiting the stator.

As leakage was increased, the blade suction surface wake degraded substantially. This is probably best seen by the increase in total pressure loss shown in Figure VII.10. Between 10% and 20% span, just off the suction side, the region of high loss ($\omega > 0.25$) covered nearly half of the blade passage for the maximum leakage configuration while the maximum loss level rose above 0.65. At the same location, the wake axial velocity deficit became greater in both width and depth (Figure VII.7) while the flow angles progressively became more underturned (Figure VII.9). The region of greatest loss for the maximum leakage case (near 15% span) had near zero axial velocity and a peak flow angle reaching 60°. The higher loss across more of the passage also reduced the tangential velocity further off the suction surface (best seen toward the left side of the contour plots in Figure VII.8), while at the same time the extra blockage forced the fluid between wakes to increase in both axial and tangential velocity. All of these trends indicating the degradation of the blade suction surface wake are surmised to be caused by the additional collection of leakage fluid on the suction surface and/or further disruption of the blade suction surface boundary layer.

Increasing leakage also produced a larger region of overturned flow very near the hub and eliminated underturning at the hub. This is clearly seen in the flow angle distributions below 10% span as illustrated in Figure VII.9. For the maximum leakage configuration, 40% of the passage had overturned flow ($\beta < 15^o$) with a small region having flow angles below 5°. All of this fluid was low in total pressure, which was postulated above. These trends are surmised to be caused by the additional leakage fluid which does not collect on the suction surface, but instead exits the passage very near the hub.

The process proposed by Adkins and Smith [8] to account for the effects of seal-tooth leakage on compressor performance seems to, at least qualitatively, match quite well the trends of the data reported herein. In hindsight, this should not be surprising. Their thought development was influenced by data obtained from GE's large low-speed research compressor which was and is still effectively used as a multistage compressor design tool. The facility and blading used in these experiments are very similar to the ones utilized at and designed at GE. Therefore, it would be surprising to find the fluid mechanics modeling to be different. Of course, the model assumes that the entrained cavity leakage flow has low momentum compared to the power stream. This assumption is proven to be true for this compressor in Chapter VIII.

CHAPTER VIII

CAVITY FLOW FIELD CHARACTERISTICS

Spatial and temporal variations in the flow field within the up-and-downstream stator hub cavities are now reviewed. The data are presented to give compressor designers some indication of the complexities of the flows within the shrouded stator cavities in current engines. Emphases are place on simple descriptions of the flow properties with some probable explanations of why some of the observed variations existed. No attempt is made to assess which flow details, spatial or temporal, are absolutely needed to accurately model cavity flows in a design calculation. All data shown are for the third stage operating at the near peak efficiency condition for the baseline leakage rate on all four stages. Other data collected but not presented here indicate that the trends seen at this operating condition were also detected at increased loading. Furthermore, the other three cases having seal-tooth leakage also had similar cavity flow field characteristics.

Circumferentially Averaged Flow Details

It is useful to begin examining the details of the up-and-downstream cavity flow fields by reviewing the radial distributions of circumferentially averaged flow properties. This review provides a good representation of the general characteristics of the flow within the cavities without the added complexity of axial, circumferential and unsteady variations which occurred. Presented data are concentrated in the mid-gap regions of the up-and-downstream cavities of stator 3, cover a range from -10% to 10% span and represent the area average of 21 pitchwise measurements. The actual axial positions and radial extents of the measurements are indicated with vertical markers (ST 3.5 and ST 4.0) in Figure VIII.1. Where applicable, data acquired with both pneumatic and hotfilm probes are given.

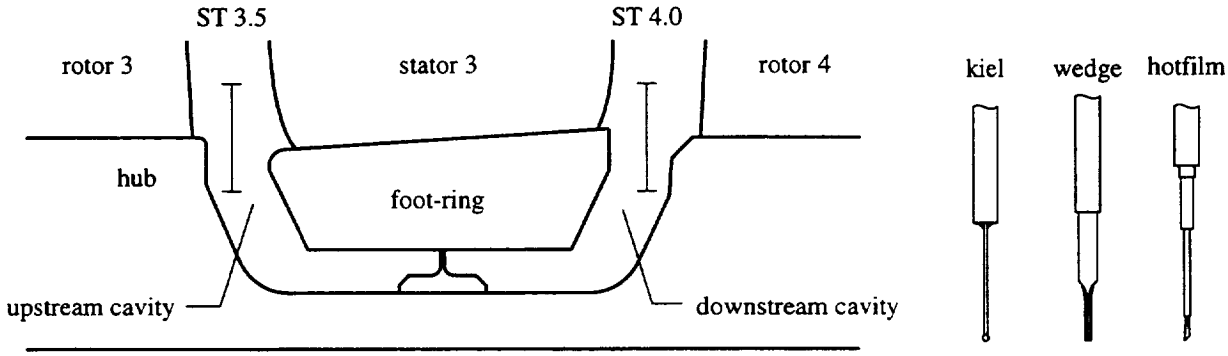

Figure VIII.1 Axial positions and spanwise extent of radial distributions of circumferentially averaged flow properties with scaled probe sizes.

Dramatic differences between cavity and power stream flow fields were noted. In general, the flow in the cavities involved low velocity fluid moving primarily in the circumferential direction. The data in Figure VIII.2 demonstrate that as the probes were traversed into the trench, little change in the static pressures were measured; however, large reductions in total pressures occurred. Since the nondimensional velocity magnitude can be approximated by Equation VIII.1, it is easy to confirm that the velocity magnitude within both cavities was much lower than that of the power stream.

$$\frac{V}{U_{tip}} \approx \sqrt{Cp_t - Cp_s} \qquad \text{(VIII.1)}$$

Traversing into the downstream cavity (ST 4.0), total pressure first decreased to a local minimum value and then increased. Since the static pressure remained nearly constant, the total pressure distribution gives evidence that as power stream fluid was drawn into the downstream well, it first lost but then gained momentum as it proceeded further into the cavity. This suggests that work was done on that fluid by the rotor drum. Figure VIII.2 also shows that the level of total pressure in the upstream cavity was less than in the downstream cavity, indicating a loss in total pressure as fluid moved across the seal-tooth from ST 4.0 to ST 3.5. Within the upstream cavity (ST 3.5) total pressure was nearly constant (-4 to -10% span) and even though there was a loss in total pressure across the seal-tooth, the upstream cavity velocity level was slightly greater than the downstream cavity velocity level because of the much lower static pressures at station 3.5. Flow within the cavities is shown to be primarily in the circumferential direction in Figure VIII.3 where flow angles acquired from both wedge and hotfilm probes are presented. Slight discrepancies between hotfilm and wedge probe data distributions at both stations are apparent, however, the trends are the same. At -10% span, data for both stations show the flow is nearly 90° from axial. For a portion of the span in the downstream cavity (ST 4.0), flow angles were measured to be greater than 90°. This indicates fluid moving in the negative axial direction.

Variations of axial and tangential velocities are presented in Figures VIII.4 and VIII.5, respectively. Interesting trends can be seen in both figures. Figure VIII.4 suggests an axial velocity distribution similar to a shear layer at both stations. At -10% span the axial velocity was virtually zero while at 5% span it was near the much larger power stream value. At station 4.0, negative axial velocities measured with the hotfilm probe are shown to be as large as 10% of the tip speed. These negative velocities correspond to the flow angles greater than 90° shown in Figure VIII.3. At 0% span, the axial velocity was not zero but nominally 20% of the tip speed (25% of the hub speed). Figure VIII.5 shows that the tangential velocity at station 3.5 could also be represented as a shear layer while at station 4.0 this was not true. In the downstream cavity the tangential velocity

first decreased and then increased as immersion into the trench became greater. This observed trend compliments the aurgument that the rotor drum quickly input work to the incoming cavity leakage fluid. At -10% span the tangential velocity was approximately 27% of tip speed (34% of the hub speed) at station 4.0 and was slightly less than 34% (43%) at station 3.5. This agrees with the velocity magnitude discussions.

Although available from hotfilm probes, circumferentially averaged radial velocity distributions are not presented. It will be stated in passing that station 3.5 circum-

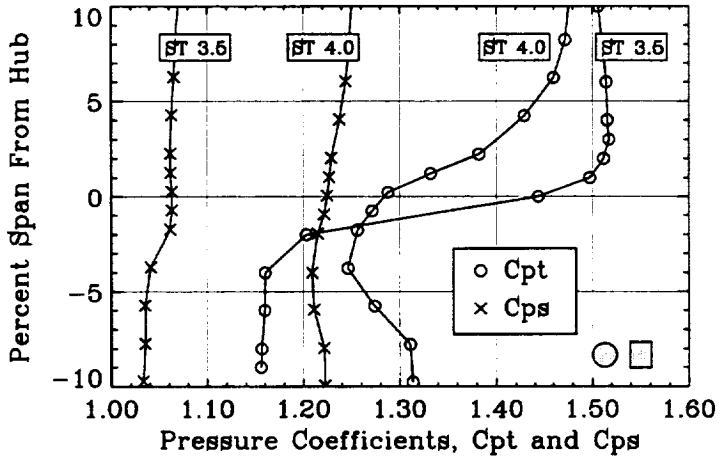

Figure VIII.2 Circumferentially averaged static pressures and total pressures in the upstream (ST 3.5) and downstream (ST 4.0) stator 3 cavities. Shaded symbols represent the kiel (circle) and wedge (rectangle) probe sensing regions.

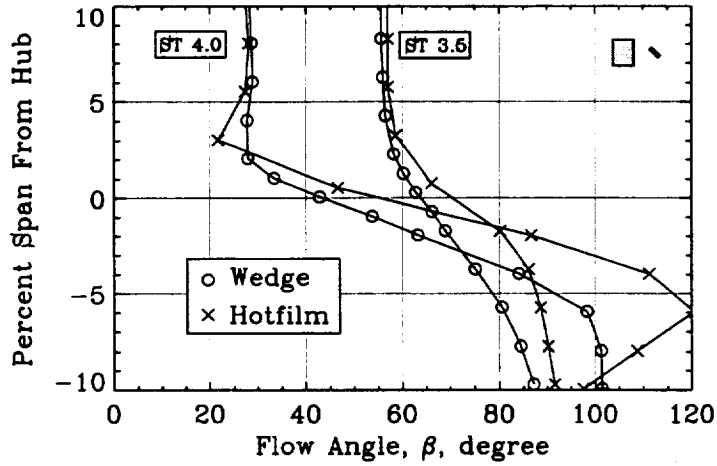

Figure VIII.3 Circumferentially averaged absolute flow angles in the upstream (ST 3.5) and downstream (ST 4.0) stator 3 cavities. Shaded symbols represent the wedge (rectangle) and hotfilm (slash) probe sensing regions.

ferentially averaged radial velocities were virtually zero while at station 4.0 they were approximately 4% of the tip speed. At first glance, this suggests mass was not conserved, since it appears that more flow went in at station 4.0 than came out at station 3.5. However, data were gathered at only one axial location at each station and so the mass flux across each gap was not actually measured.

The relatively large negative axial velocities within the downstream cavity (and small negative axial velocities in the upstream cavity) at first caused concern. It was envisioned

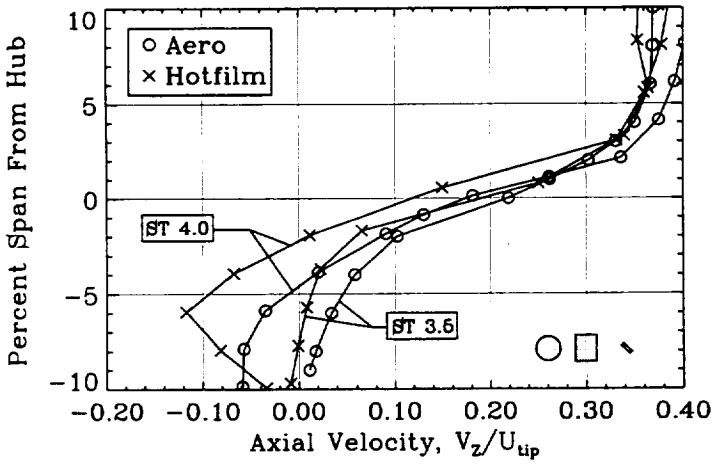

Figure VIII.4 Circumferentially averaged axial velocities in the upstream (ST 3.5) and downstream (ST 4.0) stator 3 cavities. Shaded symbols represent the kiel (circle), wedge (rectangle) and hotfilm (slash) probe sensing regions.

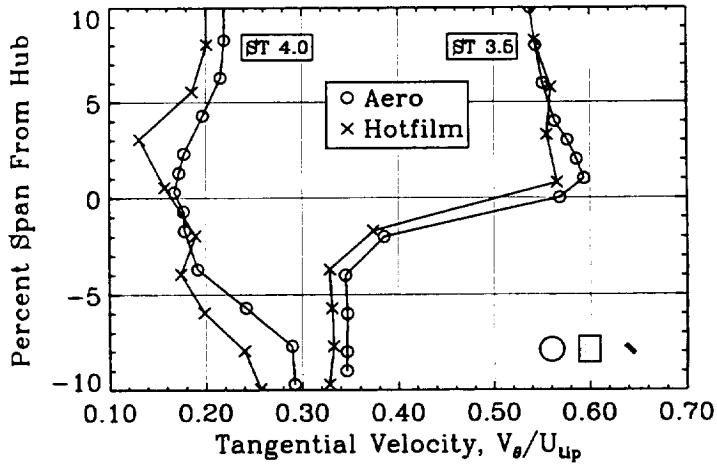

Figure VIII.5 Circumferentially averaged tangential velocities in the upstream (ST 3.5) and downstream (ST 4.0) stator 3 cavities. Shaded symbols represent the kiel (circle), wedge (rectangle) and hotfilm (slash) probe sensing regions.

that with seal-tooth leakage, fluid was drawn into or out of the cavity similar to that of a sink/source in potential flow. Data suggest that the flow within the cavity may be much more complex. The meridional velocity components in both the up-and-downstream cavities (shown in Figure VIII.6) indicate a vortical flow structure, similar to what would be produced by a driven cavity. Although this conclusion is drawn from very limited data, numerical results obtained by Heidegger *et al.* [22] support this hypothesis and data presented later in this chapter confirm the presence and extent of this vortical structure in the upstream cavity.

Circumferential Distributions Of Third Stator Cavity Flow

The distributions of circumferentially averaged flow properties proved that flow in the cavities was substantially different from flow in the power stream. Measurements also indicated circumferential variations in some flow properties within both the up-

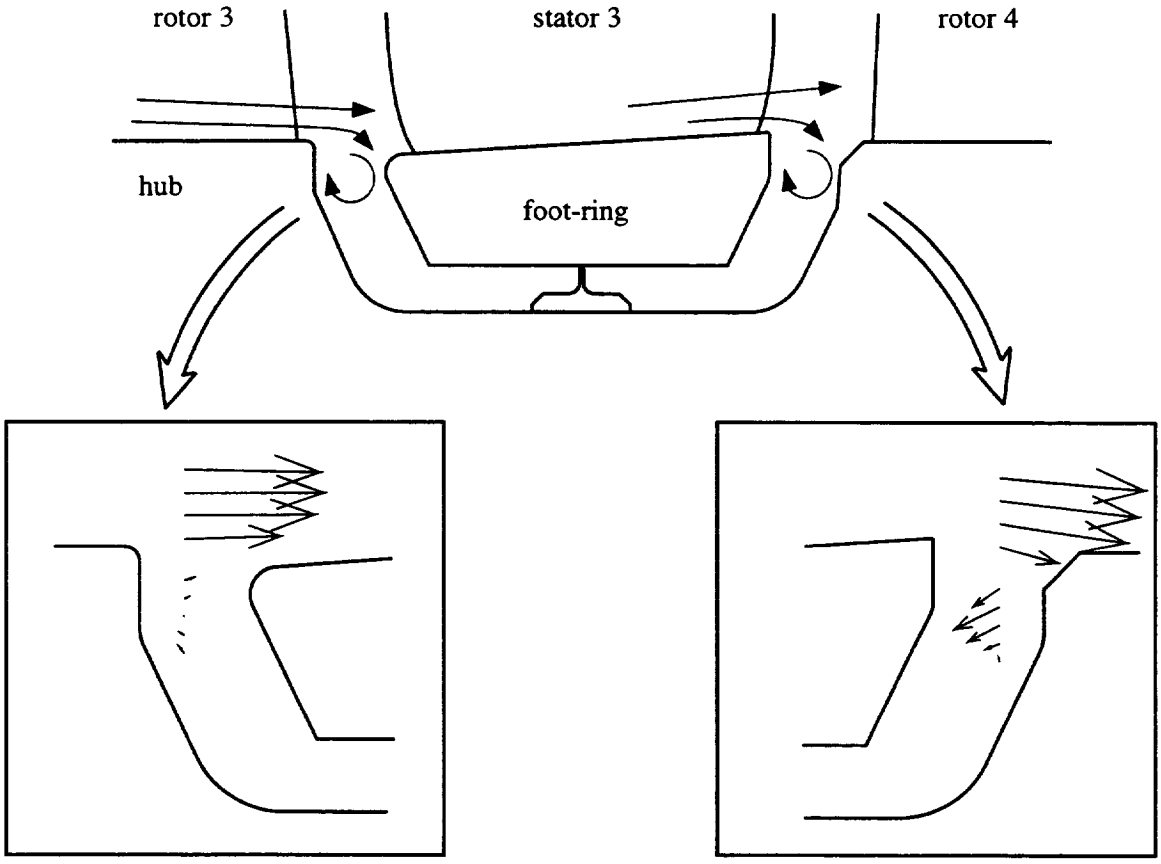

Figure VIII.6 Meridional velocity vector components in the upstream (ST 3.5) and downstream (ST 4.0) stator 3 cavities.

and-downstream cavities. These variations, which correspond to data gathered in the measurement windows shown in Figure VIII.1, are now reviewed.

Data from the upstream cavity (ST 3.5) reveal that the stator potential field penetrated into the cavity. This directly caused flow properties to vary virtually sinusoidally across a stator pitch. The penetration of the stator potential field into the upstream cavity can clearly be seen with the static pressure variations shown in Figure VIII.7. Here, static pressures acquired with a wedge probe are displayed across one stator pitch from –10% to 30% span. Note the circumferential boundaries of the data did not correspond to the actual leading edges of consecutive stator blades. Instead, straight axial projections of stator leading edges are represented by the two thick lines. The stator pressure and suction sides are also noted, indicating the flow was moving from left to right in the tangential direction. The distributions show the maximum static pressure coincided with the leading edge of the blade, while the minimum occurred near mid-pitch (approximately 40% pitch from the suction side). These variations extended to –10% span, although the sinusoidal amplitude at this location was about half that of the power stream.

The penetration of the potential field into the upstream cavity also influenced the pitchwise distribution of velocity components there. This can partially be seen in Figure VIII.8 which illustrates the time mean radial, tangential and axial velocity components acquired with a slant hotfilm probe. Note, these data cover the same spatial area as the static pressure distributions. Perhaps the most interesting feature in this data set are the radial velocity characteristics (Figure VIII.8a). At this axial location, the radial velocities near mid-pitch were positive, with a peak at 65% pitch from suction side. Small negative velocities were measured in front of the blade down to –8% span. Negative radial velocities (flow toward the hub) are denoted by dashed contour lines. It appears that seal-tooth leakage entered the power stream near mid-pitch but was suppressed near the stagnation point region ahead of the stator blade. One might at first question the

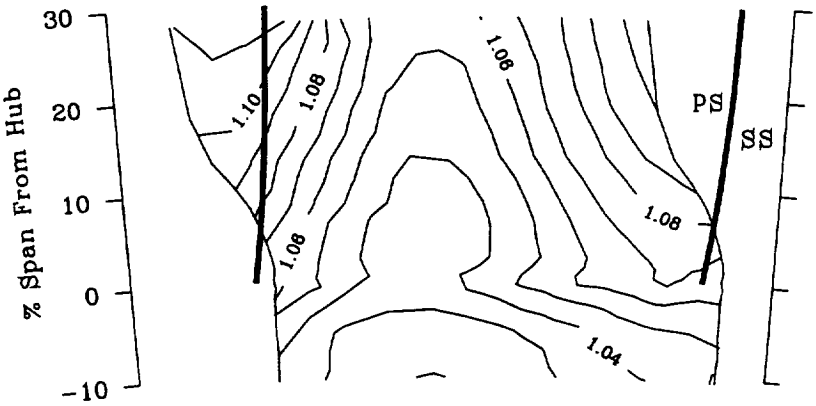

Figure VIII.7 Variation of static pressure (Cp_s) acquired with a wedge probe upstream of stator 3 and within the upstream cavity.

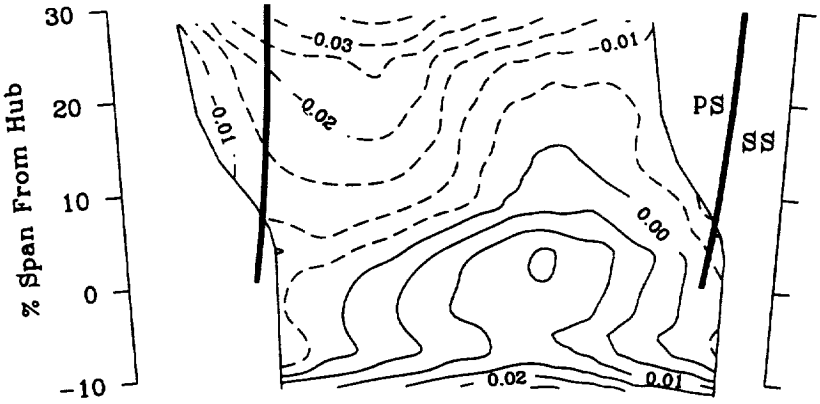

a) radial velocities, Vr / Utip

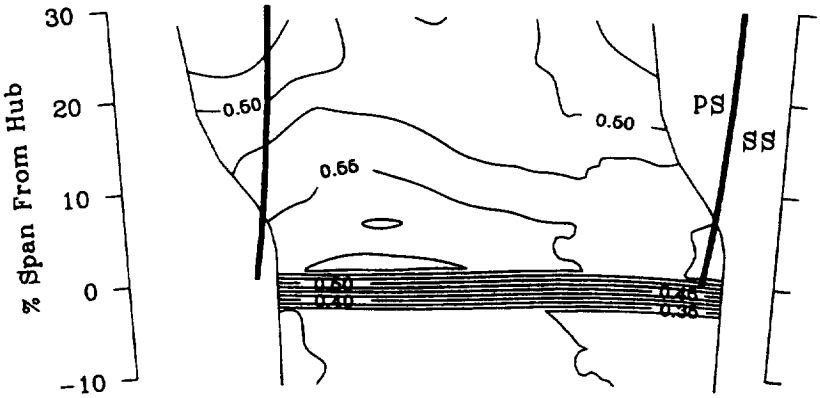

b) tangential velocities, Vθ / Utip

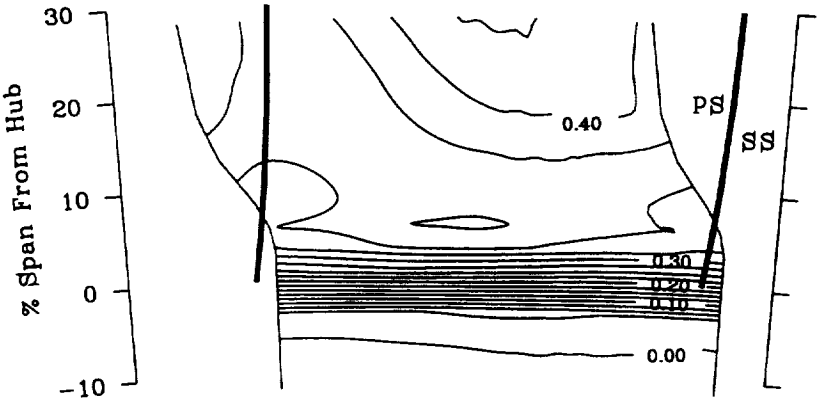

c) axial velocities, Vz / Utip

Figure VIII.8 Variation of time mean velocities (V_r, V_θ, V_z) acquired with a hotfilm probe upstream of stator 3 and within the upstream cavity.

validity of this conclusion, since the variations in radial velocity were quite small (at –5.7% span the peak-to-trough modulation was only 2% of the tip speed). However, this modulation represents a swing of flow pitch angle onto the probe of about 3.5°, which can be detected by the probe. So even if the absolute levels of radial velocity are off, the delta increments are thought to represent the actual trend. Data presented in the next two sections also support this conclusion.

Figure VIII.8b and c show a sharp reduction in tangential and axial velocity over the entire pitch near 0% span. These reductions were also shown in Figures VIII.5 and VIII.4. Since large contour intervals were used in both plots, little circumferential variation within the cavity can be detected. However, some variations did exist and to better illustrate them the measured values from –5.7% span are shown in Figure VIII.9. Here, a near sinusoidal variation in both velocities is depicted. For the tangential component, the peak-to-trough modulation was approximately 4% of tip speed which is comparable to the power stream value. For the axial component, the modulation was much less (1.5% of tip speed); however, this is similar to that seen in the radial velocity (2.0% of the speed). The tangential velocity distribution persisted to –10%, while the axial velocity amplitude was reduced to near zero by –10% span.

Virtually no circumferential variations of total pressure were detected within the upstream cavity. This is demonstrated by the near constant values of total pressure across the pitch at –6% span in Figure VIII.10. Figure VIII.10 also shows the measured static pressures at –5.7% span for comparison. The modulation in the total pressure was only a quarter of the static pressure modulation. Since the stator potential field should not influence the total pressure distribution for a steady uniform total pressure flow field,

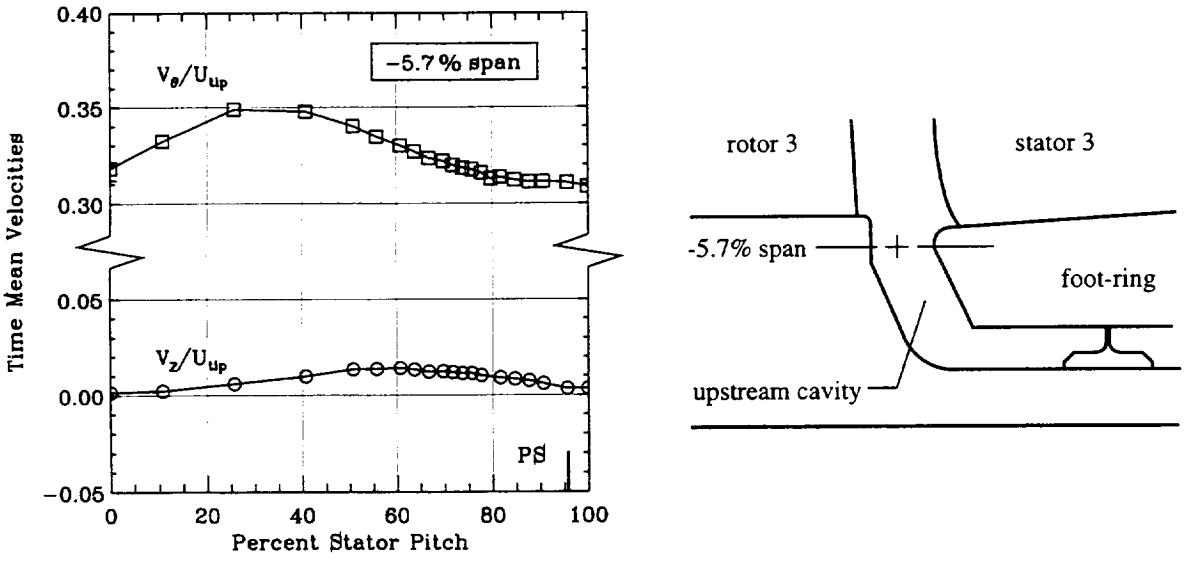

Figure VIII.9 Axial and tangential velocities at –5.7% span in the upstream cavity.

the slight variation in total pressure could be attributed to the convection of different total pressure fluid or nonuniform total pressure loss production within the cavity.

As in the upstream cavity, flow properties did vary circumferentially within the downstream cavity. Unlike the data from the upstream cavity, no clear trends were found or firm conclusions drawn from interrogation of downstream cavity data. Furthermore, most data taken with slow response instrumentation were questioned because of large unsteady velocity (flow angle) fluctuations measured there by fast response instrumentation (to be presented the next section). Therefore, comments on the downstream cavity flow field are limited to a brief review of the time mean velocities acquired with a slant hotfilm probe. All three velocity components (radial, tangential and axial) are displayed in Figure VIII.11. These measurements, gathered at the axial location shown in Figure VIII.1, cover a spatial range of one stator pitch and 40% span. The blade wake suction and pressure sides are noted in the axial velocity plot (Figure VIII.11c) and positive tangential velocities are in the clockwise direction.

The radial velocity distributions (Figure VIII.11a) again show the most interesting feature of the data set. Flow was moving radially inward at all locations, but, on a time mean basis, fluid near mid-passage was moving faster into the cavity (-5.5% tip speed) than wake fluid (less than –2.5% tip speed), the position of which is denoted by the low axial velocities in Figure VIII.11c. These circumferential variations diminished by –8% span. The variations found between 5% and –5% span are a curious result, and, like the upstream variations, were not expected. It is also noteworthy to mention relatively large positive radial velocities (4% tip speed) were measured in the hub wake at increased

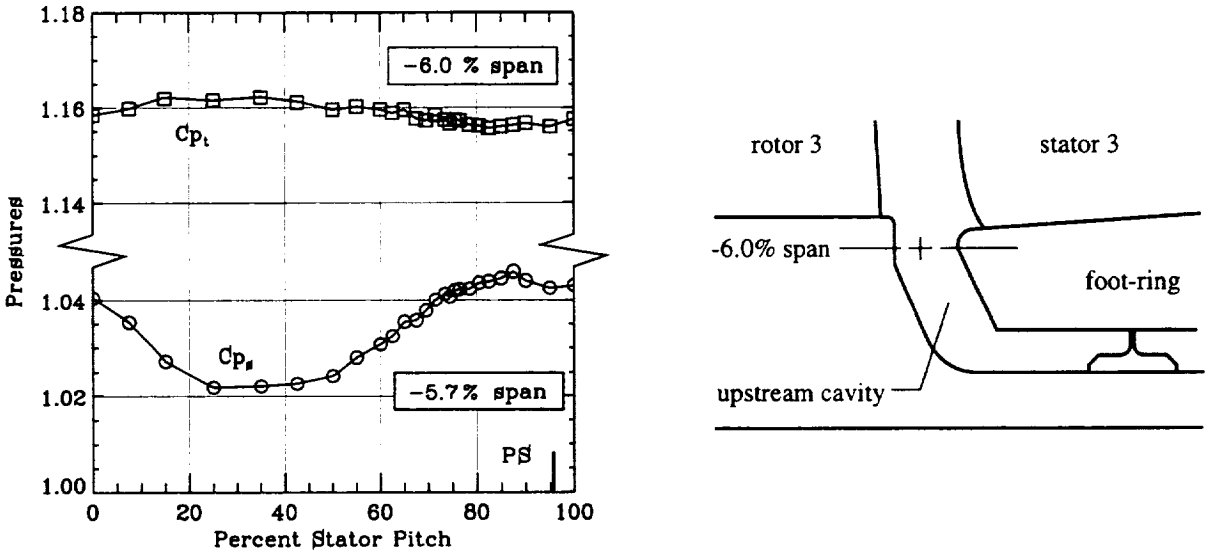

Figure VIII.10 Total and static pressures near –6.0% span in the upstream cavity.

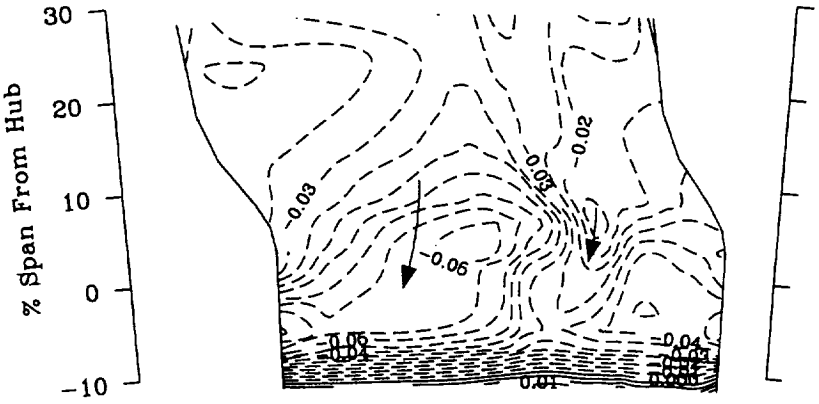

a) radial velocities, Vr / Utip

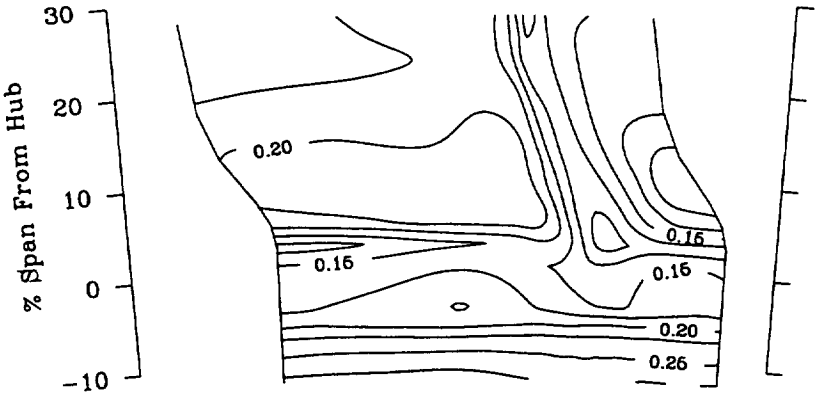

b) tangential velocities, Vθ / Utip

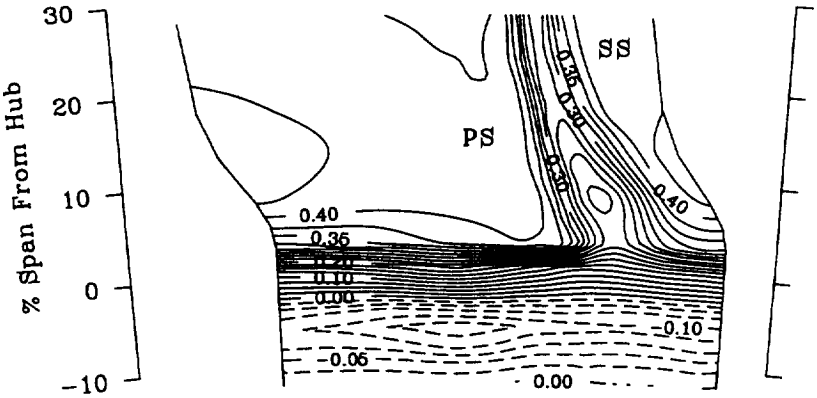

c) axial velocities, Vz / Utip

Figure VIII.11 Variations of time mean velocities (V_r, V_θ, V_z) acquired with a hotfilm probe downstream stream of stator 3 and within the downstream cavity

loading. Perhaps spanwise or secondary flows, setup in the passage, dictate which fluid particles end up in the downstream cavity.

As mentioned, the axial velocities can be used to define the location of the blade wake above 3% span. Below 3% span, the presence of the wake diminished (in terms of low axial velocity) and instead the rapid velocity decrease in the radial direction was the dominant gradient. The wake also had low tangential velocities (Figure VIII.11b), and possibly the lower momentum wake fluid may have caused some of the circumferential non-uniformity in tangential velocity between 1% and –4% span. Below –5%, these variations diminished and an increase of tangential velocity with immersion (as displayed in Figure VIII.5) occurred across the entire pitch.

Unsteady Velocities Correlated To Rotor Passing Frequency

Unsteadiness in the velocity components, corresponding to rotor passing frequency, existed in both the up-and-downstream cavities. This was determined by analyzing ensemble averaged velocities (averaged over all 39 rotor blades) acquired with fast response slant hotfilm probes. Although measurements were taken at many locations within the cavities, the trends to be noted were relatively independent of position, and, therefore, only data collected at one spatial position are reviewed here. The circumferential locations of the presented measurements, relative to the stator blade hub profile, are shown in Figure VIII.12.

Ensemble averaged velocities acquired at –5.7% span in the upstream cavity (ST 3.5) are depicted in Figure VIII.13 across one rotor pitch. The trailing edge of the rotor blade did not coincide with the once-per-rev trigger and instead is denoted by the solid vertical line at 4% rotor pitch. The pressure side of the blade was to the left of the line. The suction side was to the right. The radial and axial velocity traces reveal some temporal

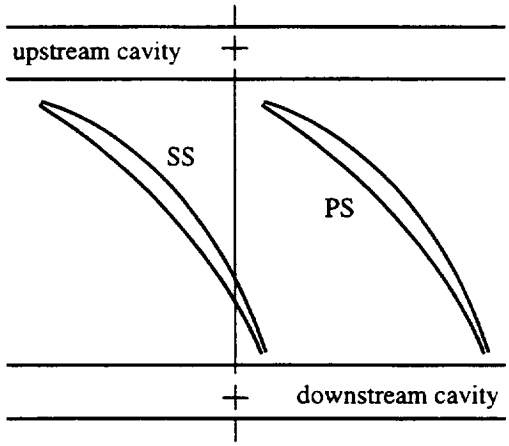

Figure VIII.12 Circumferential location of presented unsteady deterministic velocities.

variations, while the tangential velocity trace indicates virtually none. The modulation magnitudes in axial and radial velocity are comparable to those in the time mean data across a stator pitch (Figures VIII.8a and VIII.9). Slightly increased radial velocities existed near the trailing edge of the blade. This location also coincided with large positive radial velocities measured in the power stream wake. This suggests the unsteady power stream flow field did have some influence on the cavity flow. The measured fluctuations represent a unsteadiness intensity (similar to turbulence intensity) correlated with rotor passing frequency, defined by Equation VIII.2, of less than 1%. Note that this unsteadiness intensity does not include any random turbulent fluctuations, but represents only the intensity of the average unsteady flow field caused by the rotor passing.

$$Un = \frac{\sqrt{\frac{1}{3}\left(\widetilde{V_r'}^2 + \widetilde{V_\theta'}^2 + \widetilde{V_z'}^2\right)}}{\widetilde{V}} \qquad \text{(VIII.2)}$$

Ensemble averaged velocities acquired from –5.9% span in the downstream cavity are shown in Figure VIII.14 across one rotor pitch. The leading edge of the fourth rotor blade was also not in line with the once-per-rev trigger. Its position is denoted by the solid vertical line at 87% pitch with the pressure and suction sides of the blade as given. All velocity traces reveal substantial temporal variations. The sinusoidal distributions of radial and tangential velocities were similar to the time mean velocities found across the pitch in front of the stator (Figures VIII.8 and VIII.9). Radial velocity variations indicate that more fluid was being force into the downstream cavity when the rotor leading edge passed. Because of this and the sinusoidal nature of the distributions, it is

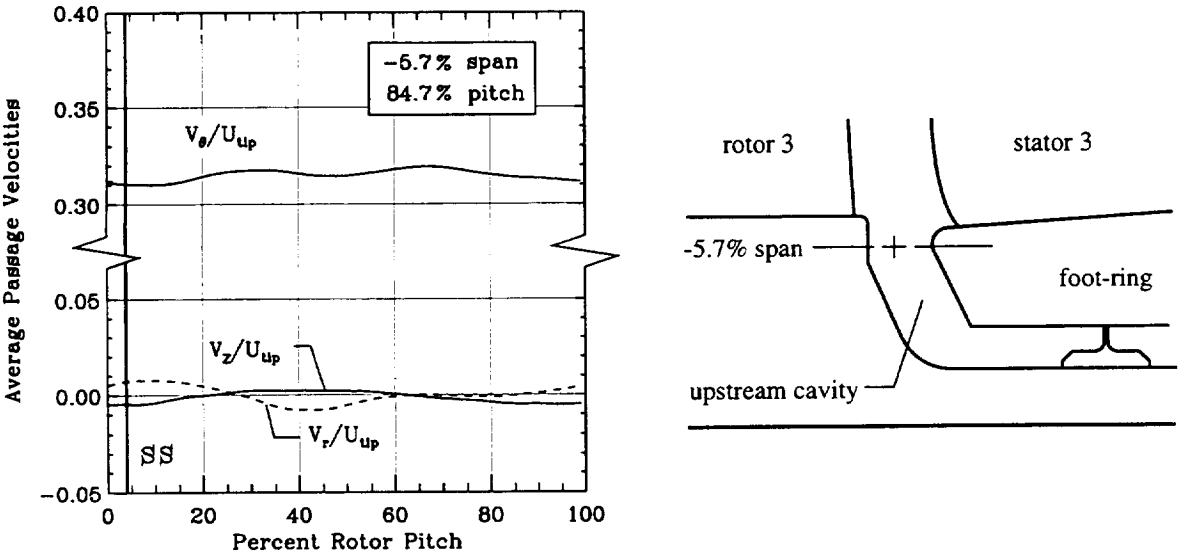

Figure VIII.13 Velocity variations across one rotor pitch in the upstream cavity.

proposed that the potential field, setup by the downstream fourth rotor blade, penetrated into the downstream stator cavity and influenced the velocity components there. This is exactly what occurred in the spatial distributions of time mean data in front of the third stator, however, this trend, now seen in front of the fourth rotor, occurred in time and not space because of the movement of the rotor relative to the stationary probe. These unsteady velocity fluctuations produced an unsteadiness intensity of 11%, which, unlike the upstream value, is quite high.

Further Flow Characteristics In The Upstream Cavity

Discussions of cavity flow field characteristics are concluded by examining some axial variations of flow found within the upstream cavity. Further measurements in the downstream cavity were not even attempted because of the large unsteady velocity fluctuations observed there. A calibrated (slow response) five-hole probe was used to measure the total pressure, static pressure and velocity components across a substantial portion of the upstream cavity gap in both radial (0% to −10% span) and axial (17% to 84% axial gap) extent. Two circumferential measurement locations relative to the stator blade hub profile and the meridional grid in which data were acquired are shown in Figure VIII.15. Yawing the probe head, while the probe stem was fixed at the axial measurement location shown in Figure VIII.1, allowed the entire axial distance to be traversed without having to physically reposition the probe stem to a new axial location.

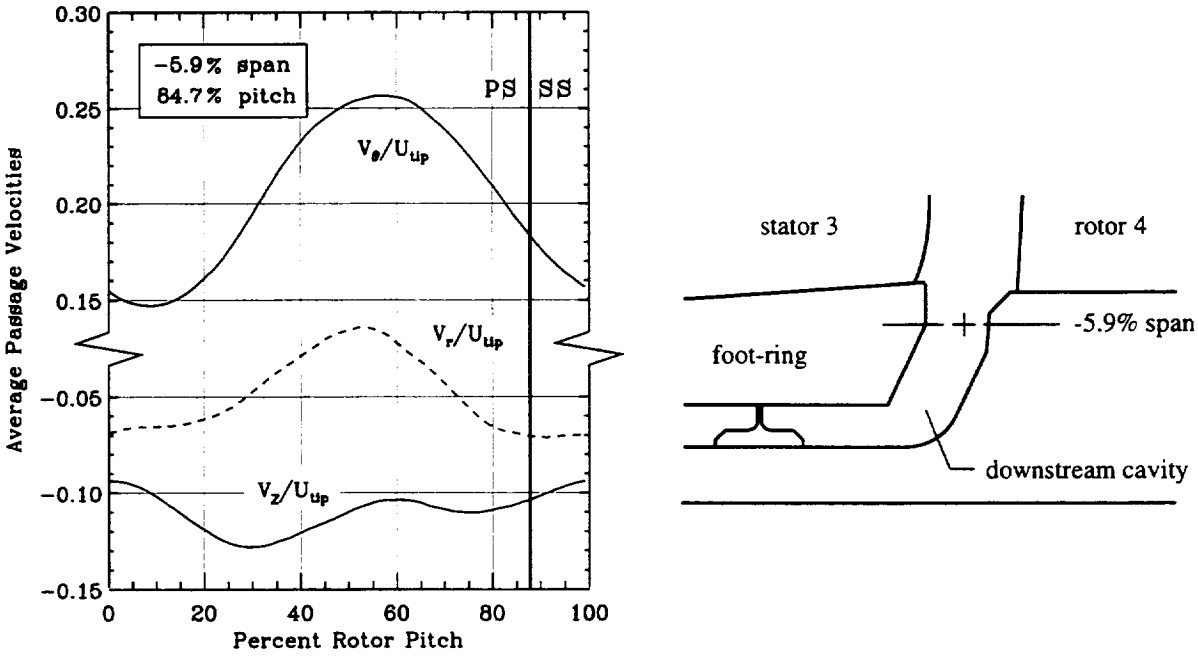

Figure VIII.14 Velocity variations across one rotor pitch in the downstream cavity.

Yawing the probe also created a non-nulled yaw alignment and, therefore, the probe was calibrated in both the pitch and yaw directions. While gathering data at different yaw locations, the position of the stator relative to the probe was adjusted to account for any slight deviation from the prescribed circumferential measurement location. Corrections were made during data reduction to account for significant flow property gradients in the radial direction.

Some axial variance in the flow existed at both circumferential locations. This is illustrated in Figures VIII.16 and VIII.17. Here, meridional distributions of total pressure and all three velocity components are presented across most of the axial gap and for 10% of the span. Static pressure distributions have been omitted, since only small variations were detected. The plots in Figure VIII.16 correspond to measurements collected near the stator mid-pitch (position A), while those in Figure VIII.17 were gathered near the stator leading edge (position B). Note the shaded triangles in the figures represent data which were outside the calibration range of the probe.

In general, the data at both positions (A and B) exhibited similar trends. As previously noted, above –3% span large gradients of total pressure, axial velocity and tangential velocity existed in the radial direction. Below –3%, the data reveal that the total pressure and tangential velocity levels were higher toward the stator foot-ring (past 50% axial gap), while the radial velocities were positive close to the rotor land and negative close to the stator foot-ring.

Although data from positions A and B exhibited similar trends, some subtle differences did exist. Below –3% span and across the entire axial gap, tangential velocities were lower in front of the stator leading edge than at mid-pitch. Likewise, axial velocities were lower in front of the stator leading edge than at mid-pitch. Both of these trends

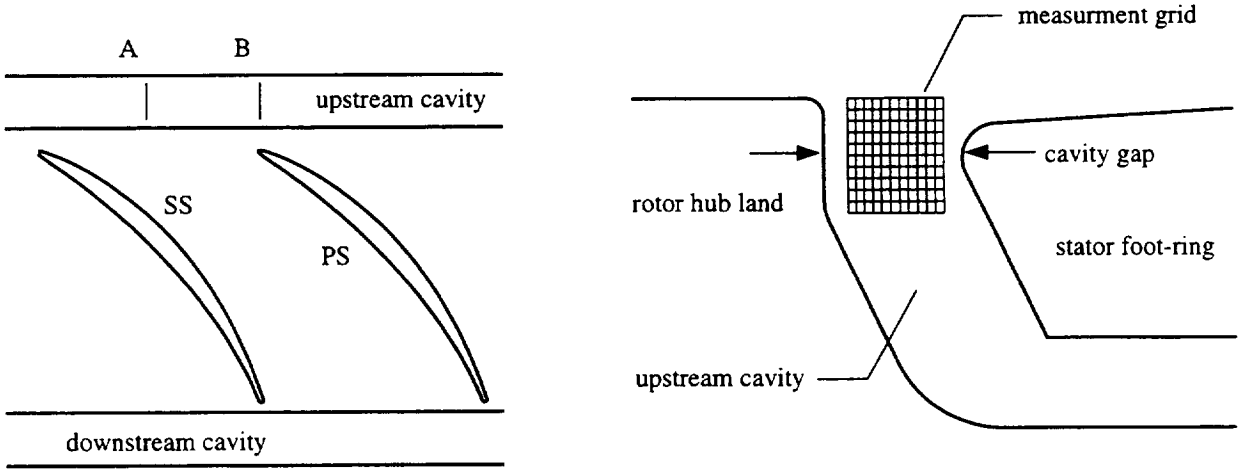

Figure VIII.15 Circumferential positions and meridional grid where five-hole data was gathered in the upstream cavity.

match those seen in Figure VIII.9, although the absolute levels between the two data sets were different. The radial velocities measured by the five-hole probe also indicate that the flow near the stator leading edge was moving more radially inward than that near mid-pitch. This was also shown in Figure VIII.8a, although, once again, the absolute levels between the two measurement techniques were different. The largest discrepancies in radial velocity between hotfilm and five-hole probe data occurred between 0% and –2% span. This is not surprising since large radial gradients in flow properties occurred there. These gradients directly affected the spatial resolution of the five-hole probe and even though corrections were made during data reduction to account for them, it is

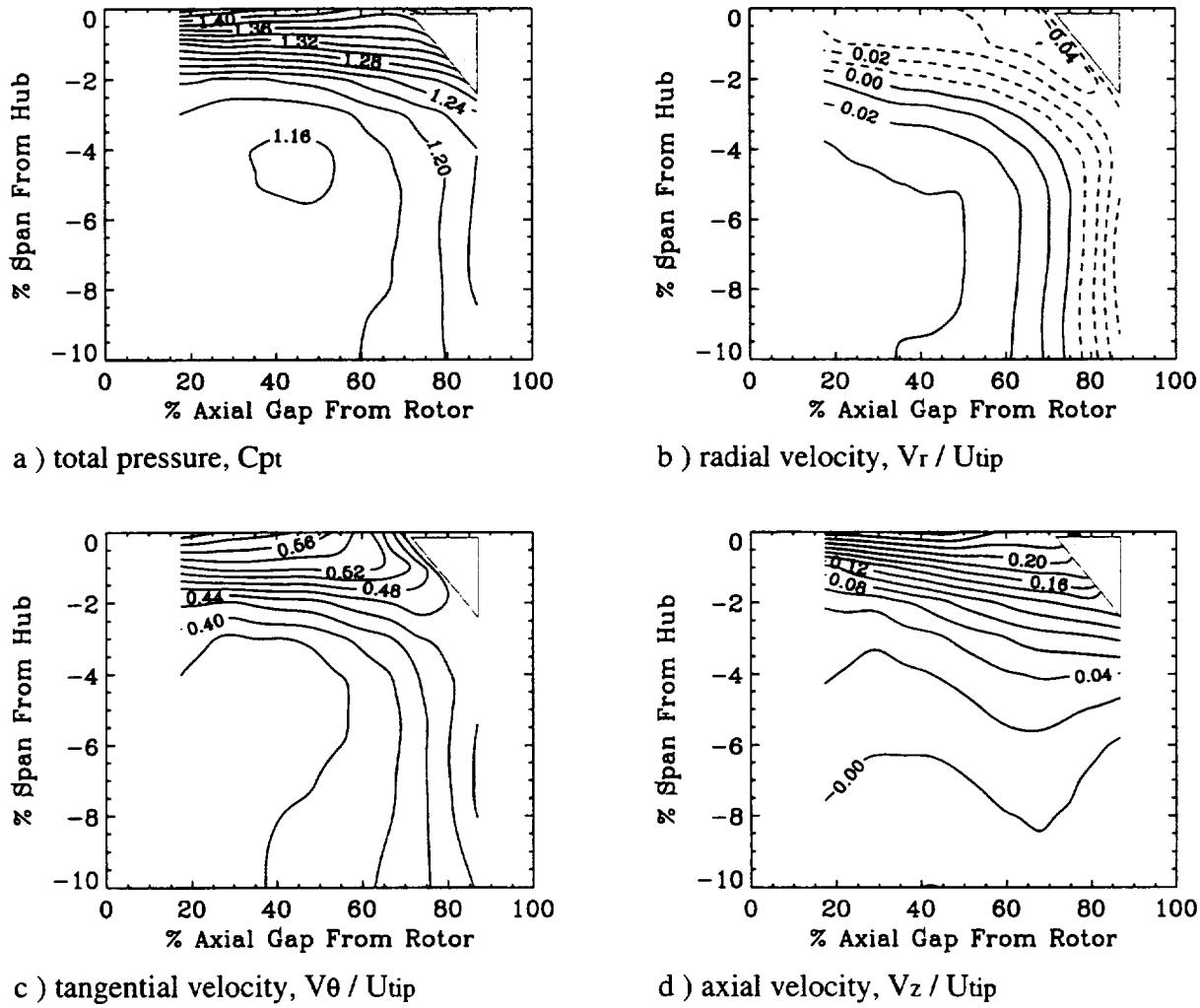

a) total pressure, Cpt

b) radial velocity, Vr / Utip

c) tangential velocity, Vθ / Utip

d) axial velocity, Vz / Utip

Figure VIII.16 Meridional distribution of flow properties near the stator mid-pitch (position A) in the upstream cavity. Shaded regions denote data outside the probe calibration range.

still unknown how a shear layer influences measurements acquired with five-hole type probes. To complicate matters, hotfilm measurements may have also been influenced in this region because of the normally high random turbulence intensity associated with shear layer flows. Therefore, the point is made that only the trends seen by the two measurement techniques are similar and not the absolute quantities.

It was previously surmised that a vortical flow structure existed in the meridional plane of the upstream cavity. The five-hole probe data prove this to be true. This can be inferred from the data already presented, but it is better visualized by reproducing the meridional velocity vectors as illustrated in Figure VIII.18. Mid-stator-pitch data are

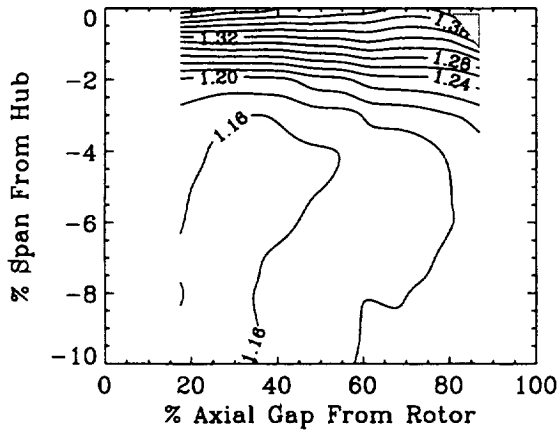

a) total pressure, Cpt

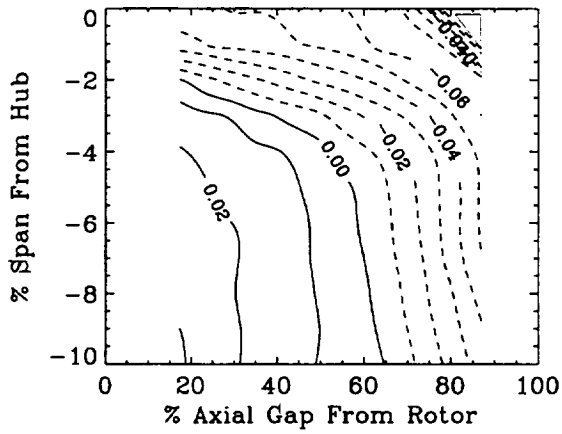

b) radial velocity, Vr / Utip

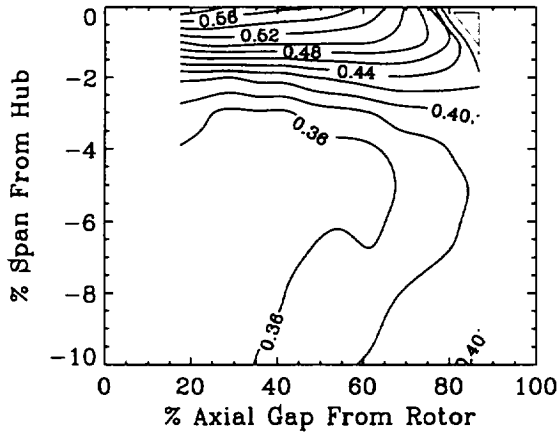

c) tangential velocity, Vθ / Utip

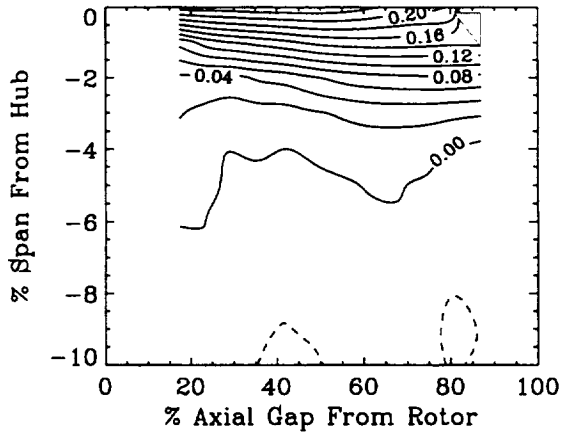

d) axial velocity, Vz / Utip

Figure VIII.17 Meridional distribution of flow properties near the stator leading edge (position B) in the upstream cavity. Shaded regions denote data outside the probe calibration range.

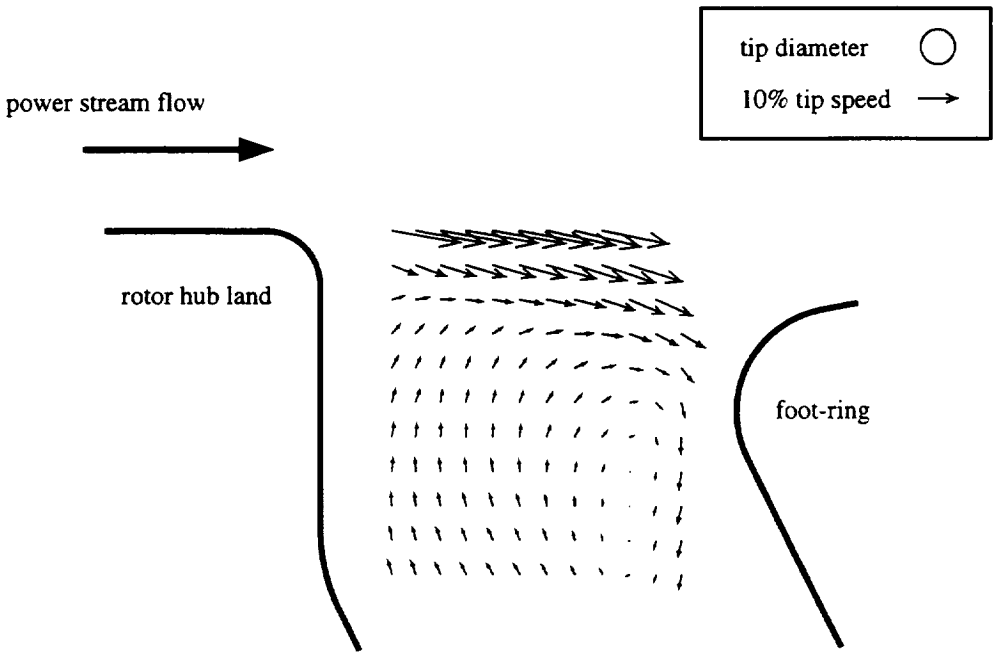

a) near stator mid-pitch (position A)

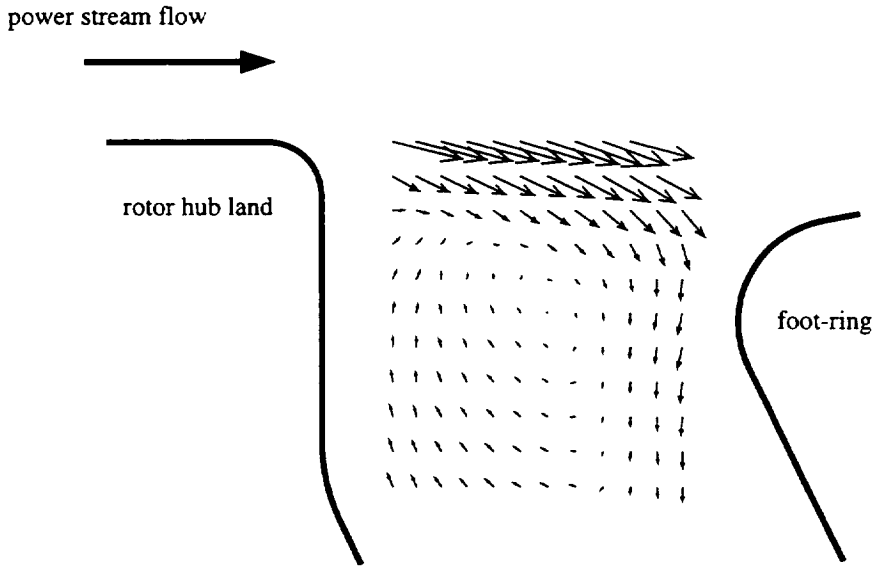

b) near stator leading edge (position B)

Figure VIII.18 Meridional velocity vectors in the upstream cavity.

presented in Figure VIII.18a, while those collected in front of the stator leading edge are shown in Figure VIII.18b. The shaded circle represents the probe tip diameter to scale and the power stream flow was from left to right. A vortical flow structure, similar to what would be produced by a driven cavity, was present at both circumferential locations. The influence of the stator leading edge on the radial velocities below the foot-ring leading edge is apparent. The position of the center of the vortical flow structure seemed to be influenced by where the stator leading edge was, being closer to mid-gap and higher span when the leading edge was close than for mid-pitch. The presence of this vortical structure was at first questioned. However, numerical calculations performed by Heidegger *et al.*[22] for a high-speed compressor support these observed trends. Therefore, it is now thought to be an actual feature of the flow field within the cavities.

Finally, it is important to restate that all of the trends presented in this chapter, corresponding to the baseline configuration near peak efficiency operation, were also detected at increased loading. Furthermore, pneumatic data acquired with kiel, wedge and five-hole probes for the other three cases with seal-tooth leakage and shrouded stator cavities showed similar cavity flow field characteristics.

CHAPTER IX

CONCLUSIONS

Experiments were performed on a multistage axial-flow compressor to assess the effects of shrouded stator cavity flows on overall compressor and stage aerodynamic performance. Other measurements were acquired to determine spatial and temporal flow field variations within up-and-downstream cavities. The data presented and conclusions drawn will help compressor designers wanting to include the influence of shrouded stator cavity flows in the design of multistage compressors and to engineers wanting to better understand the characteristics of the cavity flow field.

Results conclusively show that increasing labyrinth seal-tooth leakage degraded compressor performance. For every 1% increase in the seal-tooth clearance to blade-height ratio the compressor pressure rise dropped as much as 3% while efficiency was reduced by 1 to 1.5 points. These observed efficiency penalty slopes are comparable to those commonly reported for rotor and cantilevered stator tip clearance variations. Therefore, it appears that it is equally important to account for the effects of seal-tooth leakage as it is to include the influence of tip clearance flows in correctly predicting overall performance.

Shrouded stator cavities alone without any leakage probably have little impact on compressor performance. Some performance improvement did occur when solid foot-ring extensions were installed in the test rig to conceal the cavities. However, this improvement correlated well with the further reduction in leakage flow caused by concealing the cavities. Concealing the cavities simply reduced the seal-tooth leakage to near zero with expected improved performance.

Importantly, neither concealing the cavities nor changing the amount of seal-tooth leakage altered the stalling flow coefficient of this compressor.

The overall performance degradation, observed when leakage was increased, was brought about in two distinct ways, both related to a weakened hub endwall flow. First, increasing seal-tooth leakage directly degraded the performance of the stator row in which leakage occurred. The recirculation of more low momentum leakage fluid produced additional flow blockage, deviation and total pressure loss near the stator hub endwall. The extra blockage forced more fluid radially outward toward the case, thereby substantially unloading a significant spanwise portion of the stator. Second, the altered stator exit flow conditions, caused by increased leakage, impaired the performance of the next downstream stage. The redistribution of stator exit flow caused the next downstream rotor to work less over the outer portion of the span, while near the hub the work input remained the same, thereby reducing overall pressure rise. Furthermore, the downstream

rotor did not tend to "heal" the maldistributed incoming flow near the hub and the flow distributions into the next stator were also modified (mainly higher incidence angles near the hub). This worsened the performance of that downstream stator by increasing flow blockage, deviation and total pressure loss.

This double impact caused, in this compressor, the performance of downstream stages to become progressively worse when seal-tooth clearances where increased simultaneously on all four stages. Of the total pressure rise reduction of an embedded stage, approximately 40% of it was caused simply by the extra leakage in that stage while 50% was attributed to the incoming flow conditions worsened by upstream leakage. The total amount of blockage and total pressure loss produced in the third stator when all seal-tooth clearances where increased simultaneously was also affected by these two factors. Nearly 65% of the extra blockage and 60% of the extra total pressure loss was caused solely by the increase in third stage leakage. The rest was attributed to worsening inlet flow conditions into the third stator caused by upstream leakage. From these conclusions it becomes apparent that a designer may not only have to account for the influence of seal-tooth leakage in the design of the stator row in which leakage occurs but also in all downstream blade rows as well.

Flow within the cavities primarily involved low momentum fluid traveling in the circumferential direction at about 40% of the hub wheel speed. Measurements indicate that the flow within both cavities was much more complex than what was first envisioned. Spatial and temporal variations in flow properties did exist. Some of these variations were due to the upstream potential flow field influence of the next downstream blade row, while other variations were caused simply by flow over a recessed cavity. The presence of the potential flow field, generated by either a rotor or stator blade, in general forced fluid down into the cavity. In the upstream cavity, inward radial velocities were present nearly in line with the stator blade leading edge while outward radial velocities existed near mid-stator-pitch. This produced a circumferential variance in the entrance of seal-tooth leakage flow into the power stream. In the downstream cavity, inward radial velocities were present across the entire pitch; however, substantially more fluid went radially inward near the rotor leading edge than at mid-rotor-pitch. The upstream potential flow influence of the downstream rotor also caused the velocity unsteadiness within the downstream cavity to be much greater than in the upstream cavity. The action of flow over recessed cavity produced a vortical flow structure in the meridional plane within the upstream cavity, similar to what would be found in a driven cavity. In the upstream cavity this structure was present both in front of the stator leading edge and near mid-pitch and is believed to be across the entire stator pitch. Modeling this three-dimensional unsteady flow remains a challenge.

CHAPTER X

RECOMMENDATIONS FOR FUTURE RESEARCH

The experiments reported herein have proven that seal-tooth leakage affected the performance of this compressor. Although believed to be a general tendency for most compressors, this conclusion has not been generally proven. It would be beneficial to repeat similar experiments with different compressor blading designs to assess the generality of seal-tooth leakage influence on compressor performance. Particularly, studies on blading which are less loaded near the hub would be useful. The loading on the current blades could, perhaps, be altered by changing the inlet axial velocity profile into the compressor. More data could benefit designers wanting to know the generalities of the observed trends.

Future studies should be carried out to better evaluate how or if the presence of shrouded stator cavities alone influence compressor performance. In this study, concealing the cavities did not alter performance to an extent that the influence of the cavities alone could be assessed. Still, it has been a long standing belief that cavities can increase the stalling flow coefficient, especially with inlet circumferential distortion. An investigation to specifically address this notion would be useful to designers wanting to better predict the stall point of a compressor.

Some middle stages of multistage compressors involve variable stator blade geometries. Because of this, clearance between the stator blade hub and annular foot-ring may exist in production engines. The experiments in this study were conducted with all stator blade hub clearances sealed. Therefore, a separate study to investigate how this endwall clearance flow may impact the effects on compressor performance observed when seal-tooth leakage flow exists would also be useful.

More data which clarify the axial variations in flow within the downstream cavity should be gathered. Unfortunately, it is felt this would have to be acquired with time consuming fast response instrumentation because of the large fluctuations in the flow field there caused by the passing of the downstream rotor blades.

The data collected in this study should be used to improve models which try to incorporate the influence of shrouded stator cavity flows in compressor design. Currently, a simple control volume approach to predict the increase in total pressure loss, which occurred with more seal-tooth leakage, is being evaluated. Design throughflow codes which already utilize an existing shrouded stator cavity flow model could be calibrated against this data. A method which accurately models the essential spatial and temporal variations of a cavity flow field for establishing CFD boundary conditions needs to be

developed. This would allow designers using CFD codes to incorporate the influence of shrouded stator cavity flows without having to grid the entire shrouded stator cavity.

BIBLIOGRAPHY

[1] Ludwig, L., "Gas Path Sealing in Turbine Engines," *Seal Technology in Gas Turbine Engines*, AGARD, AGARD Publications, Neuilly Sur Seine France, Apr. 1978. (also NASA TM 73890).

[2] Wisler, D. C., *Advanced Compressor and Fan Systems*, GE Aircraft Engines, Cincinnati, Ohio, 1988. (Also 1986 Lecture to ASME Turbomachinery Institute, Ames, Iowa).

[3] Freeman, C., "Effect of Tip Clearance Flow on Compressor Stability and Performance," von Karman Institute For Fluid Dynamics Lecture Series 1985-05, Apr. 1985.

[4] Wennerstrom, A. J., "Highly Loaded Axial Flow Compressors: History and Current Developments," *ASME Journal of Turbomachinery*, Vol. 112, Oct. 1990, pp. 567–578.

[5] Wennerstrom, A. J., "Low Aspect Ratio Axial Flow Compressors: Why and What It Means," *ASME Journal of Turbomachinery*, Vol. 111, Oct. 1989, pp. 357–365.

[6] Jefferson, J. L. and Turner, R. C., "Some Shrouding and Tip Clearance Effects in Axial Flow Compressors," *International Ship Building Progress*, Vol. 5, 1958, pp. 78–101.

[7] Mahler, F. H., "Advanced Seal Technology," Pratt and Whitney Aircraft Division Tech. Rep. PWA-4372, Feb. 1972. (also AFAPL TR-72-8).

[8] Adkins, G. G. and Smith, L. H., "Spanwise Mixing in Axial-Flow Turbomachines," *ASME Journal of Engineering for Power*, Vol. 104, Jan. 1982, pp. 97–110.

[9] Wisler, D. C., Bauer, R. C., and Okiishi, T. H., "Secondary Flow, Turbulent Diffusion and Mixing in Axial-Flow Compressors," *ASME Journal of Turbomachinery*, Vol. 109, Oct. 1987, pp. 455–482.

[10] LeJambre, C. R., Zacharias, R. M., Biederman, B. P., Gleixner, A. J., and Yetka, C. J., "Development and Application of a Multistage Navier-Stokes Flow Solver, Part II: Aplication to a High Pressure Compressor Design," ASME Paper 95-GT-343, June 1995.

[11] Smith, L. H., "Secondary Flow in Axial-Flow Turbomachinery," *Transactions of the ASME*, Vol. 77, Oct. 1955, pp. 1065–1076.

[12] Denton, J. D., "Loss Mechanisms in Turbomachinery," *Journal of Turbomachinery*, Vol. 115, Oct. 1993, pp. 621–656.

[13] Heidegger, N. J., Hall, E. J., and Delaney, R. A., "Parameterized Study of High-Speed Compressor Seal Cavity Flow," AIAA Paper 96-2807, July 1996. (to be presented at the 1996 32nd AIAA/ASME/SAE/ASEE Joint Propulsion Conference).

[14] Wasserbauer, C. A., Weaver, H. F., and Senyitko, R. G., "NASA Low-Speed Axial Compressor for Fundamental Research," NASA TM 4635, Feb. 1995.

[15] Wisler, D. C., "Core Compressor Exit Stage Study : Volume 1 - Blade Design," NASA CR 135391, Dec. 1977.

[16] Wisler, D. C., "Data Analysis Plan for the Core Compressor Exit Stage Study," General Electric TM 77-271, June 1977.

[17] Lieblein, S., "Experimental Flow in Two Dimensional Cascades," *Aerodynamic Design of Axial Flow Compressors*, edited by I. A. Johnsen and R. o. Bullock, National Aeronautics and Space Administration, Washington, D.C., 1965, pp. 183–226. (NASA SP-36).

[18] Alverson, R. F. Private communications, Jan. 1996.

[19] Steinetz, B. M. and Hendricks, R. C., "Engine Seal Technology Requirements to Meet NASA's Advanced Subsonic Technology Program Goals," AIAA Paper 94-2698, June 1994. (also NASA TM 106582).

[20] Cumpsty, N. A., *Compressor Aerodynamics*, Longman Scientific and Technical, Essex CM20 2JE England, 1989.

[21] Smith, L. H., "Casing Boundary Layers in Multistage Axial-Flow Compressors," *Flow Research on Blading*, edited by L. S. Dzung, Elsevier Publishing, Amsterdam, Netherlands, 1970, pp. 275–304.

[22] Heidegger, N. J., Hall, E. J., and Delaney, R. A., "Seal Cavity Flow Investigation : Monthly Progress Reports," Performed under NASA Contract NAS3-25950, Feb. 1994 - Jan. 1996.

[23] Coleman, H. W. and Steele, W. G., *Experimentation and Uncertainty Analysis for Engineers*, John Wiley and Sons, New York, NY, 1989.

[24] Blumenthal, P. Z., "A PC Program for Estimating Measurment Uncertainty for Aeronautics Test Instrumentation," AIAA Paper 95-3072, July 1995. Also NASA CR 198361.

[25] Moffat, R. J., "Contributions to the Theory of Single-Sample Uncertainty Analysis," *ASME Journal of Fluids Engineering*, Vol. 104, June 1982, pp. 250–260.

[26] Moffat, R. J., "Using Uncertainty Analysis in the Planning of an Experiment," *ASME Journal of Fluids Engineering*, Vol. 107, June 1985, pp. 173–178.

[27] Everett, K. N., Gerner, A. A., and Durston, D. A., "Seven-Hole Probes for High Flow Angle Measurement : Theory and Calibration," *AIAA Journal*, Vol. 21, July 1982, pp. 992–998.

[28] DeGrand, G. and Kool, P., "An Improved experimental method to determine the complete Reynolds' Stress Tensor With a Single Slant Hot Wire," *Journal of Physical Engineering : Scientific Instrumentation*, Vol. 14, 1981.

[29] Smout, P. D. and Ivey, P. C., "Wall Proximity Effects in Pneumatic Measurement of Turbomachinery Flows," ASME Tech. Rep. 94-GT-116, 1994.

APPENDIX A

UNCERTAINTY ANALYSIS

An analysis was conducted to estimate the uncertainty of the calculated overall, individual stage and blade element performance parameters. The analysis used propagation of error techniques as described in Colemann and Steele [23]. Error estimates of data collected with five-hole and hotfilm probes have been omitted since these measurements were used mainly for qualitative purposes. Details of the analysis and results for both First-Order and *N*th-Order uncertainties are presented.

First-Order uncertainties refer to precision errors. The propagation process accounted for errors which were random as the experiment was conducted and predicts the amount of scatter which would result from repeated trials using the same test apparatus and instruments. For precision errors, the uncertainty of a dependent variable (δf_p) is given by Equation A.1. Here, $x_1, x_2 ... x_i$ are the independent variables and δx_i refers to the known uncertainty associated with the independent variable x_i. Independent variable uncertainty values were obtained by taking twice the standard deviation of 30 measured samples while at the design point operating condition.

$$\delta f_p = \left\{ \sum_{i=1}^{I} \left[\frac{\partial f}{\partial x_i} \delta x_i \right]^2 \right\}^{1/2} \tag{A.1}$$

$$\delta f_b = \left\{ \sum_{i=1}^{I} \left[\left(\frac{\partial f}{\partial x_i} \delta x_i \right)^2 + \sum_{j=1}^{I} \frac{\partial f}{\partial x_i} \frac{\partial f}{\partial x_j} \delta x_i \delta x_j \varrho_{ij} (1 - \delta_{ij}) \right] \right\}^{1/2} \tag{A.2}$$

$$\delta f = \left(\delta f_p^2 + \delta f_b^2 \right)^{1/2} \tag{A.3}$$

*N*th-Order estimates of uncertainty include the precision errors together with all the bias errors which influenced the measurements. Precision errors were taken from the First-Order estimates. The bias uncertainty of a dependent variable (δf_b) was calculated with Equation A.2, which accounts for correlated bias limits. Again, $x_1, x_2 ... x_i$ are the independent variables and δx_i refers to the known uncertainty associated with the independent variable x_i. Bias limits were obtained from Blumenthal [24] or better judgement. If bias limits were dependent, they were assumed perfectly correlated ($\varrho_{ij} = 1$). The Kronecker delta (δ_{ij}) was zero when $i = j$ and one when $i \neq j$. The *N*th-Order uncertainty estimate was found by taking the root sum square of bias and precision errors (Equation A.3).

Overall Performance Uncertainties

Overall performance parameters included the flow coefficient, pressure rise coefficient, total-to-static pressure coefficient, work coefficient and efficiency. All of these values were determined from measured values of temperature, pressure, rotational speed and shaft torque. The functional dependencies are listed in Equations A.4-A.8.

$$\phi = f_1\left(P^o_{ref},\ T^o_{ref},\ T_{dp},\ \omega,\ \Delta p_{mf}, C_d\right) \tag{A.4}$$

$$\psi'/4 = f_2\left(P^o_{ref},\ T^o_{ref},\ T_{dp},\ \omega,\ P_{1.0},\ P_{5.0}\right) \tag{A.5}$$

$$\psi_{ts}/4 = f_3\left(P^o_{ref},\ T^o_{ref},\ T_{dp},\ \omega,\ P_{5.0}\right) \tag{A.6}$$

$$\psi/4 = f_4\left(P^o_{ref},\ T^o_{ref},\ T_{dp},\ \omega,\ \Delta p_{mf},\ C_d,\ Tq\right) \tag{A.7}$$

$$\eta = f_5\left(P^o_{ref},\ T^o_{ref},\ T_{dp},\ \omega,\ \Delta p_{mf},\ C_d,\ Tq,\ P_{1.0},\ P_{5.0}\right) \tag{A.8}$$

The overall performance parameters were then functions of nine independent variables: reference total pressure and temperature, dew point temperature, rotational speed, massflow differential pressure, discharge coefficient, measured torque, and the static pressures at Stations 1.0 and 5.0. Uncertainties of these independent variables are listed in Table A.1. Using these values, the jitter technique [25,26] was used to estimate the uncertainties in the overall performance parameters.

The relative First-Order and *N*th-Order uncertainties (Figures A.1 and A.2 respectively) for each parameter are plotted for a wide range of compressor operation at design speed. Design point values are listed in Table A.2. When acquiring data, the desired operating condition was set by adjusting the flow coefficient. Figure A.1 indicates the precision error in flow coefficient was quit small ($\delta\phi < 0.2\%$). This lead to adequate repeatability when setting the desired operating condition during testing. Efficiency and work coefficient uncertainties were rather high because of an inability to measure the running and tare torque values adequately. When viewing the measured data it is important to remember that the First-Order uncertainties should be used when comparing differences due to configuration changes. *N*th-Order uncertainties should be used when trying to state the absolute levels of the parameters.

Table A.1 Independent variable uncertainties for the overall performance parameters.

Independent Variable	Precision Uncertianty Value	Bias Uncertianty Value
δP^o_{ref}	0.0010 psi	0.0048 psi
δT^o_{ref}	0.20 R	3.325 R
δT_{dp}	0.066 R	1.0 R
$\delta\omega$	0.45 rpm	0.50 rpm
$\delta\triangle p_{mf}$	0.00015 psi	0.00025 psi
C_d	-	0.003
δTq	23.0 in-lbf	43.0 in-lbf
$\delta P_{1.0}$	0.0004 psi	0.0048 psi
$\delta P_{5.0}$	0.0017 psi	0.0048 psi

Table A.2 Overall performance uncertainties at design point operation.

Dependent Variable	First-Order Uncertianty Value	*N*th-Order Uncertianty Value
$\delta\phi$ / ϕ	0.14 %	0.41 %
$\delta\psi'$ / ψ'	0.28 %	0.69 %
$\delta\psi_{ts}$ / ψ_{ts}	0.35 %	0.72 %
$\delta\psi$ / ψ	0.55 %	1.20 %
$\delta\eta$ / η	0.61 %	1.32 %

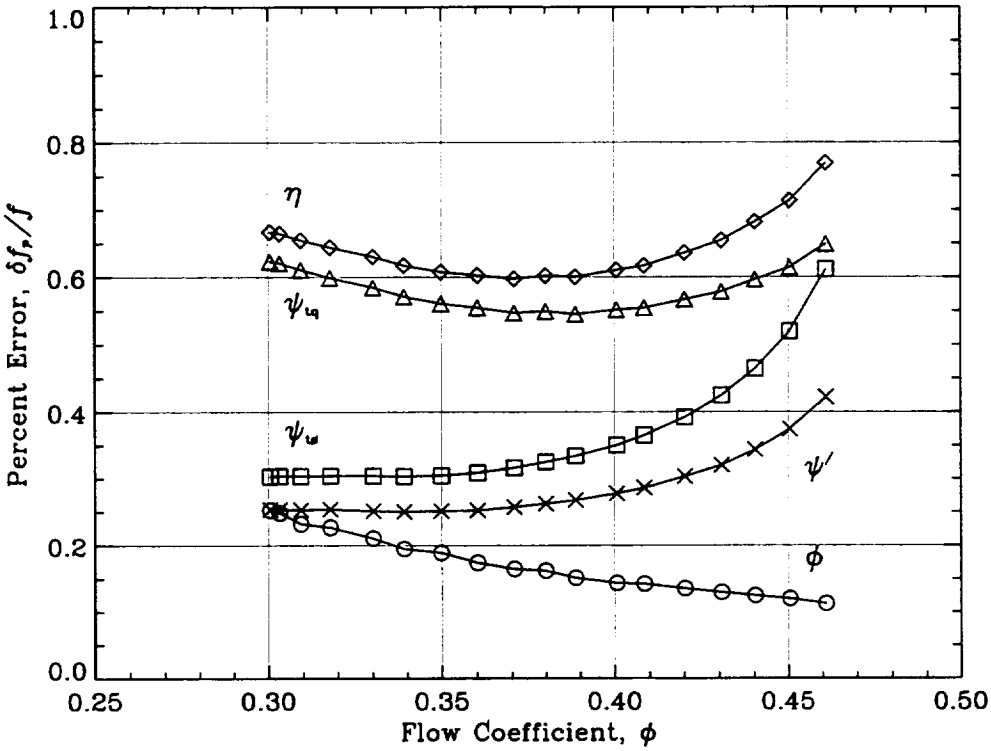

Figure A.1 First-Order uncertainty estimates ($\delta f_p/f$) for overall performance parameters.

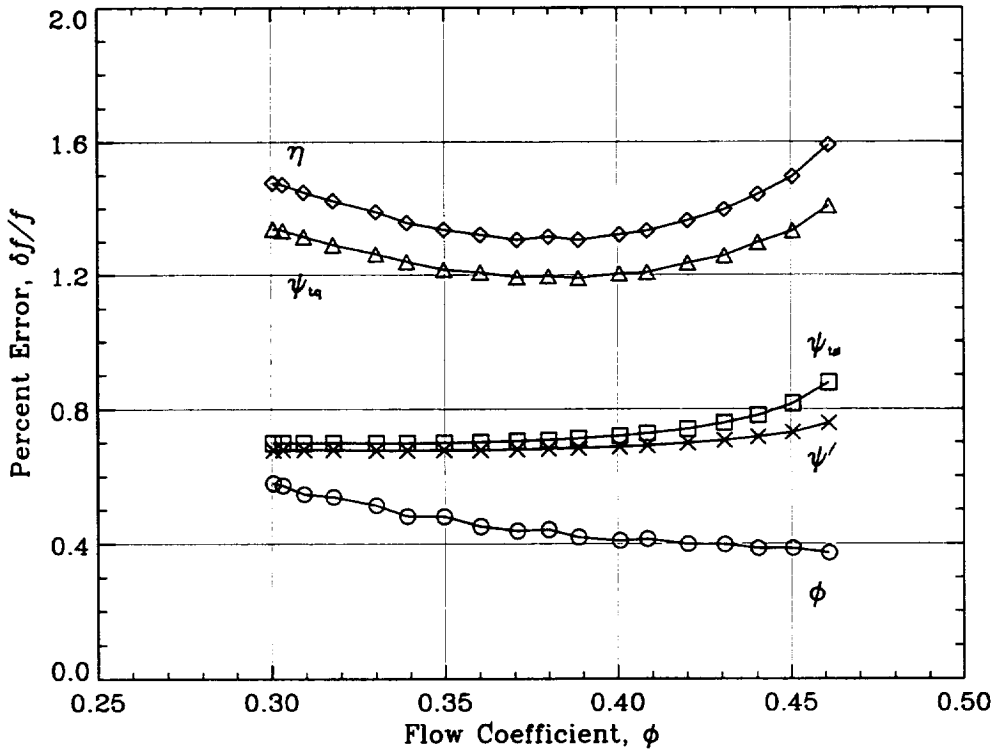

Figure A.2 *N*th-Order uncertainty estimates ($\delta f/f$) for overall performance parameters.

Individual Stage Performance Uncertainties

Stage pressure rise coefficients were calculated from measured values of reference total pressure and temperature, dew point temperature, rotational speed and the static pressures into and out of the stage as shown in Equation A.9. Here, $P_{in,i}$ and $P_{out,i}$ correspond to the proper inlet and outlet static pressures for each stage. Uncertainties of these independent variables are listed in Table A.3. These values were used to estimate the uncertainties in the stage performance parameters using the jitter technique [25,26].

$$\psi_i'/4 = f_i(P^o_{ref},\ T^o_{ref},\ T_{dp},\ \omega,\ P_{in,i},\ P_{out,i}) \tag{A.9}$$

Results for the First-Order and Nth-Order uncertainties are shown in Figures A.3 and A.4, respectively. Uncertainties for each pressure rise coefficient are plotted for the range of compressor operation at design speed. Many of the bias limits were correlated and caused the Nth-Order uncertainties to be similar to the First-Order uncertainties. The higher stage pressure rise errors, compared to overall values, were caused primarily by the smaller pressure difference across a stage when compared to the entire compressor.

Table A.3 Independent variable uncertainties for individual stage performance parameters.

Independent Variable	Precision Uncertianty Value	Bias Uncertianty Value
δP^o_{ref}	0.0010 psi	0.0048 psi
δT^o_{ref}	0.20 R	3.325 R
δT_{dp}	0.066 R	1.0 R
$\delta\omega$	0.45 rpm	0.50 rpm
$\delta P_{1.0}$	0.0004 psi	0.0048 psi
$\delta P_{2.0}$	0.0009 psi	0.0048 psi
$\delta P_{3.0}$	0.0015 psi	0.0048 psi
$\delta P_{4.0}$	0.0018 psi	0.0048 psi
$\delta P_{5.0}$	0.0017 psi	0.0048 psi

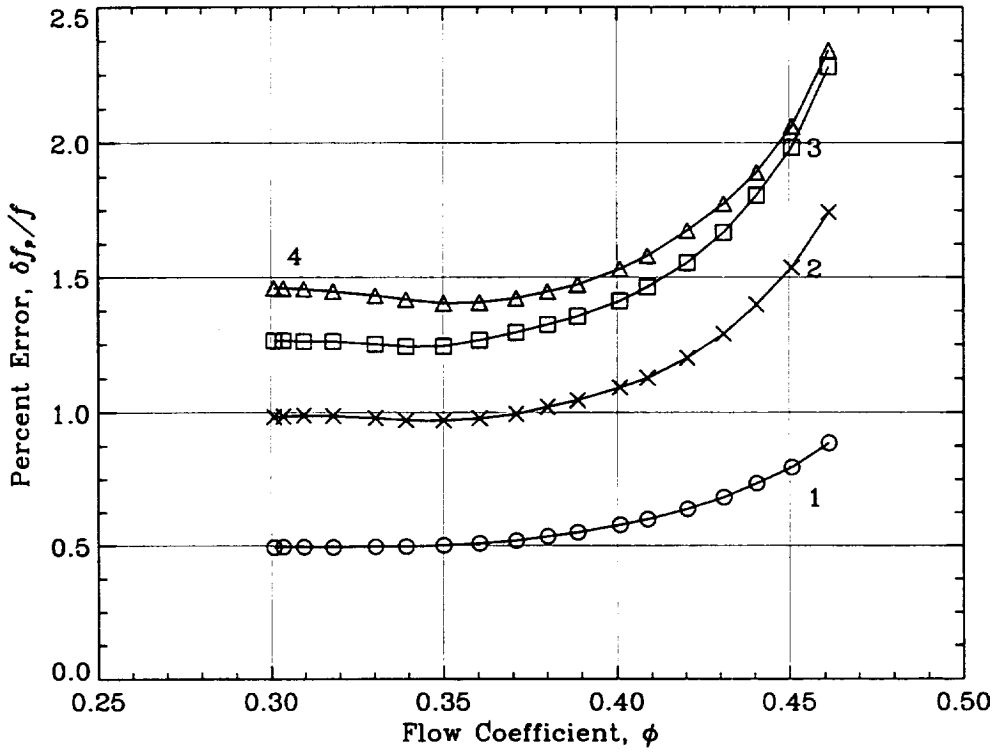

Figure A.3 First-Order uncertainty estimates ($\delta f_p/f$) for stage performance parameters.

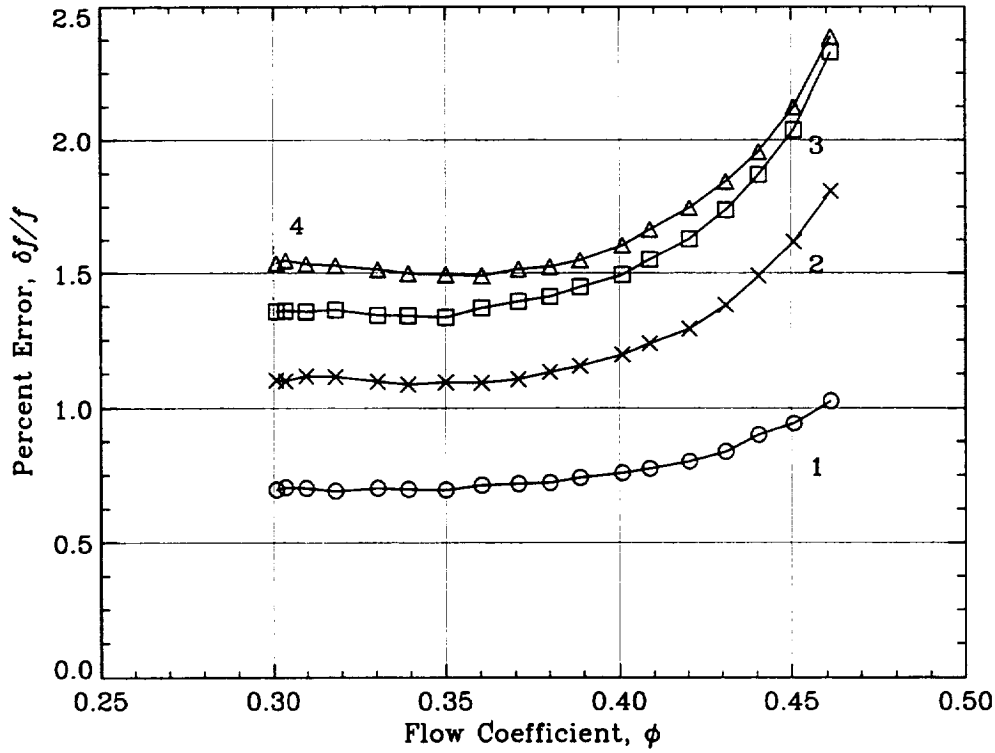

Figure A.4 *N*th-Order uncertainty estimates ($\delta f/f$) for stage performance parameters.

Blade Element Performance Uncertainties

It was truly difficult to assess the uncertainty errors associated with the blade element performance parameters. The following section attempts to summarize the results of the analysis performed. To begin the analysis, estimates on the uncertainties of the measured flow angle and the normalized total and static pressure coefficients were made, since all blade element parameters were calculated from these values. Next, errors associated with velocities and total pressure loss at a single point in space were found. Then, the uncertainties of the circumferential averaged flow properties were assessed. Finally, these were used to calculated the blade element performance errors. It must be noted that this uncertainty estimate does not fully account for the errors in the pneumatic measurements due to unsteadiness, since the ability of pneumatic probes to accurately measure the steady state pressures in an unsteady environment is unknown.

Local total and static pressure coefficients were determined from the measured values of reference pressure and density, probe pressure and rotational speed. Uncertainties of these independent variables are listed in Table A.4. These values were used, along with appropriate partial derivatives, to calculate the precision and bias uncertainties in the pressure coefficients (Equations A.10 and A.11). Results are shown in Table A.5. To give a single value of δCp_t and δCp, typical third stage pressure values were used when calculating the difference between the probe pressure and the reference pressure. Furthermore, the density and tip speed were considered to be the standard day condition and design speed values, respectively.

$$\left.\frac{\delta Cp}{Cp}\right)_p = \left[\frac{\delta P^2 + \delta P_{ref}^2}{\left(P - P_{ref}\right)^2} + \left(\frac{\delta \rho_{ref}}{\rho_{ref}}\right)^2 + \left(2\frac{\delta U_{tip}}{U_{tip}}\right)^2\right]^{1/2} \tag{A.10}$$

$$\left.\frac{\delta Cp}{Cp}\right)_b = \left[\frac{\delta P^2 + \delta P_{ref}^2 - 2\delta P \delta P_{ref}}{\left(P - P_{ref}\right)^2} + \left(\frac{\delta \rho_{ref}}{\rho_{ref}}\right)^2 + \left(2\frac{\delta U_{tip}}{U_{tip}}\right)^2\right]^{1/2} \tag{A.11}$$

The uncertainty estimates in the measured flow angle are also presented in Table A.5. The precision errors were determined from twice the standard deviation of 30 measured points, while the bias limit was taken as twice the average difference between hotfilm and wedge probe measurements traversing the entire stator exit passage.

For data reduction, absolute velocities were calculated with the isentropic compressible flow relations. However, for the uncertainty analysis, incompressible flow was assumed. The assumption of incompressible flow made the analysis much easier with little loss in accuracy. The normalized absolute velocity was estimated by Equation A.12. The relative errors in normalized velocity were found from equations A.13 and A.14. These functions (absolute levels of the pressure coefficients were assumed to be unity)

Table A.4 Independent variable uncertainties for normalized total and static pressures.

Independent Variable	Precision Uncertianty Value	Bias Uncertianty Value
δP^o_{ref}	0.0010 psi	0.0048 psi
$\delta \rho_{ref}$	0.09 $\times$ 10^{-5}slug/ft^3	1.5 $\times$ 10^{-5}slug/ft^3
$\delta \omega$	0.45 rpm	0.50 rpm
δP_t	0.0012 psi	0.0048 psi
δP	0.0016 psi	0.0066 psi

Table A.5 Uncertainties for normalized total and static pressures and flow angle.

Dependent Variable	Precision Uncertianty Value	Bias Uncertianty Value	Nth-Order Uncertianty Value
$\delta Cp_t/Cp_t$	0.0057	0.0063	0.0085
$\delta Cp/Cp$	0.0065	0.0081	0.0104
$\delta \beta$	0.2°	1.5°	1.5°

are also shown in Figure A.5 for the range of velocities encountered in the compressor. Noted in Figure A.5 are typical mid-span stator inlet and exit velocity levels.

$$\frac{V}{U_{tip}} = \sqrt{Cp_t - Cp} \tag{A.12}$$

$$\left.\frac{\delta V}{V}\right)_p = \frac{\left(\delta Cp_i^2 + \delta Cp^2\right)^{1/2}}{2(V/U_{tip})^2} \tag{A.13}$$

$$\left.\frac{\delta V}{V}\right)_b = \frac{\left(\delta Cp_i^2 + \delta Cp^2 - 2\,\delta Cp_t\,\delta Cp\right)^{1/2}}{2(V/U_{tip})^2} \tag{A.14}$$

The axial and tangential components of velocities were calculated by taking the known absolute velocity level and multiplying it by the correct flow angle trigonometric function. The errors in these components were approximated by Equations A.15 and A.16. The first term in these equations represents the error in absolute velocity and was brought about because of self-similar triangles. The second term was simply the error due to the uncertainty in the measured flow angle. The second term is an order of magnitude smaller than the first term except for flow angles very near to 0° and 90°, therefore, to a

good approximation the uncertainties in axial and tangential velocities may be calculated from the already known uncertainty in the absolute velocity magnitude.

$$\frac{\delta V_x}{V_x}\Big)_{p,b} = \left[\left(\frac{\delta V}{V}\right)^2 + \tan^2\beta\ \delta\beta^2\right]^{1/2} \approx \frac{\delta V}{V} \tag{A.15}$$

$$\frac{\delta V_\theta}{V_\theta}\Big)_{p,b} = \left[\left(\frac{\delta V}{V}\right)^2 + \frac{1}{\tan^2\beta}\ \delta\beta^2\right]^{1/2} \approx \frac{\delta V}{V} \tag{A.16}$$

Most of the axisymmetric blade element performance parameters were calculated from these known velocities. Therefore, the uncertainties of axisymmetric parameters could be obtain from the known uncertainties in absolute, axial and tangential velocity. The stator loss coefficient is the only parameter which utilizes uncertainties not already given. Loss at a point in the flow field was defined by Equation A.17. The errors in the loss were then given by Equations A.18 and A.19. For the experiments, the loss in total pressure, $P_1^o - P_2^o$, was measured with a very accurate differential transducer, with a precision error of 0.00015 psi and a bias error of 0.00025 psi. Using these uncertainty values along with those already noted for total and static pressure coefficients, the uncertainties in total pressure loss coefficient were estimated for a two conditions and are shown in Figure A.6.

$$\omega = \frac{P_1^o - P_2^o}{P_1^o - P_1} = \frac{\triangle_{1,2}Cp_t}{Cp_{t,1} - Cp_1} \tag{A.17}$$

$$\frac{\delta\omega}{\omega}\Big)_p = \left[\left(\frac{\delta(\triangle_{1,2}Cp_t)}{\triangle_{1,2}Cp_t}\right)^2 + \frac{\delta Cp_t^2 + \delta Cp^2}{(Cp_{t,1} - Cp_1)^2}\right]^{1/2} \tag{A.18}$$

$$\frac{\delta\omega}{\omega}\Big)_b = \left[\left(\frac{\delta(\triangle_{1,2}Cp_t)}{\triangle_{1,2}Cp_t}\right)^2 + \frac{\delta Cp_t^2 + \delta Cp^2 - 2\delta Cp_t\delta Cp}{(Cp_{t,1} - Cp_1)^2}\right]^{1/2} \tag{A.19}$$

The flow property errors, at one spatial position in the flow field, were used to estimate the uncertainties in the axisymmetric blade element performance parameters. It must be stated that these final calculations are, at best, estimates. From the previous results it is apparent that the flow property uncertainties vary greatly with velocity magnitude, flow angle and pressure level. This implies that property uncertainties varied greatly in the spanwise and pitchwise directions at one measurement station, not to mention throughout the entire compressor. To further complicate matters, axisymmetric values were obtained by averaging across one stator pitch. All of these problems created difficulty when trying to define an upper limit to the uncertainty estimates.

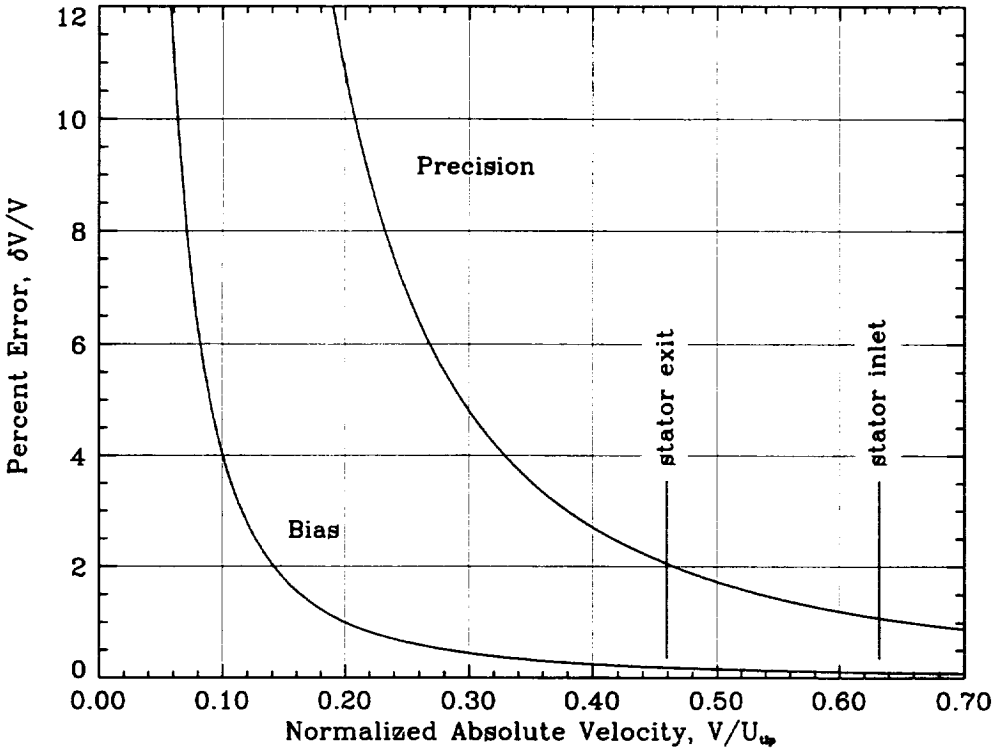

Figure A.5 Percent relative errors in the normalized absolute velocity.

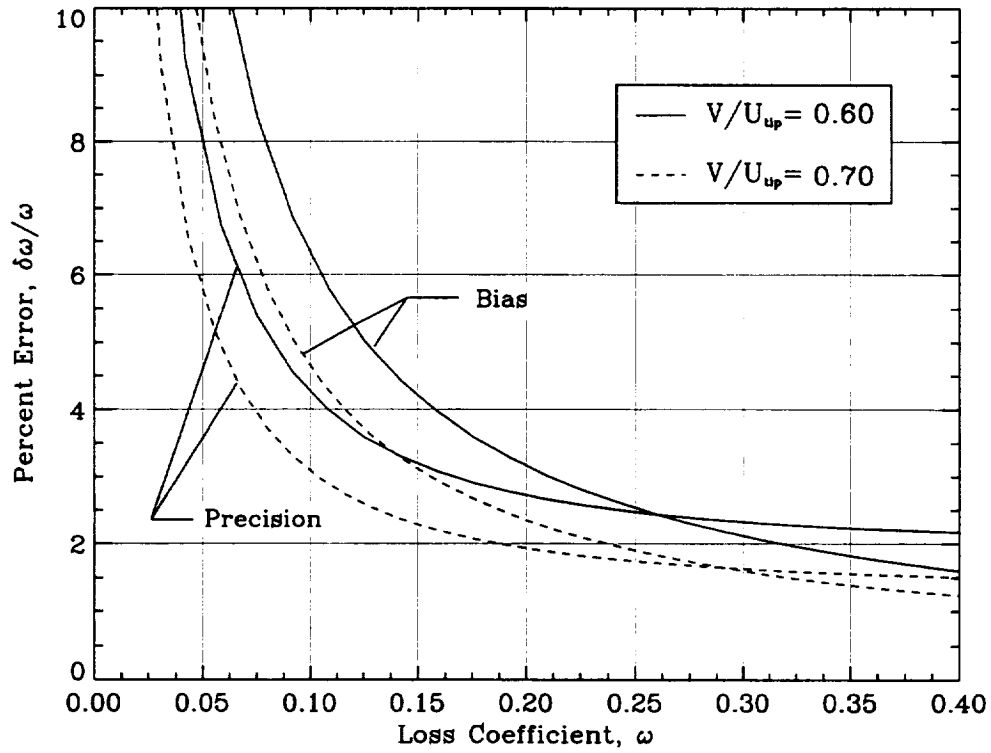

Figure A.6 Percent relative errors in the total pressure loss coefficient.

Figure A.7 Calculated blade element performance errors for mid-span flow conditions.

Variable	First-Order Uncertainty Value	Bias Uncertainty Value	*N*th-Order Uncertainty Value
$\delta\overline{V}/\overline{V}$	1.2 %	0.5 %	1.3 %
$\delta\overline{V_z}/\overline{V_z}$	1.5 %	2.5 %	3.0 %
$\delta\overline{V_\theta}/\overline{V_\theta}$	1.5 %	2.5 %	3.0 %
$\overline{\beta}$	0.35	1.30	1.34
$\triangle\beta$	0.45	1.85	1.90
$\delta DF/DF$	2.0 %	4.0 %	5.0 %
$\delta\omega/\omega$	0.5 %	2.0 %	2.1 %
$\delta\omega_p/\omega_p$	1.7 %	5.5 %	6.0 %

To obtain single valued uncertainty quantities, a single pitchwise survey, which contained nominal flow conditions, was analyzed. The data corresponded to the third stage increased loading mid-span measurements for the baseline configuration. First-Order (precision) uncertainties were calculated from Equation A.1. These errors were random and, therefore, profited from the beneficial effect of averaging. Bias uncertainties were taken as the mean bias uncertainty value across the stator pitch. Since biases are fixed errors, they were not affected by averaging. Results from this analysis are presented in Table A.7. Values are recorded as percentages where appropriate. Only uncertainty quantities corresponding to the absolute frame are presented; however, the respective counterparts in the relative frame were also well approximated by the values in Table A.7.

APPENDIX B

PROBE CALIBRATION AND REDUCTION TECHNIQUES

This appendix contains supplementary information on the calibration methods and data reduction techniques for pneumatic and hotfilm probes. Brief descriptions of the probes are also included. The pneumatic probes used in the experiments included kiel, wedge and five-hole types. Five-hole probe calibration techniques used in this thesis closely follow the methods developed by Everett *et al.* [27] Hotfilm calibration techniques followed the methods developed by Degrand and Kool [28] but are not reviewed here. The reader is referred to these references for further details.

Probe Calibration Facility

The facility used for the calibration of aerodynamic and hotfilm probes is illustrated in Figure B.1. The rig was designed for convenient access. With it, the accurate calibration of measurement probes was possible. The facility consisted of a flow conditioning section, contraction nozzle, calibration exhaust jet and an exhaust diverter.

Flow conditioning section

The flow conditioning section provided a uniform low turbulence intensity free-stream flow field. Pressurized shop air was used as the flow driving mechanism. Mach numbers up to 0.95 were attainable. The flow rate was controlled by a gate valve. A Cuno filter retained foreign particles from continuing downstream. A perforated steel cone mixed the flow. A two inch wide honeycomb mesh reduced large eddies into small eddies and a fine mesh screen eliminated any local nonuniformities created by the honeycomb mesh. Plenum total pressure was measured by a Pitot probe positioned downstream of the screen. The jet static pressure was assumed to be the test cell atmospheric pressure. The exit contraction nozzle, with an exit diameter of 3.80 cm and an area contraction ratio of 28 to 1, uniformly accelerated the flow such that no measurable centerline losses occurred between the measured plenum total pressure and the calibration point.

Calibration point

The calibration point was located 2.54 cm away from the contraction exit and in the center of the exhaust jet. Figure B.2 indicates the jet core had a uniform total pressure distribution for a large range of Mach numbers. Rotations in the pitch and yaw directions could occur without repositioning the calibration point. Pitching motion was electronically controlled by an L.C. Smith actuator connected to a lever arm. This assembly required a calibration of the pitch angle to actuator step position. The curve which correlates the pitch angle to actuator step position is given in Equation B.1. The

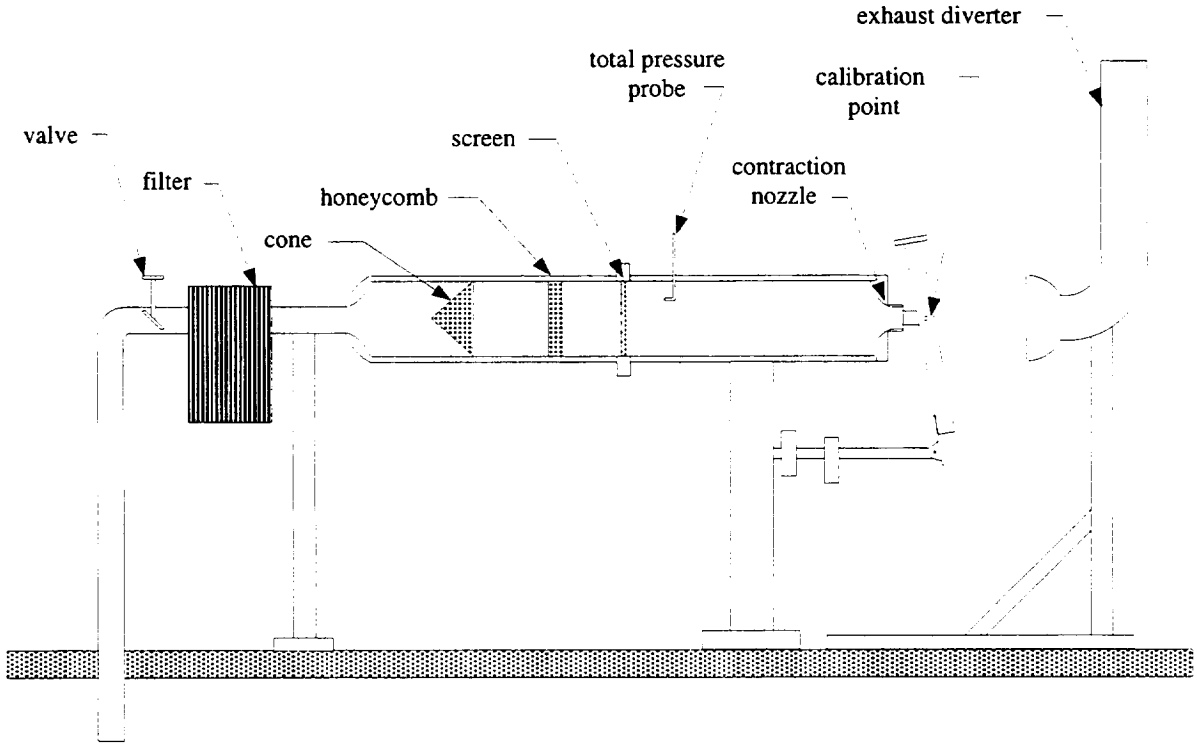

Figure B.1 Probe calibration facility illustration.

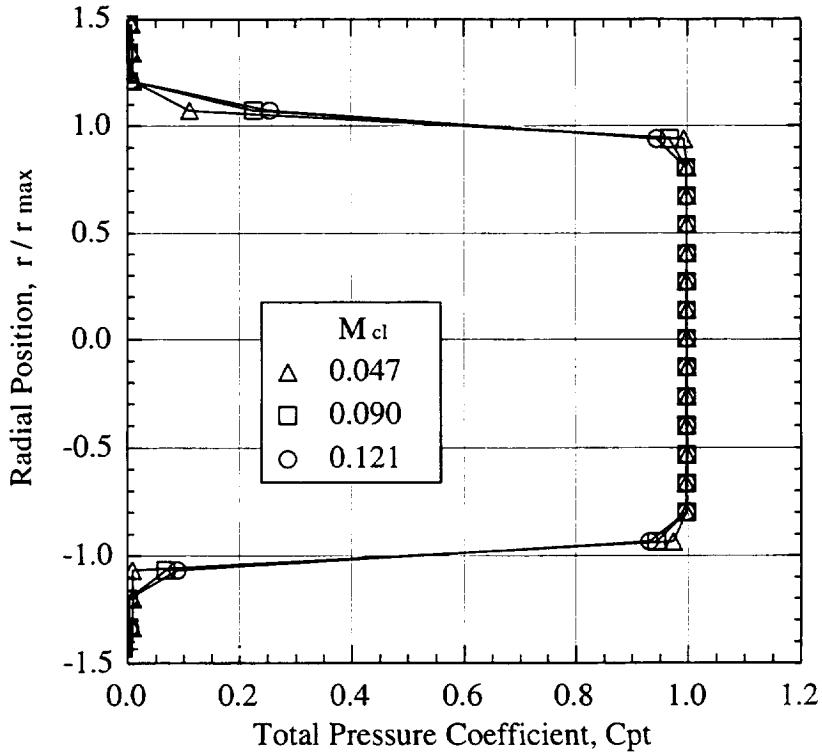

Figure B.2 Distribution of total pressure across the calibration jet.

variance on the forth order fit was 0.1068. Yawing motion was adjusted by the L.C. Smith actuator in which the probe was mounted.

$$
\begin{aligned}
N_{step} =& a_0 + a_1\alpha + a_2\alpha^2 + a_3\alpha^3 + a_4\alpha^4 \\
a_0 &= 0.482884 \times 10^3 \\
a_1 &= -0.165604 \times 10^2 \\
a_2 &= 0.161018 \times 10^{-1} \\
a_3 &= 0.110516 \times 10^{-2} \\
a_4 &= 0.207685 \times 10^{-4}
\end{aligned}
\tag{B.1}
$$

Kiel Probe

Miniaturized kiel probes were used to measure total pressures in the compressor. A scale drawing of a kiel probe is shown in Figure B.3. The probe was constructed of silver brazed stainless steel tubes. The measurement tube was 0.254 mm in diameter and was shielded with a 1.65 mm diameter hypodermic tube approximately 3.2 mm in length. The opening of the tubes were normal to their centerlines. The shield was chamfered 45° on the leading edge.

Kiel probes were not calibrated; however, measurement characteristics were checked to ensure each probe read the correct total pressure over a wide range of flow angles. To check the measurement characteristics, probes were positioned in the center of the jet flow field produced by the calibration facility. The probe was automatically pitched

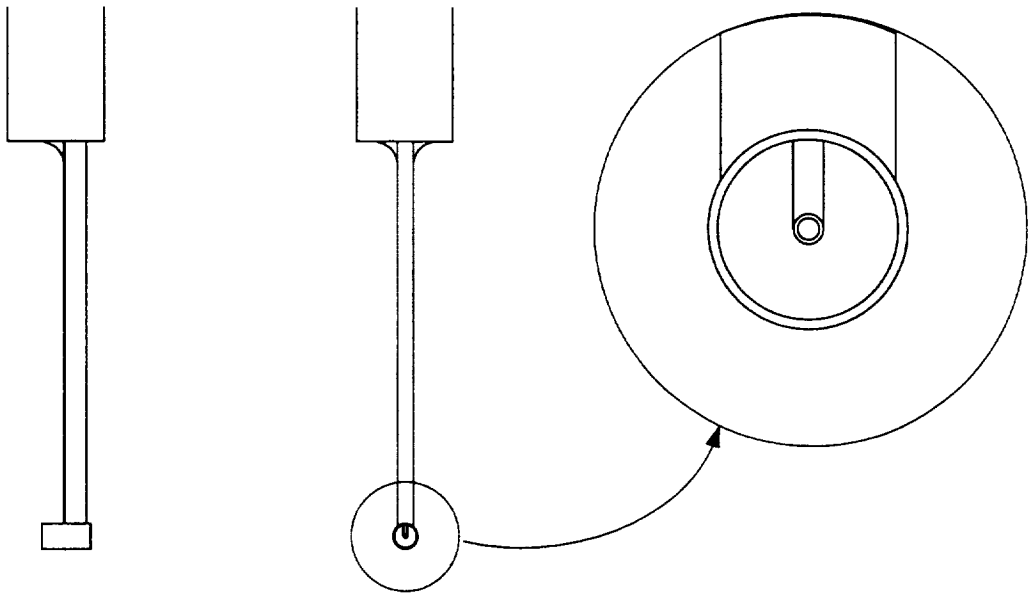

Figure B.3 Pictorial of a miniature kiel probe.

and yawed while recording the measured pressure (P_i). The jet total pressure (P^o) was measured by a Pitot tube, shown in Figure B.1, and jet static pressure (P) was assumed to be the test-cell atmospheric pressure. Pressure coefficients were calculated as in Equation B.2.

$$Cp_i = \frac{P_t - P}{P^o - P} \tag{B.2}$$

Typical errors in the measured total pressure coefficients are shown in Figure B.4. Here, the error in total pressure is plotted against the probe yaw angle for three pitch angles. The shaded region represents the uncertainty band due to the precision errors in the pressure transducers. Kiel probes usually had a ±40° range in which the total pressure was measured correctly. Probes which gave pressure measurements far outside the uncertainty band or had erratic behavior when pitched or yawed were discarded and used as javelins.

Wedge Probe

Wedge probes were used to measure static pressures and flow angles in the compressor. A scale drawing of a wedge probe is shown in Figure B.5. The included wedge angle was 18°. The wedge portion of the probe was approximately 1.52 cm in length. The two side ports (0.4 mm diameter) were located along the probe stem centerline but offset radially by 1.3 mm. The ports were drilled normal to their respective side. Encased hypodermic tubes conveyed the side port pressures up the probe stem.

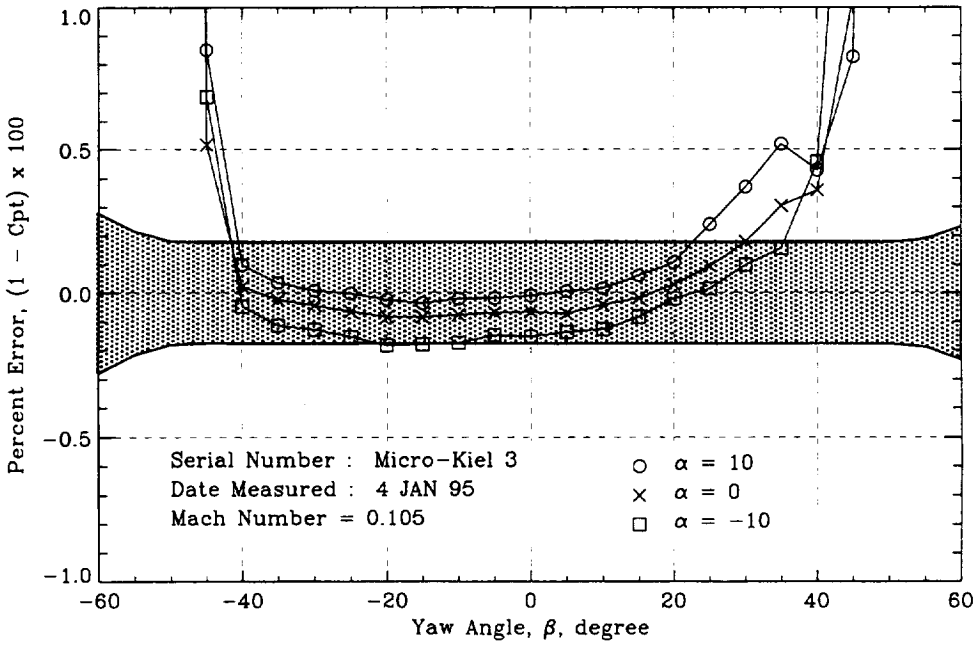

Figure B.4 Measurement characteristics of a miniature kiel probe.

Wedge probes were calibrated and their measurement characteristics were checked. To check the measurement characteristics, probes were positioned in the center of the jet flow field produced by the calibration facility. Pressures were measured over a wide range of pitch and yaw angles. The zero yaw position was found by nulling the probe until the side port pressures were equal. Pressure coefficients were calculated as in Equation B.3 for each port. As with kiel probes, the jet total pressure was measured by a Pitot tube, shown in Figure B.1, and jet static pressure was the test-cell atmospheric pressure.

$$Cp_i = \frac{P_i - P}{P^o - P} \tag{B.3}$$

Common characteristics of side port pressure measurements are shown in Figure B.6. Both side port pressures (Cp_1 and Cp_2) are plotted against the probe yaw angle for three pitch angles. The discontinuity near $\pm 10°$ was common among all wedge probes tested and was believed to be caused by the flow separating off the leading edge of the wedge. Probes which had wildly erratic behavior when pitched or yawed or had difficultly auto-nulling were discarded. Errors in the static pressure coefficient (Equation B.4) are shown in Figure B.7. The shaded region represents the uncertainty band due to the precision errors in the pressure transducers. Large errors in static pressure were present and depended greatly on the pitch angle and yaw angle of the probe.

$$Cp_s = \frac{Cp_1 + Cp_2}{2} \tag{B.4}$$

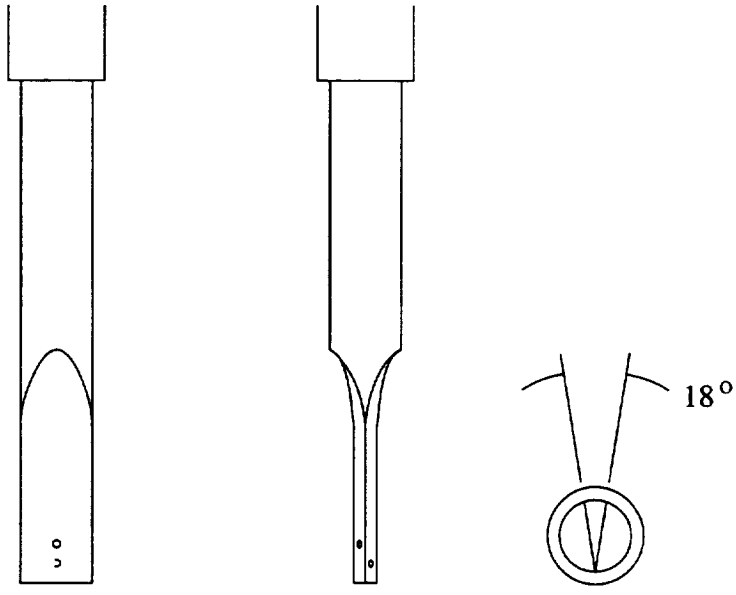

Figure B.5 Pictorial of a wedge probe.

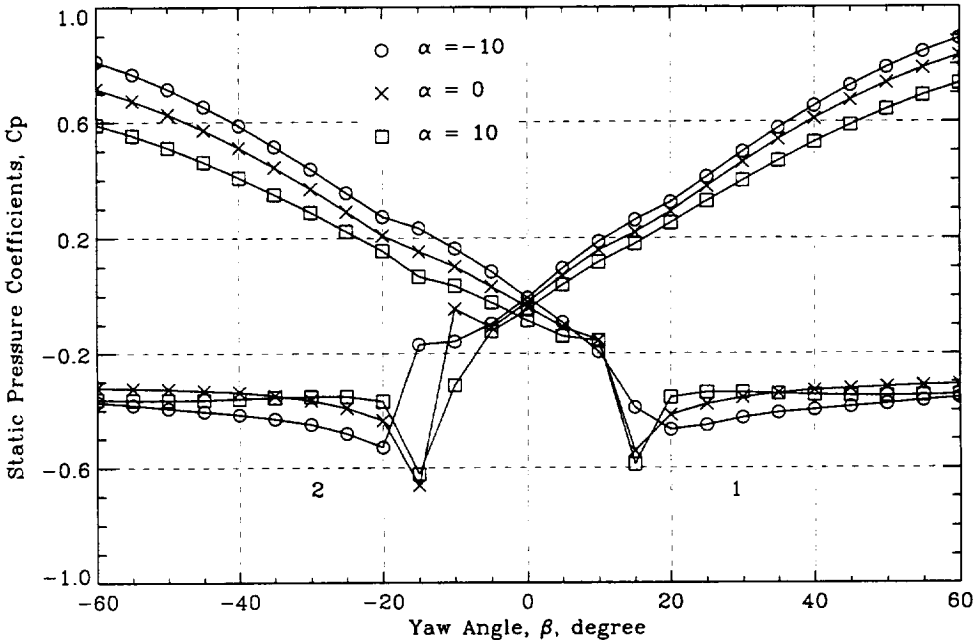

Figure B.6 Side port pressures of a wedge probe.

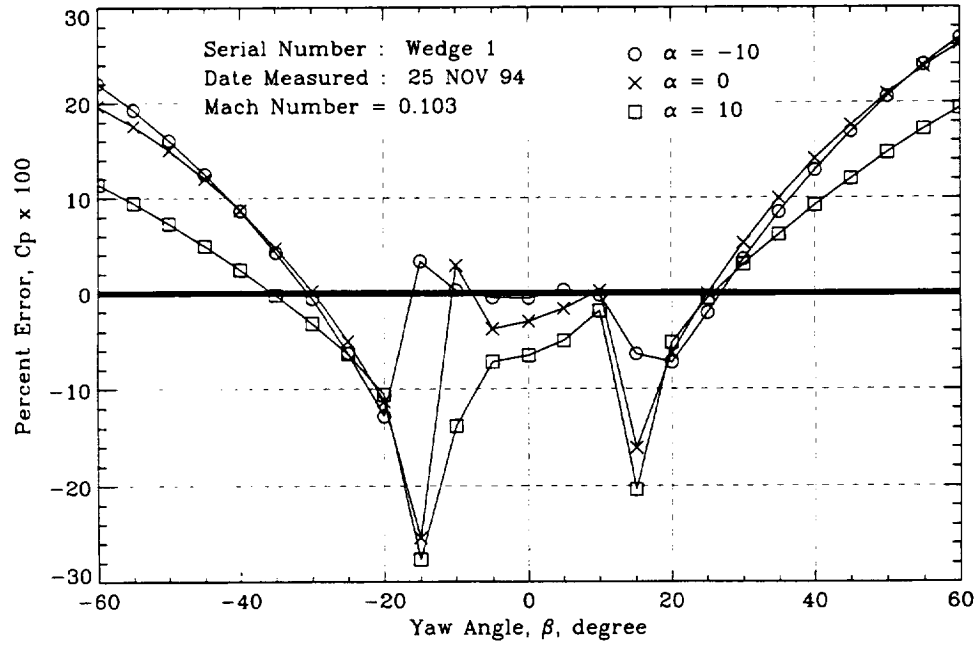

Figure B.7 Wedge probe static pressure errors at different pitch and yaw angles.

Since the wedge probe incorrectly measured the static pressure, a calibration was performed in an attempt to correct the error. The calibration accounted for "wall proximity" effects and scaled with the local dynamic head approaching the probe. Wall proximity effects are common when using wedge type probes and have been documented many times, most recently by Smout and Ivey [29]. The effect forces non-constant calibration coefficients to be used across the span. The influence of yaw and pitch angle were ignored, since the wedge probe was used in an auto-nulling mode, and pitch angle variations were considered small in the compressor flow field.

The calibration was performed in the LSAC ahead of the inlet-guide vanes instead of the calibration facility. Here, the flow was nearly in the axial direction across the entire span. Boundary layer thicknesses were approximately 30% of the span at both the hub and case. Both wedge and kiel probes were traversed across the span at different through-flow rates. The kiel probe measured the local total pressure while the wedge probe gave an estimate of the local static pressure. The true static pressure was assumed to vary linearly across the span, with the end points being set by the measured hub and case static pressures. From these measurements a relation between the true and measured local static pressure was determined.

The calibration used the pressure coefficient defined in Equation B.5. After viewing the recorded data it was found the pressure coefficient could be approximated to be linear with respect to the radial position for a portion of the span and constant across the rest of the span. Hence the pressure coefficient was represented by Equation B.6, where a was the calibration constant and r_a corresponded to the radius were the linear variation stopped. The calibration constants were determined from a least-squares fit to the measured data.

$$Cp_c(r) = \frac{2P - (P_1 + P_2)}{2P^o - (P_1 + P_2)} \tag{B.5}$$

$$Cp_c(r) = \begin{cases} \frac{a}{r_{tip} - r_a}(r_{tip} - r) & r_a \leq r < r_{tip} \\ a & r < r_a \end{cases} \tag{B.6}$$

Wedge probe calibration data are depicted in Figure B.8. Here the pressure coefficient is plotted against the span for three different flow rates. The measured data are given by symbols, the calibration fit is denoted by the thick line while the standard deviation to the calibration fit is represented by the dashed lines. Although not perfect, the calibration gives reasonable estimates to the static pressure across the span. Standard deviations were below 1.5% with maximum deviations usually not larger than 3.0%.

Local static pressures in the compressor were found by employing Equation B.7, where the pressure coefficient (Cp_c) was dependent on probe location and the total

pressure was measured with a kiel probe.

$$P = \frac{P_1 + P_2}{2} + Cp_c\left(P^o - \frac{P_1 + P_2}{2}\right) \tag{B.7}$$

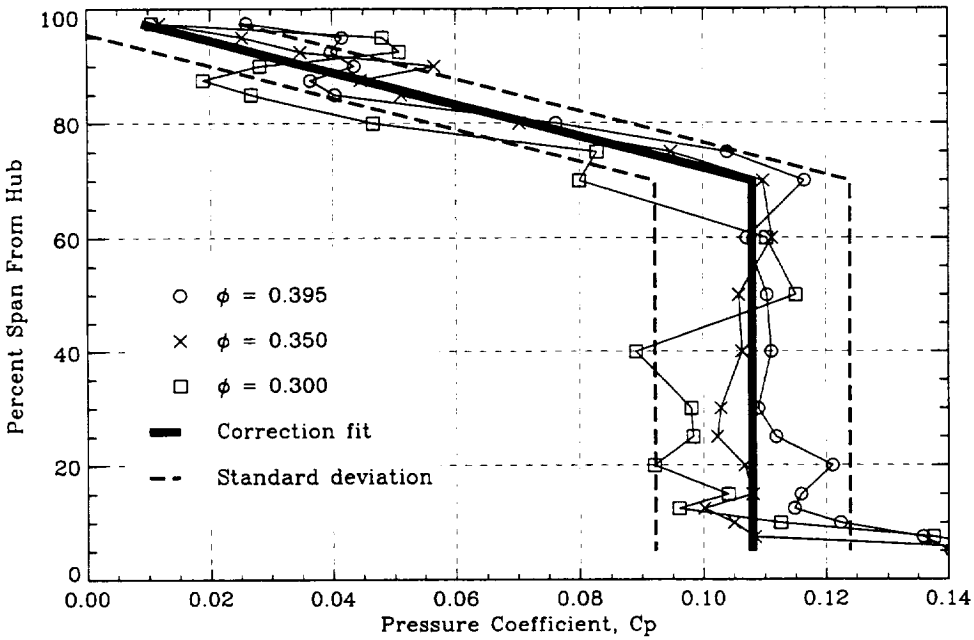

Figure B.8 Static pressure calibration of a wedge probe.

Five-Hole Probe

A drawing of the five-hole probe used is shown in Figure B.9. The probe axes and nomenclature assigned to the individual openings are also presented. The probe was constructed of five silver brazed stainless steel tubes, each having an inside diameter of 0.056 cm. The opening of the center tube was normal to its centerline. The openings of the four outer tubes were inclined 45° to their centerlines. This arrangement resulted in yawing and pitching symmetry.

Non-yaw-nulling calibration and reduction techniques were used. This method permitted the unknown flow conditions within the test flow field to be found without the need for the probe to be nulled in the yaw direction. The flow conditions were determined from measured probe pressures and the calibration coefficients.

The non-yaw-nulled five-hole probe calibration empirically determined the relationships between the flow conditions (P^o, P, α_c and β_c) and the five measured pressures of the probe ($P_1, \cdots, P_5$). The pressures measured during probe calibration

were nondimensionalized as indicated in Equation B.8.

$$Cp_i = \frac{P_i - P}{P^o - P} \tag{B.8}$$

The pressure coefficients were dependent on Mach number, M, Reynolds number, Re, specific heat ratio, γ, the measured pitch angle, α_c, and the measured yaw angle, β_c. Reynolds number, specific heat ratio and Mach number were removed from the list of independent variables since these values did not change significantly during testing. Pitch and yaw angles were then the independent calibration variables.

The calibration was accomplished by varying pitch angle and yaw angle while measuring the probe pressures. The probe openings were positioned near the center of the jet flow field produced by the calibration facility. Prior to calibration the zero yaw position was found by nulling the probe in the jet flow until the two side ports equaled. Total pressure was measured by the Pitot tube, shown in Figure B.1. Static pressure was the test-cell atmospheric pressure. Typical pressure coefficient data are shown in Figure B.10. Here the five coefficients are plotted against the measured pitch angle, α_c, and measured yaw angle, β_c.

Taylor series expansions were used to approximate the relationships between the flow conditions and the measured pressures. Four flow conditions were expanded: pitch angle, yaw angle, total pressure coefficient (Equation B.9) and dynamic head coefficient

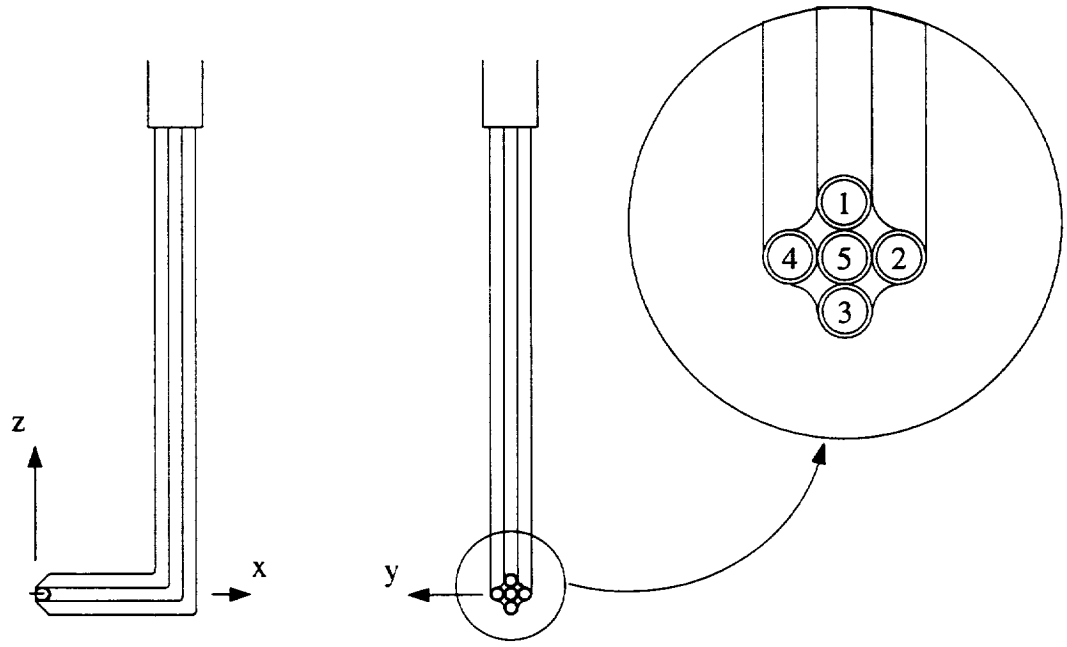

Figure B.9 Pictorial of the five-hole probe.

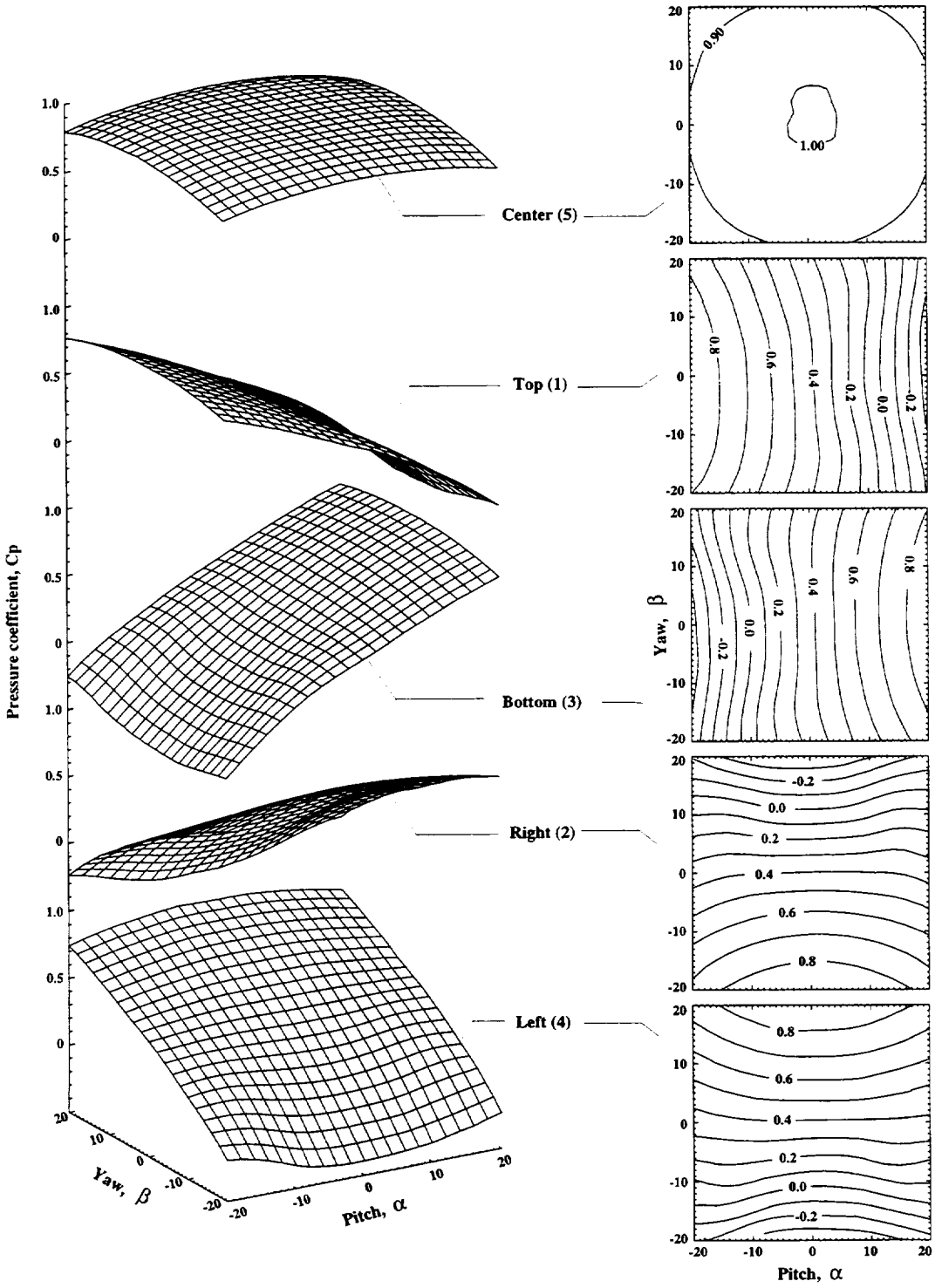

Figure B.10 Variation of pressure coefficients with pitch and yaw angle.

(Equation B.10).

$$Cp_t = \frac{Cp_5 - 1}{Cp_5 - Cp_{avg}} \tag{B.9}$$

$$Cp_q = \frac{1}{Cp_5 - Cp_{avg}} \tag{B.10}$$

An approximation to a general flow condition is given in Equation B.11. Here a general flow condition is given as an expansion of the pitch pressure coefficient (Cp_α) and the yaw pressure coefficient (Cp_β). These coefficients are defined in Equations B.12 and B.13. The subscript i identifies the equation as representing the value of the flow property measured for the ith data point. Fifth-order approximations were used. Therefore, 21 calibration coefficients for each flow condition variable were calculated.

$$\begin{aligned} g_i(Cp_\alpha, Cp_\beta) = (a_1 + \\ & a_2 Cp_\alpha + a_3 Cp_\beta + \\ & a_4 Cp_\alpha^2 + a_5 Cp_\alpha Cp_\beta + a_6 Cp_\beta^2 + \\ & a_7 Cp_\alpha^3 + a_8 Cp_\alpha^2 Cp_\beta + a_9 Cp_\alpha Cp_\beta^2 + a_9 Cp_\beta^3 \ \ldots)_i \end{aligned} \tag{B.11}$$

$$Cp_\alpha = \frac{Cp_1 - Cp_3}{Cp_5 - Cp_{avg}} \tag{B.12}$$

$$Cp_\beta = \frac{Cp_2 - Cp_4}{Cp_5 - Cp_{avg}} \tag{B.13}$$

Defining the vectors [g] and [a] and the matrix [M] enables a system of equations (Equation B.14) to be abbreviated as Equation B.15. The $I \times 1$ [g] vector contains values of one of the four flow properties, the $I \times 21$ [M] matrix contains the corresponding expanded pressure coefficient variables and the 21×1 [a] vector contain the calibration constants.

$$\begin{bmatrix} g_1 \\ g_2 \\ \cdot \\ \cdot \\ g_{I-1} \\ g_I \end{bmatrix} = \begin{bmatrix} 1 & Cp_{\alpha_1} & Cp_{\beta_1} & \cdots & Cp_{\alpha_1} Cp_{\beta_1}^4 & Cp_{\beta_1}^5 \\ 1 & Cp_{\alpha_2} & Cp_{\beta_2} & \cdots & Cp_{\alpha_2} Cp_{\beta_2}^4 & Cp_{\beta_2}^5 \\ \cdot & \cdot & \cdot & & & \cdot \\ \cdot & \cdot & \cdot & & & \cdot \\ 1 & Cp_{\alpha_{I-1}} & Cp_{\beta_{I-1}} & \cdots & Cp_{\alpha_{I-1}} Cp_{\beta_{I-1}}^4 & Cp_{\beta_{I-1}}^5 \\ 1 & Cp_{\alpha_I} & Cp_{\beta_I} & \cdots & Cp_{\alpha_I} Cp_{\beta_I}^4 & Cp_{\beta_I}^5 \end{bmatrix} \begin{bmatrix} a_1 \\ a_2 \\ \cdot \\ \cdot \\ a_{20} \\ a_{21} \end{bmatrix} \tag{B.14}$$

$$[\mathbf{g}] = [\mathbf{M}][\mathbf{a}] \tag{B.15}$$

Calibration constants were determined from a least-squares-curve fit to the experimental data, as given in Equation B.16. Once the calibration constants were determined, the corresponding curve fits were compared to the known calibration data to ensure proper representations of the flow properties. Probes were discarded if they had irregular calibration behaviors or if the fifth order expansions were unable to capture the probes measured flow conditions.

$$[\mathrm{a}] = \left[\mathbf{M}^{\mathrm{T}}\mathbf{M}\right]^{-1}[\mathbf{M}]^{\mathrm{T}}[\mathrm{g}] \tag{B.16}$$

The data reduction procedure resolved the local total pressure, static pressure and velocity vector components from the measured probe pressures. The procedure began by calculating the pitch and yaw pressure coefficients (Equations B.12 and B.13). From these coefficients and the empirically derived calibration coefficients, each fitted flow condition was found explicitly using the Taylor-series expansions (Equation B.11). Pitch and yaw angles were determined directly from the appropriate curve fit. Total and static pressure coefficients were found from solving Equations B.17 and B.18.

$$Cp^{o} = Cp_5 - Cp_t(Cp_5 - Cp_{avg}) \tag{B.17}$$

$$Cp = Cp^{o} - Cp_q(Cp_5 - Cp_{avg}) \tag{B.18}$$

The reduction was completed by calculating the velocity components. For these calculations the local Mach number was obtained from the isentropic compressible flow relations using the corrected total and static pressure values. The velocity magnitude was calculated using the definition of Mach number. It was assumed the total temperature at the probe head equaled the standard day condition. Velocity components were then found with Equations B.19-B.21. Here, the yaw offset (β_o) was the absolute position the probe was set at during the survey.

$$V_r = V \sin\alpha \tag{B.19}$$

$$V_\theta = V \cos\alpha \ \cos(\beta_o - \beta) \tag{B.20}$$

$$V_z = V \cos\alpha \ \sin(\beta_o - \beta) \tag{B.21}$$

REPORT DOCUMENTATION PAGE

Form Approved
OMB No. 0704-0188

1. AGENCY USE ONLY (*Leave blank*)	2. REPORT DATE	3. REPORT TYPE AND DATES COVERED
	October 1996	Final Contractor Report

4. TITLE AND SUBTITLE

Effects of Shrouded Stator Cavity Flows on Multistage Axial Compressor Aerodynamic Performance

5. FUNDING NUMBERS

WU–505–62–52
G–NAG3–1427

6. AUTHOR(S)

Steven R. Wellborn and Theodore H. Okiishi

7. PERFORMING ORGANIZATION NAME(S) AND ADDRESS(ES)

Iowa State University
Ames, Iowa 50011

8. PERFORMING ORGANIZATION REPORT NUMBER

E–10465

9. SPONSORING/MONITORING AGENCY NAME(S) AND ADDRESS(ES)

National Aeronautics and Space Administration
Lewis Research Center
Cleveland, Ohio 44135–3191

10. SPONSORING/MONITORING AGENCY REPORT NUMBER

NASA CR–198536

11. SUPPLEMENTARY NOTES

Project Manager, Michael D. Hathaway, Internal Fluid Mechanics Division, organization code 2640, (216) 433–6250.

12a. DISTRIBUTION/AVAILABILITY STATEMENT

Unclassified - Unlimited
Subject Categories 02 and 07

This publication is available from the NASA Center for AeroSpace Information, (301) 621–0390.

12b. DISTRIBUTION CODE

13. ABSTRACT ***(Maximum 200 words)***

Experiments were performed on a low-speed multistage axial-flow compressor to assess the effects of shrouded stator cavity flows on aerodynamic performance. Five configurations, which involved changes in seal-tooth leakage rates and/or elimination of the shrouded stator cavities, were tested. Data collected enabled differences in overall, individual stage and the third stage blade element performance parameters to be compared. The results show conclusively that seal-tooth leakage can have a large impact on compressor aerodynamic performance while the presence of the shrouded stator cavities alone seemed to have little influence. Overall performance data revealed that for every 1% increase in the seal-tooth clearance to blade-height ratio the pressure rise dropped up to 3% while efficiency was reduced by 1 to 1.5 points. These observed efficiency penalty slopes are comparable to those commonly reported for rotor and cantilevered stator tip clearance variations. Therefore, it appears that in order to correctly predict overall performance it is equally important to account for the effects of seal-tooth leakage as it is to include the influence of tip clearance flows. Third stage blade element performance data suggested that the performance degradation observed when leakage was increased was brought about in two distinct ways. First, increasing seal-tooth leakage directly spoiled the near hub performance of the stator row in which leakage occurred. Second, the altered stator exit flow conditions caused by increased leakage impaired the performance of the next downstream stage by decreasing the work input of the downstream rotor and increasing total pressure loss of the downstream stator. These trends caused downstream stages to progressively perform worse. Other measurements were acquired to determine spatial and temporal flow field variations within the up-and-downstream shrouded stator cavities. Flow within the cavities involved low momentum fluid traveling primarily in the circumferential direction at about 40% of the hub wheel speed. Measurements indicated that the flow within both cavities was much more complex than first envisioned. A vortical flow structure in the meridional plane, similar to a driven cavity, existed within the upstream cavity. Furthermore, other spatial and temporal variations in flow properties existed, the most prominent being caused by the upstream potential influence of the downstream blade. This influence caused the fluid within cavities near the leading edges of either stator blades in space or rotor blades in time to be driven radially inward relative to fluid near blade mid-pitch. This influence also produced large unsteady velocity fluctuations in the downstream cavity because of the passing of the downstream rotor blade.

14. SUBJECT TERMS	15. NUMBER OF PAGES
Turbomachinery; Compressors; Shrouds; Cavities; Labyrinth seal leakage	138
	16. PRICE CODE: A07

17. SECURITY CLASSIFICATION OF REPORT	18. SECURITY CLASSIFICATION OF THIS PAGE	19. SECURITY CLASSIFICATION OF ABSTRACT	20. LIMITATION OF ABSTRACT
Unclassified	Unclassified	Unclassified	